

Aus der Klinik und Poliklinik für Innere Medizin A  
(Direktor/in Univ.- Prof. Dr. Markus M. Lerch)  
der Universitätsmedizin der Ernst-Moritz-Arndt-Universität Greifswald

**Tumor specific delivery of siRNA coupled superparamagnetic iron  
oxide nanoparticles, targeted against Polo-like kinase 1, stops  
progression of pancreatic ductal adenocarcinoma**

Inaugural - Dissertation  
zur  
Erlangung des akademischen  
Grades  
**Doktor der Wissenschaften in der Medizin**  
**(Dr. rer. med.)**

der  
Universitätsmedizin  
der  
Ernst-Moritz-Arndt-Universität  
Greifswald  
**2015**

vorgelegt von:  
**Mahajan, Ujwal Mukund MS (Pharm.)**  
geb. am: 26 August, 1986  
in: Nashik, Maharashtra, India



Dekan: Prof. Dr. rer.nat. Max P. Baur

1. Gutachter: Frau Prof. Dr. Julia Mayerle

2. Gutachter: Prof. Dr. Walter Halangk

Ort, Raum: Seminarraum O 0.65 der klinik für Innere Medizin A, Sauerbruchstr.,  
Greifswald

Tag der Disputation: 12.02.2016



***“What we know is a drop, what we don't know is an ocean.”***

-Sir Isaac Newton



## TABLE OF CONTENT

<b>LIST OF FIGURES</b> .....	<b>A</b>
<b>LIST OF TABLES</b> .....	<b>C</b>
<b>ABBREVIATIONS</b> .....	<b>D</b>
<b>1. INTRODUCTION</b> .....	<b>1</b>
<b>2. THEORETICAL BACKGROUND</b> .....	<b>3</b>
<b>2.1 Pancreatic ductal adenocarcinoma</b> .....	<b>3</b>
<b>2.2 Factor predisposing to PDAC:</b> .....	<b>4</b>
<b>2.3 Pathogenesis of pancreatic cancer:</b> .....	<b>4</b>
<b>2.4 Alteration of cell cycle during progression of pancreatic cancer:</b> .....	<b>6</b>
2.4.1 Polo like kinases (PLKs): .....	8
2.4.2 The role of PLK1 in malignant transformation:.....	8
2.4.3 Dysregulated PLK1 in human cancers .....	10
2.4.4 PLK1 targeting in cancer therapy .....	11
<b>2.5 Lack of efficacy traditional cancer therapy</b> .....	<b>12</b>
<b>2.6 Novel treatment approach with PLK1</b> .....	<b>13</b>
<b>2.7 Theranostics</b> .....	<b>14</b>
<b>2.8 Iron oxide nanoparticles</b> .....	<b>15</b>
2.8.1 Characteristics SPIONs .....	16
<b>2.9 Ligand targeted therapy</b> .....	<b>17</b>
2.9.1 MUC1 .....	18
2.9.2 MPAP .....	18
<b>2.10 Use of RNA interference in Tumor therapy</b> .....	<b>19</b>
<b>3. HYPOTHESIS</b> .....	<b>20</b>
<b>4. MATERIALS AND METHODS</b> .....	<b>21</b>
<b>4.1 Materials</b> .....	<b>21</b>
4.1.1 Antibodies and growth factors .....	21
4.1.2 Enzymes, kits and substrates.....	21
4.1.3 Peptides and siRNAs .....	22
4.1.4 Chemicals .....	22
4.1.5 Glasswares and labwares .....	25
4.1.7 Instruments .....	29
4.1.8 Cell-lines and Animals.....	30
4.1.9 Software.....	31
<b>4.2 Methods</b> .....	<b>32</b>
4.2.1 siRNAs.....	32
4.2.2 siPLK1-StAv-SPIONs synthesis .....	32
4.2.3 Characterization of SPIONs .....	33
4.2.4 Animal strains .....	34
4.2.5 Measurement of iron content.....	34
4.2.6 Cell cycle analysis.....	35
4.2.7 Proliferation assay .....	35
4.2.8 In solution stability of siPLK1-StAv-SPIONs .....	35
4.2.9 In vitro toxicity .....	35
4.2.10 Live cell imaging and uptake measurement .....	35
4.2.11 Fluorescence Immunostaining .....	36
4.2.12 Transmission electron microscopy .....	36
4.2.13 Flow cytometric analysis .....	37

4.2.14 MRI analysis .....	37
4.2.15 Iron staining in tumor section (Perl's staining) .....	37
4.2.16 Pharmacokinetics.....	38
4.2.17 Immunoblotting .....	38
4.2.18 Quantitative real-time PCR analysis.....	39
4.2.19 Caspase 3 activity measurement .....	39
4.2.20 Histology and immunohistochemistry .....	39
4.2.21 Macrophages isolation .....	40
4.2.22 Splenocytes isolation .....	40
4.2.23 Electrophoretic mobility .....	41
4.2.24 Serum biochemical estimation .....	41
4.2.25 Survival analysis .....	41
4.2.26 Statistical analysis.....	41
<b>5. RESULTS .....</b>	<b>43</b>
<b>5.1 siPLK1-StAv-SPIONs congregate the characteristics of superparamagnetic nanoparticles .....</b>	<b>43</b>
<b>5.2 PLK1 targeting by means of siPLK1-StAv-SPIONs impede tumor cell growth...50</b>	<b>50</b>
<b>5.3 Uptake of siPLK1-StAv-SPIONs is specific for tumor cells and depends on clathrin mediated endocytosis .....</b>	<b>54</b>
<b>5.4 siPLK1-StAv-SPIONs selectively taken up in the tumor and are detected by MRI imaging.....</b>	<b>60</b>
<b>5.5 siPLK1-StAv-SPIONs targeting hinder tumor burden and improves the disease response and overall survival.....</b>	<b>63</b>
<b>5.6 siPLK1-StAv-SPIONs represent pharmacokinetic profile suitable for in vivo delivery of siPLK1 to tumor .....</b>	<b>75</b>
<b>5.7 siPLK1-StAv-SPIONs though taken up by immune cells, do not influence immunostimulatory effects .....</b>	<b>76</b>
<b>5.8 siPLK1-StAv-SPIONs targeting to tumor halt tumor progression KPC mice .....</b>	<b>77</b>
<b>6. DISCUSSION.....</b>	<b>81</b>
<b>7. SUMMARY.....</b>	<b>95</b>
<b>8. ZUSAMMENFASSUNG .....</b>	<b>96</b>
<b>9. REFERENCES.....</b>	<b>97</b>
<b>10. APPENDICES .....</b>	<b>I</b>
<b>APPENDIX I.....</b>	<b>I</b>
<b>APPENDIX II.....</b>	<b>II</b>
<b>APPENDIX III.....</b>	<b>III</b>
<b>APPENDIX IV .....</b>	<b>V</b>
<b>11. ACKNOWLEDGEMENT.....</b>	<b>X</b>
<b>SCHRIFTLICHE ERKLÄRUNG .....</b>	<b>XI</b>

## LIST OF FIGURES

Figure 1: Graphical representation showing projected cancer related deaths by 2030. ....	3
Figure 2: Genetic progression model of pancreatic adenocarcinoma.....	5
Figure 3: Cell cycle mechanistic pathway showing G2/M transition. ....	7
Figure 4: Functional role of PLK1 .....	8
Figure 5: Role of PLK1 in malignant transformation.....	9
Figure 6: Structure of uMUC1 selective peptide, EPPT1 (a) and myristoylated poly-arginine peptide, MPAP (b) .....	19
Figure 7: schematic representation of siPLK1 coupled streptavidin conjugated dextran coated superparamagnetic iron oxide nanoparticles (siPLK1-StAv-SPIONs) .....	20
Figure 8: Physical characterization of siPLK1-StAv-SPIONs. ....	43
Figure 9: Surface characterization of siPLK1-StAv-SPIONs .....	44
Figure 10: Composition of siPLK1-StAv-SPIONs.....	45
Figure 11: SAED patterns for siPLK1-StAv-SPIONs, redrawn using diffraction ring profiler..	46
Figure 12: Evaluation of StAv (StAv) binding efficiency to SPIONs.....	47
Figure 13: siPLK1 binding evaluation to StAv-SPIONs .....	48
Figure 14: Electrophoretic mobility of siPLK1-StAv-SPIONs.....	48
Figure 15: <i>In-silico</i> modeling of siPLK1 binding to StAv .....	49
Figure 16: Quantitative analysis of the uptake of siPLK1-StAv-SPIONs into tumor cells.....	51
Figure 17: siPLK1-StAv-SPIONs are efficacious in silencing PLK1 and thus manifesting its effect on cell division .....	52
Figure 18: siPLK1-StAv-SPIONs are efficacious in reducing tumor cell proliferation <i>in vitro</i> .	53
Figure 19: <i>In vitro</i> tolerance on generation in reactive oxygen species on treatment of siPLK1-StAv-SPIONs .....	53
Figure 20: In solution stability of siPLK1-StAv-SPIONs.....	54
Figure 21: Immunofluorescence staining of MUC1 showing surface localization of the MUC1 on the pancreatic cancer cell-line, 6606PDA .....	54
Figure 22: Uptake of siPLK1-StAv-SPIONs is mediated by uMUC1 and MPAP .....	55
Figure 23: <i>In-vitro</i> uptake analysis of siPLK1-StAv-SPIONs using fluorescence associated cell sorting .....	56
Figure 24: Uptake of siPLK1-StAv-SPIONs is tumor specific and mediated by MUC1.....	57
Figure 25: Uptake of siPLK1-StAv-SPIONs is tumor specific and mediated by MUC1 as evaluated by FACS.....	57
Figure 26: Uptake of siPLK1-StAv-SPIONs is mediated by clathrin dependent endocytosis.	58
Figure 27: Uptake of siPLK1-StAv-SPIONs is mediated clathrin dependent endocytosis evaluated using FACS.....	59
Figure 28: Uptake of siPLK1-StAv-SPIONs is mediated clathrin dependent endocytosis evaluated using TEM imaging .....	59
Figure 29: Co-localization of siPLK1-StAv-SPIONs with endosomes.....	60
Figure 30: <i>In vivo</i> imaging of delivery of siPLK1-StAv-SPIONs to the tumor .....	61
Figure 31: <i>In vivo</i> MRI was performed on the mice bearing a syngenic orthotopic tumor before and 2 hours after intravenous administration of siPLK1-StAv-SPIONs.....	62
Figure 32: Perl's iron staining in tumors 6 hours after injection indicated presence of siPLK1-StAv-SPIONs inside the tumor (Blue), confirming delivery of siPLK1-StAv-SPIONs to the tumor.....	62
Figure 33: Influence of MPAP and EPPT1 on iron overload in tumor.....	62
Figure 34: Intracellular iron concentration in tumors 6 hours after siPLK1-StAv-SPIONs treatment.....	63

Figure 35: siPLK1-StAv-SPIONs arrest tumor progression in syngenic orthotopic tumor model .....	63
Figure 36: <i>In situ</i> tumor measurement using MRI showed stagnancy of tumor growth on siPLK1-StAv-SPIONs treatment. ....	64
Figure 37: Immunoblotting of PLK1 revealed a decrease in PLK1 expression the siPLK1-StAv-SPIONs treated group.....	65
Figure 38: Differential expression of PLK1 upon siPLK1-StAv-SPIONs treatment .....	65
Figure 39: Perl's Iron staining showing rapid clearance of siPLK1-StAv-SPIONs from tumors, liver and kidney .....	67
Figure 40: Influence of siPLK1-StAv-SPIONs treatment on PLK1 expression.....	69
Figure 41: Immunohistochemistry of Ki67 showing decrease proliferation on siPLK1-StAv-SPIONs .....	70
Figure 42: Tunel assay showing significant increase in apoptotic nuclei upon siPLK1-StAv-SPIONs treatment .....	71
Figure 43: Influence of siPLK1-StAv-SPIONs treatment on caspase 3 activity .....	71
Figure 44: Influence of siPLK1-StAv-SPIONs treatment on neo-angiogenesis .....	72
Figure 45: siPLK1-StAv-SPIONs treatment improves the survival in syngenic orthotopic tumor mouse model.....	73
Figure 46: Diagram illustrating the influence of siPLK1-StAv-SPION treatment on tumor volume over survival duration .....	73
Figure 47: Time dependent change in serum iron concentration after single dose of siPLK1-StAv-SPIONs.....	75
Figure 48: siPLK1-StAv-SPIONs did not influence the proliferation of macrophages. ....	76
Figure 49: siPLK1-StAv-SPIONs prevent tumor progression in LSL-Kras <sup>G12D</sup> ,LSL-Trp53 <sup>R172H</sup> , Pdx-1-Cre (KPC) mice.....	77
Figure 50: Quantitative RT-PCR and immunoblotting of PLK1 showed a decrease in PLK1 expression in the siPLK1-StAv-SPIONs treated group.....	78
Figure 51: siPLK1-StAv-SPIONs prevents tumor progression in LSL-Kras <sup>G12D</sup> ,LSL-Trp53 <sup>R172H</sup> , Pdx-1-Cre (KPC) mice by decreasing proliferation.....	79
Figure 52: siPLK1-StAv-SPIONs prevent tumor progression in LSL-Kras <sup>G12D</sup> ,LSL-Trp53 <sup>R172H</sup> , Pdx-1-Cre (KPC) mice by increasing apoptosis. ....	79
Figure 53: Change in PLK1 expression in KPC mice upon siPLK1-StAv-SPION treatment ..	80
Figure 54: Uptake and release mechanism of siPLK1-StAv-SPIONs.....	91
Figure 55: Schematic diagram illustrating biotin binding sites evaluation using TRITC-Streptavidin substrate.....	IV
Figure 56: siPLK1-StAv-SPIONs uptake by splenocytes 30 min after treatment. ....	V

## LIST OF TABLES

Table 1: PLK1 expression in different human tumors .....	10
Table 2: Drugs currently being evaluated as PLK1 inhibitors .....	11
Table 3: Novel approaches to specifically target PLK1 .....	13
Table 4: Different theranostics agents used for biomedical applications .....	15
Table 5: Different categories of SPIONs.....	16
Table 6: The composition of siPLK1-StAv-SPIONs as determined by Energy-dispersive X-ray spectroscopy .....	45
Table 7: Physiochemical characterization of siPLK1-StAv-SPIONs .....	47
Table 8: Stoichiometric calculations for binding and conjugation on SPIONs.....	50
Table 9: Table showing change in clinical serum parameters on the treatment of siPLK1-StAv-SPIONs in syngenic orthotopic tumor mice .....	68
Table 10: Table showing changes in cytokine and chemokines on the treatment of siPLK1-StAv-SPIONs in tumor bearing mice.....	74
Table 11: Table illustrating pharmacokinetic profiling following intravenous administration of siPLK1-StAv-SPIONs. ....	76
Table 12: Most commonly used site specific delivery carriers.....	85
Table 13: Different types of multifunctional SPIONs for cancer theranostics.....	87
Table 14: JCPDS card for Magnetite .....	1

## ABBREVIATIONS

°C	Grad Celsius
µg	Microgram = 10 <sup>-6</sup> Gram
µl	Microliter = 10 <sup>-6</sup> Liter
APS	Ammonium persulfate
BCA	Bicinchoninic acid
Bp	Base pair
BSA	Bovine serum albumin
CBA	Cytokine bead array
CCK-BR	Cholecystokinin B receptor
CDK	Cyclin dependent kinases
cDNA	Complementary DNA
COX	Cyclo-oxygenase
CT	Computer tomography
DAB	3,3' diaminobenzidine
DAPI	4'6-diamidino-2-phenylindile
DCFDA	Dichloroflourrescein diacetate
DMEM	Dulbecco's Modified Eagle Medium
DMSO	Dimethylsulfoxide
DNA	Deoxyribonucleic acid
DTT	Dithiothreitol
ECL	Enhanced chemiluminescence
EDTA	Ethylenediamine tetraacetate
EDX	Energy dispersive X ray spectroscopy
EEA1	Early endosomes antigen 1
EGFR	Epidermal growth factor receptor
FACS	Flow associated cell sorting
FCS	Fetal calf serum
G	Gravitation force g (9,897 m/s <sup>2</sup> )
GAPDH	Glyceraldehyde 3-phosphate dehydrogenase
GEMM	Genetically engineered mouse model
H	hours
HE	Haematoxylin-Eosin
HEPES	Hydroxyethyl piperazine N'-2-ethane sulfonic acid
HGF	Hepatocytes growth factor
HRP	Horse radish peroxidase
HRTEM	High resolution transmission electron microscopy

i.v.	Intra venous
IGF1	Insulin like growth factor 1
IPMN	Intraductal papillary mucinous neoplasm
kDa	Kilo Dalton = 10 <sup>3</sup> Dalton
KPC	LSL-Kras <sup>G12D</sup> , LSL-Trp53 <sup>R172H</sup> , Pdx-1-Cre
M	Molar
mA	Milliampere = 10 <sup>-3</sup> Ampere
MACS	Magnetic associated cell sorting
MAPK	Mitogen activated phosphokinases
MCN	Mucinous cystic neoplasm
MDC	Monodansylcadaverine
Mg	Milligram = 10 <sup>-3</sup> Gram
Min	Minutes
ml	Milliliter = 10 <sup>-3</sup> Liter
mM	Millimolar
MMPs	Matrix metalloproteases
MRI	Magnetic resonance imaging
mRNA	Messenger RNA
MW	Molecular weight
NFκB	Nuclear factor κB
Ng	Nanogram = 10 <sup>-9</sup> Gram
Nm	Nanometer = 10 <sup>-9</sup> Meter
OD	Optical Density
PanINs	Pancreatic intraepithelial neoplasia
PBS	Phosphate buffered saline
PCR	Polymerase chain reaction
PDAC	Pancreatic ductal adenocarcinoma
PDT	Photodynamic therapy
PET	Positron emission tomography
PI3K	Phosphatidylinositol 3 kinases
PLK1	Polo-like kinases 1
PMSF	Phenylmethylsulphonyl fluoride
PSMA	Prostate specific membrane antigen
RAS	Renin angiotensin system
Rb	Retinoblastoma protein
RES	Reticular endothelial system
RISC	RNA-induced silencing complex

RNA	Ribonucleic acid
ROI	Region of interest
ROS	Reactive oxygen species
Rpm	Revolutions per minute
SD	Standard deviation
SDS	Sodium deodecyl sulfate
SHh	Sonic Hedgehog
siRNA	Small interfering RNA
SPECT	Single photon emission computed tomography
SPIONs	Superparamagnetic nanoparticles
TBE	Tris borate EDTA
TBS	Tris buffer saline
TBST	Tris buffer saline Tween 20
TEMED	Tetramethylethylenediamine
TNF $\alpha$	Tumor necrosis factor alpha
Tris	Trishydroxymethylaminomethane
U	Units
uMUC1	Underglycolated Mucin 1
uPA	Urokinase-type plasminogen activator
V	Volt
v/v	Volume/volume
w/v	Weight/volume





## 1. INTRODUCTION

While pancreatic malignant tumors display a variety of histological forms, the term 'pancreatic cancer' is usually synonymous with a pathological diagnosis of pancreatic ductal adenocarcinoma (PDAC). PDAC is one of the most aggressive malignancy burdened with an especially dismal prognosis<sup>1</sup>. Given the importance of the regulation of the cell division cycle and its high fidelity execution to organismal homeostasis, it is unsurprising that alteration of the cell cycle is a hallmark of the pathogenesis human malignancies<sup>2</sup>. Importantly, many of the genes encoding key regulators of the cell cycle are mutated in both sporadic and hereditary forms of cancer including pancreatic<sup>3</sup>. Given possible role of Polo-like kinases (PLKs) in the centrosome cycle, it is expected that deregulated expression of PLKs is detected in many types of cancer and is associated with oncogenesis. PLK1 overexpression has been observed in wide range of tumor types and is often associated with a poor prognosis<sup>4</sup>. Overexpression of PLK1 was detected in both pancreatic cancer cell lines as well as in tumors of PDAC patients<sup>5,6</sup>. Several PLK1 specific small molecule inhibitors have been restricted to phase II and phase III trials, but owing to its non-specificity, chemoresistance and toxicity (Febrile neutropenia, myelosuppression and neuropathies), their clinical use is limited<sup>7</sup>.

Despite the knowledge and insights into biological properties and genetic aberrations of malignant cells, therapeutic options of PDAC remain incompletely effective and transitory. One plausible explanation for this futile response is insufficient delivery of anticancer drugs to the tumour site<sup>8,9</sup>.

The use of siRNAs that allow specific intervention at single molecular stages of the disease may provide a potential therapeutic agent. siRNAs virtually can be used to inhibit the expression of any gene. Major hurdles of *in vivo* delivery of siRNAs are the adequate and delivery to the specific site of interest, stability of siRNAs in serum and non-invasive monitoring of the influence of siRNAs.

The objective of the present study is to evaluate the potential of siRNA conjugated to dual purpose superparamagnetic iron-oxide-nanoparticles (SPIONs) for the therapeutic intervention of PDAC functioning as theranostics. Theranostics are the materials that combine the modalities of therapy and diagnostic imaging such that it delivers therapeutic drugs as well as diagnostic imaging agents concurrently within same dose<sup>10</sup>. Although the feasibility of using SPIONs for cancer detection and drug delivery has been demonstrated<sup>11</sup>, a major obstacle limiting their clinical application is that non-targeted nanoparticles are unable to reach sufficient concentrations in the tumor site to either produce a strong signal for tumor imaging or to carry optimal amounts of therapeutic agents into tumor cells.

Keeping the limitations of classical PDAC therapy, *in vivo* delivery of siRNA and drug delivery properties of SPIONs in mind, we have developed a novel formulation that not only deliver the siRNAs adequately and specifically to the tumor site but also allow non-invasive imaging of the uptake of our therapeutic agent. In order to accomplish this, we designed dual purpose functional probes with dextran coated superparamagnetic nanoparticles as a backbone which can be detected by magnetic resonance imaging (MRI) and which are further conjugated to streptavidin. Reflecting the fact of streptavidin and biotin as the strongest covalent binding, we coupled biotin conjugated myristoylated polyarginine peptides (MPAPs) for translocation of the complex into the cytosol by electrostatic interaction as well as biotin conjugated EPPT1, a non-immunogenic underglycosylated MUC1 antigen highly specific for MUC1 protein, (a trans-membrane protein, highly expressed in pancreatic ductal adenocarcinoma) which allows tumor specific intake. Furthermore we linked biotin conjugated siRNAs directed against PLK1 to the streptavidin anchor to be used as a therapeutic target. Administrations of these nanoparticles in tumor-bearing mice allowed monitoring of delivery of the agent to the tumor and metastasis by MRI imaging and results in efficient silencing of the target gene, *PLK1*. This approach can significantly advance the therapeutic potential of siRNAs by providing a way not only to effectively shuttle siRNA to target sites but also to noninvasively access the bioavailability and efficacy of the siRNA at tumor site.

## 2. THEORETICAL BACKGROUND

Pancreatic cancer can basically be divided into two major subtypes: adenocarcinoma, which originates in the exocrine portion of the pancreas (95% of cases), and rare endocrine tumors, which originate from islet cells. As its name implies, PDAC is presumed to arise from pancreatic ductal epithelial cells. These tumors typically display a distinct duct-like histology and express markers of ductal differentiation<sup>1</sup>.

### 2.1 Pancreatic ductal adenocarcinoma

PDAC continues to pose an enormous challenge to clinicians owing to its unfavorable prognosis. The global incidence of pancreatic cancer is rising. PDAC is an aggressive malignant disease of the exocrine pancreas with a 5-year survival rate of less than 5% and is the fourth leading cause of cancer-related deaths<sup>12,13</sup>. PDAC is projected to be the second leading cause of cancer-related deaths by 2030<sup>14</sup> (**Figure 1**).

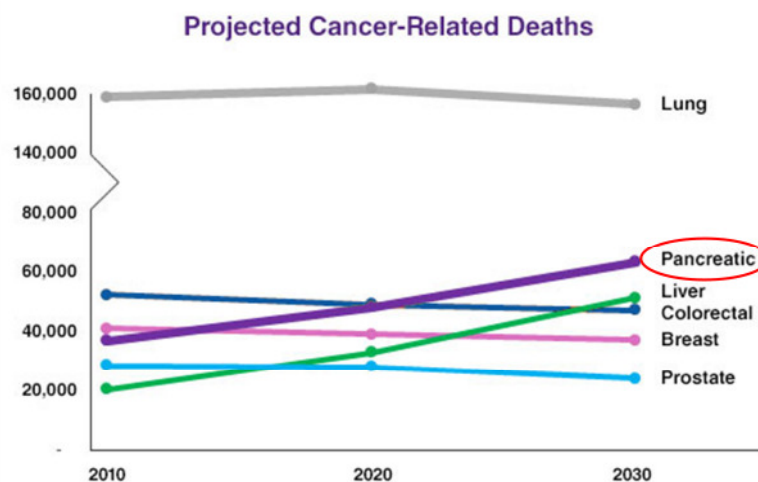


**Figure 1: Graphical representation showing projected cancer related deaths by 2030.** (Figure adopted from Rahib *et al*, 2014)

Dismal prognosis is a result of the late diagnosis of the disease, the lack of biomarkers allowing early screening, the early metastatic dissemination, and ultimately the resistance to systemic therapies. Poor prognosis results from the aggressive nature of the disease, with as many as 90% of patients at the time of diagnosis harboring unresectable cancer that is extremely resistant to chemotherapy<sup>15</sup>. Furthermore, only about 20% of patients resected in curative orientation survive longer than 5 years<sup>16</sup>. Without active treatment, metastatic PDAC has a median survival of 3 to 5 months and 6 to 10 months for locally advanced disease. The late presentation and aggressive tumor biology of this disease allow only a minority (10 to 15%) of patients to undergo potentially curative surgery<sup>17,18</sup>. Unfortunately, post-surgically, most patients still relapse despite adjuvant systemic therapies.

## 2.2 Factor predisposing to PDAC:

Both genetic and modifiable risk factors contribute to the development of PDAC. A hereditary component has been identified in approximately 10% of cases, with a specific germline mutation being implicated in 20% of those cases<sup>19,20</sup>. Modifiable risk factors for this malignant disease include smoking, family history of chronic pancreatitis<sup>21,22</sup>, advancing age, male sex, diabetes mellitus<sup>23</sup>, obesity, non-O blood group, occupational exposures (e.g, to chlorinated hydrocarbon solvents and nickel), African-American ethnic origin, a high-fat diet, diets high in meat and low in vegetables and folate, and possibly *Helicobacter pylori* infection and periodontal diseases<sup>12,20,24</sup>.

## 2.3 Pathogenesis of pancreatic cancer:

PDAC is defined as a malignant epithelial neoplasm of the pancreas in which the neoplastic epithelial cells focally form glands. PDAC is fundamentally a disease of inherited and acquired mutations in cancer-related genes and its implications in dysregulated molecular signaling. Dysregulated molecular signaling and the accumulation of genetic changes over time result in incremental changes in pancreatic epithelium ranging from preinvasive precursor lesions to invasive carcinoma. Pancreatic intraepithelial neoplasias (PanINs) are the most common lesions found in preinvasive carcinoma. PanIN1A lesions are flat, tall columnar cells with basally located nuclei; PanIN1B lesions show papillary architecture; PanIN2 lesions exhibit nuclear abnormalities, such as a loss of polarity or nuclear crowding; PanIN3 lesions have marked nuclear and cytologic abnormalities and represent the lesions previously referred to as carcinoma *in situ*. Invasion through the basement membrane marks the transition from PanIN3 to invasive Carcinoma. Histological progression of PanINs lesions is analogous to progressive accumulation of genetic aberrations (**Figure 2**)<sup>12,25,26</sup>. Other variants of preinvasive lesions include intraductal papillary-mucinous neoplasms (IPMN) and Mucinous cystic neoplasms (MCN).

The genes targeted in pancreatic cancer include oncogenes (*KRAS*, *BRAF*, *AKT2*, *MYB* and *AIB1*), tumor-suppressor genes (*p16/CDKN2A*, *TP53* and *SMAD4*) and genome-maintenance genes (*MLH1*, *MSH2*, *BRAC2* and other Fanconi anemia genes)<sup>27,28</sup>. The activation of oncogenes and inactivation of tumor suppressor genes are partly responsible for the initiation and progression of PDAC<sup>27-29</sup>. Furthermore the dysfunction of molecules in several cell signaling pathways, such as EGFR, PI3K-Akt, NFκB, Hedgehog signaling etc. and their molecular crosstalk also play important roles in the molecular pathogenesis of pancreatic cancer<sup>27-31</sup>.

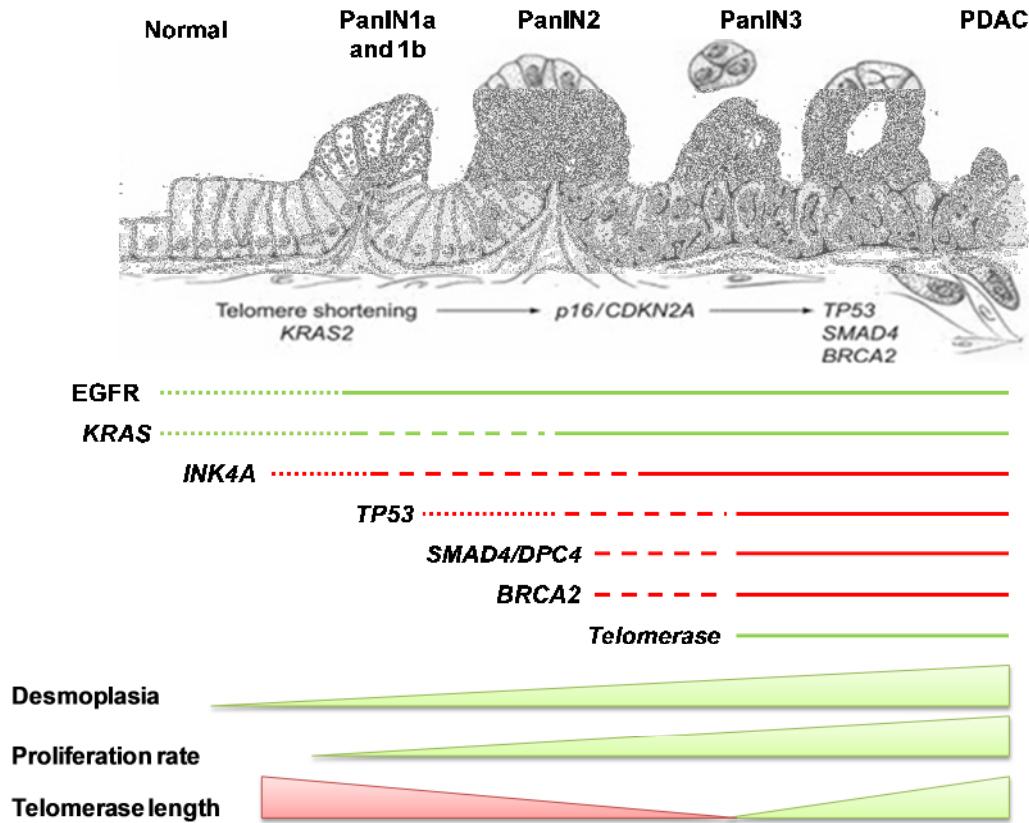


**Figure 2: Genetic progression model of pancreatic adenocarcinoma.** Pancreatic intraepithelial neoplasia (PanINs) seems to represent progressive stages of neoplastic growth that are precursors to pancreatic adenocarcinoma. The genetic alterations documented in adenocarcinoma also occur in PanIN in what seems to be a temporal sequence, although these alterations have not been correlated with the acquisition of specific histopathological features<sup>12,25,32</sup>.

Oncogenes are genes that once activated by means of mutations (point mutation, amplifications etc.), contribute to oncogenesis. The activation of the *RAS* oncogene has been found in more than 90% of PDAC<sup>33</sup>. The *RAS* gene family is involved in signal transduction and mediates pleiotropic effects including cell proliferation and migration. The *KRAS* gene on chromosome 12p is activated in >90% of pancreatic cancers<sup>31</sup>. It has been found that approximately 80-90% of PDAC harbor point mutations in *KRAS*<sup>33</sup>. The point mutation leads to the generation of a constitutively active form of ras. The constitutively activated ras binds to GTP and gives uncontrolled stimulation signals to downstream signaling cascades, promoting uncontrolled cell growth. *KRAS* mutation in pancreatic cancer typically develops during the early phase of carcinogenesis and patients with *KRAS* mutation have a shorter survival time than patients with the wild-type *KRAS*, suggesting that the mutation of *KRAS* is partly responsible for the initiation and progression of pancreatic cancer<sup>1,27,31</sup>.

One-third of the PDAC with wild-type *KRAS* have mutations in *BRAF* gene, which regulates RAF-MAP signaling pathway<sup>34</sup>. The *BRAF* and *KRAS* mutations appear to be mutually exclusive in pancreatic cancers. The mutual exclusivity in the mutation status of these two genes suggests that the RAF-MAP signaling pathway plays a critical role in mediating cancer

causing signals in the RAS pathway<sup>31</sup>. These mutations contribute to the uncontrolled cell proliferation either by alteration of cell cycle or evading cell cycle check points,

#### **2.4 Alteration of cell cycle during progression of pancreatic cancer:**

Several families of protein kinases orchestrate the complex events that drive the cell cycle and their activity is frequently deregulated in hyperproliferative cancer cells<sup>35</sup>. Within the human genome, approximately 300 genes have been found to be mutated in cancer and many more exhibit altered levels or patterns of expression. Such changes contribute to deregulation of cell cycle kinases which is often associated with aberrant division and uncontrolled proliferation of cancer cells<sup>36</sup>.

During the mammalian cell cycle, progression through G<sub>1</sub> phase and initiation of the DNA synthesis (S phase) is cooperatively regulated by several cyclins and their associated cyclin dependent kinases (CDKs) which integrate the flow of information from extracellular mitogenic stimuli, including growth factor signaling and the availability of nutrients<sup>37</sup>. When cells in the quiescent G<sub>0</sub> phase enter the cycle, CDK4 and CDK6 form active complexes with D type cyclins (D1, D2 and D3) and initiate phosphorylation of the retinoblastoma protein (Rb1; also known as p105) and possibly other members of the pocket protein family which inactivates their function as transcriptional repressors<sup>38</sup>. In late G<sub>1</sub>, active CDK2-cyclin E heterodimers reinforce Rb1 phosphorylation on additional sites to irreversibly initiate the gene expression of the S phase<sup>39,40</sup>. This stage, called the 'restriction point', is crucial in cancer as alterations in the key regulatory players in the G<sub>1</sub> to S phase transition could allow cells to proliferate independently of mitogenic stimuli. Beyond the restriction point, Rb1 is maintained in a hyperphosphorylated state by the sequential activities of cyclin A-CDK2, cyclin A-CDK1 and cyclin B-CDK1 complexes, thereby ensuring cell cycle progression **(Figure 3)**<sup>41,42</sup>.

In parallel with DNA replication, the centrosome cycle begins. Centrosomes duplicate during late S phase to early G<sub>2</sub> phase and separate to form the poles of the mitotic spindle at the beginning of mitosis<sup>43,44</sup>. They then begin maturation process in which each centrosome nucleates its own aster of dynamic microtubules radiating from both poles of the mitotic spindle. These processes are controlled by both CDK1 and CDK2 as well as other serine threonine protein kinases, including aurora A and polo-like-kinase 1 (PLK1)<sup>45</sup>.

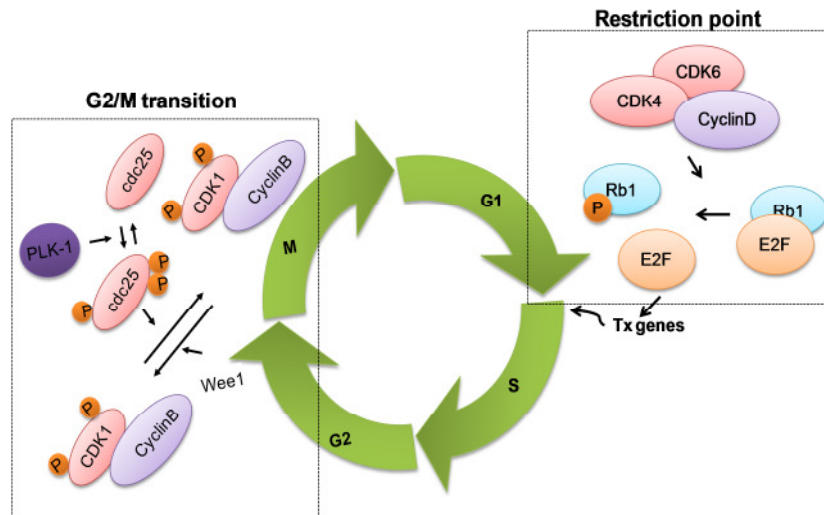


**Figure 3: Cell cycle mechanistic pathway showing G2/M transition.**

A complex regulatory network controls the activity of the principal mitotic regulatory kinase, CDK1. Cyclin B that is required for CDK1 activity accumulates during G<sub>2</sub> phase. However, the newly formed CDK1-cyclinB complex is maintained in an inactive state by the Wee1 and membrane-associated Cdk1-inhibitory kinase (Myt1) kinases. Activation of the CDK1-cyclinB complex occurs when the activity of the dual specificity phosphatase Cdc25 overcomes the effect of the opposing kinases Wee1/Myt1, which results in the dephosphorylation of CDK1. PLK1 Regulates the activities of Cdc25 and Myt/Wee1<sup>46</sup>. In complex with cyclin A, CDK1 is abruptly activated at the transition from the G<sub>2</sub> phase to the mitosis (M) phase to facilitate the commencement of mitosis through regulation of chromosome condensation and microtubule dynamics<sup>45</sup>. Following nuclear envelope breakdown, cyclin A is degraded and newly formed cyclin B-CDK1 complexes are required for progression through the M phase. Ultimately, for complete division into two daughter cells, CDK1 activity must be switched off; this occurs by proteolysis of cyclin B by the anaphase-promoting complex or cyclosome<sup>2</sup>. When mitosis begins, chromosomes become condensed. In the subsequent stage of metaphase, both sister chromatids of each duplicated chromosome pair are attached through their kinetochores to the microtubules of the mitotic spindle, and aligned to the spindle midzone for the following equal segregation at the two spindle poles during anaphase<sup>47</sup>. Cytokinesis is the final stage of cell division that splits a cell into two. The process initiates in anaphase with the localisation of a microtubule associated protein complex to the cell equator and the subsequent assembly and constriction of an actomyosin based contractile ring coordinated by the Rho signaling pathway<sup>45</sup>. Recent studies in mammals suggested that the activity of Polo kinase peaks in anaphase and telophase suggesting a role in cytokinesis<sup>42</sup>. PLK1 has been shown to have a pivotal role in regulating the cell cycle at G<sub>2</sub>/M phase, including entry into mitosis, centrosome maturation, assembly of the bipolar spindle, sister chromatid

splitting, activation of ubiquitin ligase, anaphase-promoting complex/cyclosome and exit from mitosis with the initiation of cytokinesis<sup>45</sup>.

#### 2.4.1 Polo like kinases (PLKs):

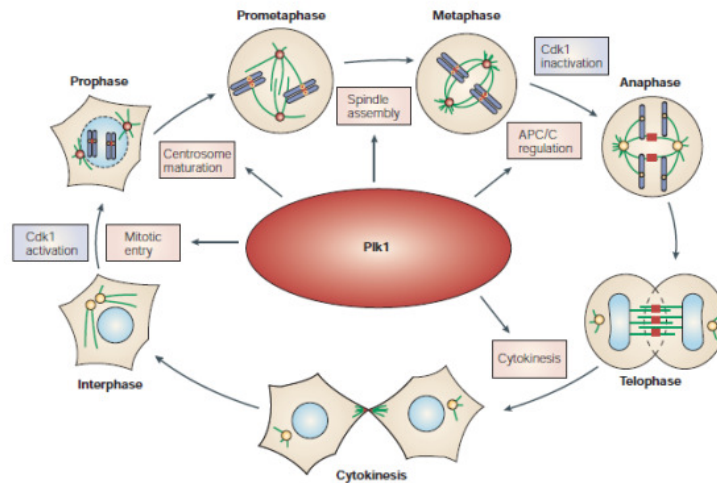


**Figure 4: Functional role of PLK1** (Figure adopted from Barr *et al* 2004)

The PLK family belongs to highly conserved family of mitotic serine/threonine kinase and comprises four structurally related but functionally distinct proteins: PLK1, PLK2 (also known as SNK), PLK3 (also known as FNK and PRK) and PLK4 (also known as SAK)<sup>48,49</sup>. PLK1 is the best-characterized family member, and several studies describe its essential and vital functions for activation of the CDK1-cyclin B complex at the G<sub>2</sub>/M phase transition, centrosome maturation, spindle formation, chromosome segregation kinetochores functions, sister chromatid cohesion and cytokinesis. Recently, a role for PLK1 in regulating aurora A localization and activity on centrosomes was also discovered (**Figure 4**)<sup>39</sup>. PLK activity is regulated both in time and space. Temporal control is achieved by transcriptional regulation, phosphorylation and proteolysis; spatial control is achieved by protein interactions that localize the enzymes<sup>50</sup>.

#### 2.4.2 The role of PLK1 in malignant transformation:

Deregulated centrosome duplication or maturation results in increased centrosome size and centrosome number which show a significant correlation with aneuploidy and chromosomal instability, thus contributing to cancer formation. Given the role of Polo-like kinases (PLKs) in the centrosome cycle, it is expected that deregulated expression of PLKs is detected in many types of cancer and is associated with oncogenesis. PLK1 overexpression has been observed in wide range of tumor types and is often associated with a poor prognosis<sup>4</sup>. Furthermore, PLK1 mutations could play a part in tumorigenesis<sup>41</sup>. PLK1 is an attractive anticancer target because targeted interference in PLK1 function induces prolonged mitotic arrest and subsequent onset of apoptosis. Thus, PLK1 inhibition could potentially have the

same effect as the microtubule toxins in causing mitotic arrest, without disrupting microtubule dynamics in non-cycling cells, thereby evading the adverse effects arising from tubulin interference in non-cancerous cells. Moreover, normal cells seemed to be less sensitive to PLK1 depletion than transformed cells (**Figure 5**)<sup>40,45,48,51</sup>.

The observation that the kinase domain of PLK1 physically binds to the DNA binding domain of p53, thereby inhibiting both the trans-activation activity and the apoptosis-inducing function of p53, provided the first evidence of a direct relationship between PLK1 and p53<sup>52</sup>. It was discovered that the topoisomerase-I binding protein topors is phosphorylated on Ser718 by PLK1<sup>48</sup>. The tumor suppressor p53, which is disrupted in more than 50% of human cancers, is of central importance in the cellular response to DNA damage and other cellular stresses. Normal functioning of p53 maintains the stability of the genome and is a potent barrier to cancer development<sup>16,17</sup>. Its activation leads to the trans-activation of target genes and the induction of growth arrest or apoptosis, which depends on the severity of the damage in a specific cellular context<sup>48,52</sup>.

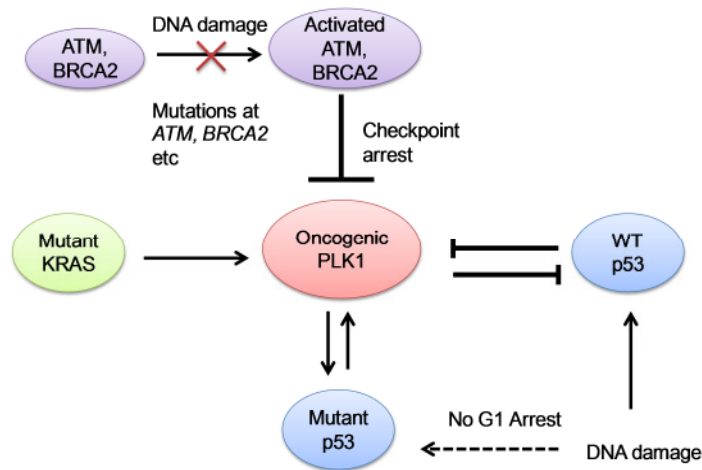


**Figure 5: Role of PLK1 in malignant transformation**<sup>53</sup>

Phosphorylation of topors by PLK1 inhibits sumoylation of p53 and simultaneously enhances the ubiquitylation of p53. This leads to the degradation of p53 and therefore supports the role of PLK1 as a negative regulator of p53. The long-term downregulation of PLK1 correlates with reduced levels of MDM2, a p53-specific E3 ubiquitin ligase that acts as a p53 antagonist<sup>48</sup>. This suggests that the mutual regulation of PLK1 and p53 occurs at multiple molecular levels. Furthermore, studies that describe its interplay with various other tumor suppressor proteins indicate that PLK1 is a central player in the development of human cancer. Although the PLK1-mediated control of the tumor suppressors p53 probably supports mitotic progression<sup>54</sup>, the activity of PLK1 is negatively regulated by several checkpoint pathways, including those involving *ATM*, *ATR*, *BRCA1* and *CHK1*<sup>35,44</sup>. Thus, an upstream event, such as the inactivation of p53, might suffice to tip the balance towards malignant

progression by inducing a series of events that lead to the upregulation of the activity of PLK1, followed by a further weakening of the tumor suppressors<sup>2</sup>.

Although the evidence for PLK1 as an oncogene continues to be limited<sup>49</sup>, evidence suggests the role of elevated PLK1 activity as a tumor promoting force. This increase in PLK1 activity stimulates mitotic transcriptional programmers<sup>55</sup>; overrides the DNA damage checkpoint<sup>56</sup>; contributes to checkpoint adaptation<sup>57</sup>; supports the invasion through the extracellular matrix<sup>3,4,57</sup> and paves the way for aneuploidy as a key feature of carcinogenesis<sup>37,58</sup>.

### 2.4.3 Dysregulated PLK1 in human cancers

PLK1 as a tumor promoting force prompted a number of studies that subsequently demonstrated that PLK1 is overexpressed in a broad spectrum of human tumors compared with normal controls (**Table 1**). Analyses of these clinical data revealed expression levels of PLK1 positively correlate with tumor progression and poor patient survivals.

Overexpression of PLK1 was detected in both pancreatic cancer cell lines as well as in tumors harvested from patient harboring PDAC<sup>5,6</sup>. Owing to its characteristics of regulating G<sub>2</sub>/M transition and thus regulating mitosis, its connections to mutant KRAS and p53 and its regulatory cross-talk with p53, oncogenic PLK1 represents attractive selective target for anticancer therapy. The added advantage of PLK1 targeting is that normal cells are less susceptible to cell cycle arrest at G<sub>2</sub>/M transition on PLK1 depletion compared to that of cancer cells<sup>59</sup>. This supports the notion of PLK1 as feasible cancer therapy target.

**Table 1: PLK1 expression in different human tumors**<sup>48,51,60</sup>

Tumor	Overexpression of PLK1	Prognostic potential	Influence on survival with moderate expression compared to high expression
Non-small-cell lung Carcinoma	Yes	Yes	(5 year survival) 51.8%,P=0.0001
Oropharyngeal carcinoma	Yes	Yes	(5 year survival) 59.8%,P=0.013
Oesophageal carcinoma	Yes	Yes	(3 year survival) 54.9%,P<0.05
Gastric carcinoma	Yes	No	-
Melanomas	Yes	Yes	(10 year survival) 93.6%,P=0.03
Breast cancer	Yes	No	-
Ovarian cancer	Yes	ND	-
Endometrial cancer	Yes	ND	-
Colorectal cancer	Yes	Yes	-
Glioblastoma	Yes	ND	-
Papillary carcinoma	Yes	No	-
Pancreatic cancer	Yes	ND	-

Tumor	Overexpression of PLK1	Prognostic potential	Influence on survival with moderate expression compared to high expression
Prostate cancer	Yes	No	-
Hepatoblastoma	Yes	Yes	-
Non-Hodgkin Carcinoma	Yes	Yes	-
Head and Neck cancer	Yes	ND	(5 year survival) 43%,P=0.0047

#### 2.4.4 PLK1 targeting in cancer therapy

Several PLK1 inhibitors have been developed as an anticancer therapeutic strategy. Some of these inhibitors are listed in **Table 2**. Some of these inhibitors are currently under preclinical development while others are undergoing clinical trials. Most of the drugs undergoing clinical trials showed marginal benefits owing to direct drug related adverse effects.

**Table 2: Drugs currently being evaluated as PLK1 inhibitors**<sup>48,61-67</sup>

Compound	Phase	Mechanism of Action	Direct drug related Adverse events
BI 2536	II	ATP-competitive inhibitor	Neutropenia, leucopenia, nausea, fatigue
BI 6727	I/II	ATP-competitive inhibitor	Reversible thrombocytopenia, Neutropenia and febrile neutropenia
Compound 36	Preclinical	ND	ND
CYC-800	Preclinical	ND	ND
Cyclapolin 1	Preclinical	Non-competitive with respect to ATP	ND
DAP-81	Preclinical	Predicted to target the nucleotide pocket	ND
GSK461364	I	ATP-competitive inhibitor	Neutropenia, thrombocytopenia, venous thrombotic emboli, myelosuppression
HMN-176	Preclinical	Alters spatial distribution of PLK1	ND
HMN-214	I	Prodrug of HMN-176	Myalgia, bone/pain syndrome, hyperglycemia, noncardiac chest pain
LFM-A13	Preclinical	binding to the catalytic site of the Plx1 kinase domain	ND
NMS-P937	I	ATP-competitive inhibitor	ND
Poloxin	Preclinical	Interferes with PLK1 PBD functions	ND
Poloxipan	Preclinical	Pan-specific inhibitor of the PBDs of PLK1	ND

Compound	Phase	Mechanism of Action	Direct drug related Adverse events
Purpurogallin	Preclinical	Inhibits PBD-dependent binding	ND
Rigosertib	II	Affects microtubule dynamics	Dysuria, haematuria, nocturia and cystitis, abdominal pain, Atrial fibrillation
TAK-960	I	ND	Terminated because of serious adverse effects

#### 2.4.4.1 Issue with PLK1 inhibitors

Jimeno *et al*<sup>68</sup> describe a phase I study with an accelerated titration dose-escalation design of Rigosertib, a small-molecule PLK1 inhibitor, is believed to compete for the substrate-binding site of PLK1. The second phase I study by Mross *et al*<sup>64</sup> explores BI2536, a highly potent (low nanomolar inhibitory concentration by 50%) PLK1 inhibitor in a traditional 3+3 escalation scheme. Traditional phase I trial designs were pursued in both trials with pharmacokinetic evaluation; pharmacodynamic studies were not pursued in either trial. Despite this, in the trial of BI2536, the typical toxicity of mitotic inhibitors, febrile neutropenia, was reported as the dose-limiting toxicity; this supports target blockade in surrogate tissue with BI2536 and further evaluation in phase II trials. Given the similarities between the known cell death pathways induced by antimitotics, it will be important to define biomarkers predictive of response and to identify whether these new agents demonstrate efficacy in disease compared to nonspecific effects. It is important to note that nonspecific inhibition of cell cycle inhibitors lead to direct dose related adverse events leading to compromise clinical outcome.

#### 2.5 Lack of efficacy traditional cancer therapy

Developments in last decades in cancer chemotherapy were successful to most of cancers, however, results remained poor on treating certain solid tumors such as breast, colon, lung and pancreatic cancer is still less impressive. Two important factors contribute to this ineffectiveness. First, heterogeneity of the tumor, in which tumor cells are surrounded by non-cancerous stromal cells, immune cells, lymphatic cells and extra-cellular matrix. These subpopulations of cells differ widely in their response to cytotoxic drugs and other therapeutic modalities and therapy is only successful if this diversity can be taken into account. Second, the lack of selectivity of most anticancer drugs for tumor cells poses risk of significant toxicity to normal tissues resulting in suboptimal therapy<sup>8,9</sup>.

The efficacy of anticancer drugs can also be limited by poor diffusion to certain areas of the tumors, because of a number of penetration barriers related to the abnormal neovasculature and altered composition of tumor tissue. Therefore, strategies aimed at increasing the

selectivity and amounts of chemotherapeutics delivered to tumor areas could increase the therapeutic index of these class of compounds<sup>69,70</sup>.

Novel delivery systems allow clinical use of new therapeutics, are permitting anticancer therapy with significantly reduced side effects, and have enabled new and better chemotherapeutic regimens using existing pharmaceuticals. Drug delivery systems have also facilitated cancer prevention as well as the pain management associated with cancer progression and chemotherapy<sup>71</sup>.

## 2.6 Novel treatment approach with PLK1

PLK1 inhibitors found to be efficacious in some of the clinical trials, still, their effectiveness is limited by two critical aspects: chemoresistance and toxicity (Febrile neutropenia, myelosuppression and neuropathies)<sup>7</sup>. In attempt to avoid severe adverse side effects related to small molecule inhibitors, novel therapeutic approaches were explored in recent past. Some of these novel approaches are enlisted in **Table 3**. Specific targeting PLK1 through the aid of these approaches hold much promise for the treatment of a wide range of human cancers.

The emergence of nanotechnology has offered an opportunity to draw diagnosis and therapy closer. Implementation of novel treatment approaches with added advantage of nanoparticles in diagnosis pave the way for co-delivery or "Theranostics". One underlying driving force of such a combination is that imaging and therapy both require sufficient accumulation of agents in diseased areas. This common targeting requirement brings the two research domains closer and, ultimately, will blur the boundary between them, since many techniques to enhance imaging can, at least in theory, be readily transferred to the therapeutic domain, and vice versa.

**Table 3: Novel approaches to specifically target PLK1**

Approaches to targeting PLK1	Characteristics	Phenotypes	References
<b>Antisense oligonucleotide</b>	Antisense oligonucleotides targeted against PLK1 coupled with Human serum albumin nanoparticles. <i>cell-type specific targeted delivery</i>	HER2-Positive and negative breast cancer cell-lines	72
<b>Aptamers</b>			
Aptamers-siRNAs chimeras	siPLK1 coupled with prostate specific membrane antigen (PSMA) targeted aptamers. <i>specific, intratumoral delivery</i>	Prostate carcinoma	73,74
<b>siRNAs targeted against PLK1</b>			
Nanoparticles	siRNAs targeted against PLK1 conjugated to either to metallic nanoparticles (Iron oxides, Carbon nanotubes, gold nanoparticles, and	Different cell-lines and orthotopic tumor models	75-80

Approaches to targeting PLK1	Characteristics	Phenotypes	References
	silica nanoparticles), cholesterol conjugates, Polycationic nanoparticles, antibody conjugates, stable nucleic acid lipid nanoparticles, Liposomes, dendrimers or cationic lipid assisted Polyethylene glycol-poly ( <i>D</i> -lactide) nanoparticles. <i>siRNA retain its integrity within the nanoparticles, effectively internalized by cancer cells and easily escaped from the endosomes</i>	with cell-lines transfected in nude mice	
Virus-like particles	siRNAs targeted against PLK1 delivered with non-virulent virus like vectors. <i>Due to their intrinsic mechanism for gene transduction, viruses readily function as vectors in a cost-effective and delivery-efficient way</i>	Different cell-lines	81
<b>Microinjections of PLK1 antibodies</b>	Anti-PLK1 antibodies microinjected in cytoplasm. <i>Cells injected with anti-PLK1 antibodies displayed defects in its ability to assemble a bipolar spindle</i>	HeLa cells and Hs68 human cells	82
<b>shRNAs targeted against PLK1</b>	Plasmids expressing shRNAs targeted to human PLK1 and driven by a human U6 promoter. <i>Combination of gene silencing with effective in vivo delivery generate long lasting signal.</i>	HeLa S3 cervical and A549 lung cancer cell-lines transfected nude mice	72

## 2.7 Theranostics

The ultimate goal of the cancer drug discovery is to monitor drug delivery to the diseased tissue, delivery kinetics, with concurrent imaging. Theranostics are the materials that combine the modalities of therapy and diagnostic imaging such that it delivers therapeutic drugs as well as diagnostic imaging agents concurrently within same dose<sup>10</sup>. Theranostics have potential advantage of overcoming undesirable differences in biodistribution and selectivity on concurrent administration of therapeutic drugs and diagnostic agents<sup>10,83</sup>. Owing to combinatorial properties of nanoparticles such as modifiable surfaces, nanometric size for radial clearance, high surface area to volume ratios, high loading capacity, and nanoparticulate drug delivery provides the multifunctional platform. Nanoparticles either have characteristics material properties for diagnosis or diagnostic agents can be conjugated and can be used as theranostics. Theranostic strategies were developed based on nanotechnological platform for different types of cancer treatments, such as nucleic acid therapy, chemotherapy, hyperthermia treatment (Photothermal ablation), photodynamic therapy, radiation therapy with incorporation of imaging agents to promote one or more diagnostic imaging techniques, such as magnetic resonance imaging, nuclear imaging

(PET/SPECT/CT), and/or fluorescence imaging/optical imaging<sup>10,83-85</sup>. Different types of nanoparticles used as theranostics and their applications are listed in **Table 4**.

**Table 4: Different theranostics agents used for biomedical applications** (Table Adopted from Ahmed *et al* 2012)

Nanoparticles	Therapeutic application	Diagnostic application
Manganese oxide nanoparticles	siRNAs	MRI
Gold nanoparticles	Doxorubicin	Photothermal Therapy
Iron oxide nanoparticles	siRNAs, Doxorubicin, Docetaxel	MRI, Photothermal ablation, Photodynamic therapy, cell sorting and tracking, multimodal therapy
Silica nanoparticles	Pyropheophorbide (HPPH), Doxorubicin	X-ray/CT imaging, Photodynamic therapy
Carbon nanotubes	DNA plasmid, Doxorubicin, Paclitaxel	Near infrared (NIR) Photothermal ablation therapy
Quantum dots	Doxorubicin, Methotrexate	Imaging, sensing and fluorescence imaging, FRET

Due to increased knowledge of nanotechnology, it has become possible to fabricate, characterize and modify the functional properties of nanoparticles for biomedical applications and diagnostics. As intermediates between the molecular and the solid states, inorganic nanoparticles combine chemical convenience in solution with physical properties of the bulk phase providing ideal properties for the construction of nanostructure materials and devices with adjustable physical and chemical properties<sup>86,87</sup>. Owing to multifunctional platforms, one can load a wide range of functionalities onto the particle surfaces. These nanoplatforms can be further loaded with therapeutic agents and imaging motifs to aid as multimodal imaging or for theranostics applications<sup>83,88</sup>.

## 2.8 Iron oxide nanoparticles

Colloidal iron oxide nanoparticles have been used in the clinic as MRI contrast agents, mostly for improving the visibility of lesions. Recent discovery to prepare nanoparticles with fine control over a wide range of parameters, including size, shape, composition, magnetization, surface coating and surface charge improved the applicability of nanoparticles<sup>88</sup>. Increased investigations with several types of iron oxides have been carried out in the field of nanosized magnetic particles (mostly maghemite,  $\gamma$ -Fe<sub>2</sub>O<sub>3</sub>, or magnetite, Fe<sub>3</sub>O<sub>4</sub>). Magnetite, Fe<sub>3</sub>O<sub>4</sub>, is a common magnetic iron oxide that has a cubic inverse spinel structure. It exhibits unique electric and magnetic properties based on transfer of electrons between Fe<sup>2+</sup> and Fe<sup>3+</sup> ions in octahedral sites<sup>89</sup>. Due to their ultra-fine sizes, biocompatibility and superparamagnetic properties, magnetite nanoparticles are emerging as promising candidates for drug delivery and biomedical imaging applications<sup>90</sup>. These nanoparticles are occurred with two major obstacles for *in vivo* applications: short plasma half-life and thus reduced efficiency. Their destabilization and aggregation due to plasma protein absorption

and non-specific uptake by reticular-endothelial system (RES), i.e. macrophages, lead to reduced plasma concentration and efficiency. With proper hydrophilic and biocompatible surface coating; these nanoparticles can be stabilized, and RES clearance avoided to be efficacious. Dispersed into suitable solvents forming homogeneous suspensions, called Ferrofluids. Such a suspension can interact with an external magnetic field and be positioned to a specific area, facilitating magnetic resonance imaging (MRI) for medical diagnosis and AC magnetic field-assisted cancer therapy<sup>89</sup>. All these technological and medical applications require superparamagnetic magnetite nanoparticles with sizes smaller than 20 nm and the overall particle size distribution is narrow so that the particles have uniform physical and chemical properties. These nanoparticles are commonly known as 'Superparamagnetic iron oxide nanoparticles' (SPIONs). SPIONs typically consist of two components, an iron oxide core and a hydrophilic coating such as Dextran, Dextrimers, Polyethylene glycol or Polyethylene oxide<sup>11</sup>. SPIONs can be categorized based on their overall diameter and are listed in **Table 5**.

**Table 5: Different categories of SPIONs** (Table adopted and modified from Thorek *et al* 2006)

Categories	Abbreviation	Mean Particle size	Trade names
oral SPIONs	oral SPIONs	300 nm-3.5 $\mu$ m	Lumirem, Gastromark, Ferumoxsil, Abdoscan
Standard SPIONs	SSPIONs	60 -150 nm	Feridex, Endorem, Ferumoxide, Resovist
ultrasmall SPIONs	USPIONs	10 - 40 nm	Sinerem, Combidex, Ferumoxtran, Clariscan
Monocrystalline SPIONs	MIONs	10- 30 nm	--
Cross-linked dextran SPIONs	CLIONs	10 - 30 nm	--

As mentioned earlier, SPIONs synthesized in presence of coating polymers, usually dextran, due to their biocompatibility, biodegradable, less prone to anaphylactic shock and show longer plasma half-life<sup>11,91</sup>. These hybrid inorganic-organic nanocomposite SPIONs are of potential use because of their multifunctionality, ease of processability and simplicity of large scale manufacturing<sup>92</sup>.

### 2.8.1 Characteristics SPIONs

The magnetic properties of ferromagnetic iron oxide nanoparticles are results of aligned unpaired electron spins. These materials exhibit magnetization even in absence of external magnetic field. In a non-magnetized ferromagnetic material, magnetic domains (Weiss domains) at short range are aligned but at long range adjacent domains are anti-aligned. This transition between two domains is called Bloch wall. At the nanometer scale (~14 nm),

the formation of Bloch walls becomes thermodynamically unfavorable leading to formation of signal domain crystals, termed as superparamagnetic. It is characteristic of aligning atomic magnetic dipoles with applied external field, their positive magnetic susceptibility and random orientation in absence of magnetic field (Brownian Fluctuation). SPIONs exhibit larger magnetic susceptibility as entire crystal aligns with the applied field due to its single crystal structure. On application of external magnetic field, SPIONs magnetic moments align in direction of magnetic field, enhancing magnetic flux. This ability to elicit substantial disturbances in the local magnetic field through large magnetic moments leads to rapid dephasing the surrounding protons, detecting significant changes in MR contrast signal. Thus imaging capability provided is not intrinsic property of SPIONs, but through their influence on longitudinal ( $r_1$ , Spin-lattice) and transverse ( $r_2$ , spin-spin) relaxation of the surrounding nuclei. Although the ability of SPIONs to significantly reduce the spin-spin relaxation ( $T_2$ ) time is generally relied on for generating MR contrast, it has also been demonstrated that SPIONs can generate sufficient  $T_1$  contrast for biomedical applications; thus possessing both high  $R_1$  and  $R_2$  relaxivities<sup>11,86,87,93</sup>.

Besides the magnetic properties, the colloidal properties are of high importance. Upon removal of the magnetic field, Brownian motion is sufficient to randomize the SPIONs orientations leaving no magnetic reminiscences. Brownian forces also prevent the aggregation of the SPIONs due to magnetic attraction in solution. The attractive *van der Waals forces* and repulsive forces, like *electrostatic or steric hindrance*, depends strongly on the ionic strengths, pH and type and conformation of surface coatings and biological molecules. In cell media and similar liquids with high ionic strength the electrostatic double layer is very small, thus, steric stabilization imparts stability to SPIONs<sup>91</sup>. The multifunctionality of SPIONs further enables the integration of imaging and therapy (Theranostics). SPIONs have received great attention in the development of theranostic nanomedicines because they are not only used as contrast enhancement agents for MRI but can also deliver therapeutic agents, such as anticancer drugs to disease sites. In addition, SPION can be used for Magnetic induced hyperthermia, photodynamic therapy (PDT), and photothermal ablation owing to continuous emission of heat by converting electromagnetic energy into heat upon exposure to an alternating external magnetic field (AMF)<sup>91</sup>. Choosing high power SPIONs combined with appropriate external magnetic field, very small amounts of particles can be used to raise the temperature of biological tissue locally up to cell necrosis. It was shown that hyperthermia greatly enhances cytotoxicity of radiation and drug treatment with brain tumor cell lines, which were also confirmed by multimodal hyperthermia<sup>87</sup>.

## 2.9 Ligand targeted therapy

Owing to surface modification characteristics and multifunctionality of nanocarriers, one strategy is to couple the nanocarriers to antibodies or other ligands that recognize tumor-

associated antigens to improve exposure to the tumor cells, to increase efficacy and reduce nonspecific side effects. The choice of targeting ligand can be crucial to the success of targeting applications. Variables that must be considered include the degree of receptor expression; degree of internalization and surface expression<sup>94</sup>. Mucin 1 (MUC1) is associated with tumor invasion and is highly expressed in pancreatic ductal adenocarcinoma<sup>95</sup>. Targeting of variants of MUC1 in solid tumors as ligand targeted therapy may prove beneficial for site directed tumor selective therapy<sup>96</sup>.

### **2.9.1 MUC1**

MUC1 is a highly O-glycosylated transmembrane protein predominantly expressed on apical surface of glandular epithelial cells. It lubricates and protects the outer border against extracellular events. MUC1 is distributed on cell surface as well as in cytoplasm. In Normal tissues, MUC1 is highly glycosylated. Neoplastic cells showed underglycosylated MUC1 (uMUC1) owing to premature termination of carbohydrate chain by addition of sialic acid, limiting its branching potential. These molecule extends 100-200 nm above the surface, making MUC1 an accessible target for imaging and, possibly, therapeutic probes. During tumorigenesis, uMUC1 is no longer restricted to the apical surface of plasma membranes and covers the entire cell surface, leading to interactions of cytoplasmic tails with signaling molecules. Owing to its surface properties, uMUC1 expression remains homogenously upregulated and ubiquitous during progression of tumor. Such abnormal expression has been associated with cellular growth, transformation, adhesion, invasion and immune cell responsiveness and tolerance<sup>97-100</sup>.

Multiple monoclonal antibodies targeted against uMUC1 have been studied to recognize immunogenic APDTRP sequence of tandem repeats. Consequently, small non-immunogenic, high affinity with selectivity peptides derived from CDR3 V<sub>h</sub> region of anti-ASM2 antibodies, named EPPT, has been studied<sup>97-101</sup>. Taken together uMUC1 provides a promising target for site directed ligand specific therapy of PDAC.

### **2.9.2 MPAP**

Most oligonucleotides, peptides or proteins are taken up by cells due to their insufficient association with lipid bilayer of the plasma membrane. Therapeutic agents need to possess lipophilic properties in order to achieve the desired pharmacokinetic profile. Thus, the lipophilicity of the molecules assists in penetration of cytoplasmic and intracellular membranes<sup>102</sup>. Recently, myristoylated poly-arginine peptides (MPAP) have been studied to increase translocation of drug delivery vectors into cytoplasm. MPAP is small peptides with a 14-carbon myristic acid moiety increases the affinity of the peptide for lipid bilayer membranes. This peptide was used to promote cellular uptake of drug delivery vectors to

solid tumors by facilitating uptake by electrostatic interaction between the positively charged peptide and the negatively charged cell membrane<sup>101,103-106</sup>.

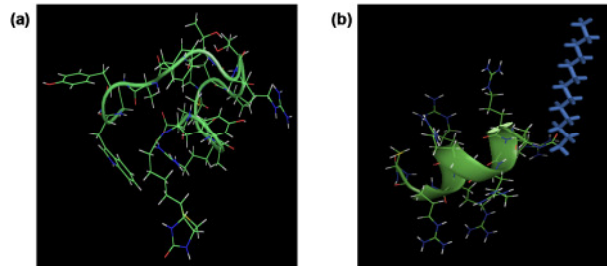


**Figure 6: Structure of uMUC1 selective peptide, EPPT1 (a) and myristoylated poly-arginine peptide, MPAP (b).**

### 2.10 Use of RNA interference in Tumor therapy

In vivo gene silencing using RNA interference (siRNA) plays an important role in target validation and is advancing towards the development of siRNA based therapeutics. The growth of siRNA technology and the potential of this phenomenon to control gene expression very precisely have opened opportunities for the management and controlling disease. Cancer is the alteration of gene expression causing uncontrolled gene expressions. The identification of this altered expression is the key for the precise targeting of these molecules using siRNA. Owing to its selectivity, better tolerability with minimal side effects, siRNA provide the basis of development of selective anti-cancer therapy in controlling cancer to a more manageable disease organ delivery via direct injection into a confined organ. For systemic use, the biggest challenge in the use of siRNA based therapies is the difficulty of delivery. In order to become effective and induce silencing, it is imperative that the siRNAs reach the cytoplasm of the target cell. Naked siRNA cannot penetrate cellular lipid membranes and therefore, systemic application of unmodified siRNA, due to its susceptibility to degradation by RNase, is unlikely to be successful. To address the concerns of low stability in serum and rapid renal excretion, several different approaches have been developed to deliver envelope packaged siRNA. The most popular envelopes included liposomes and other nanoparticles, both as simple packages, but also in combination with specific ligand targeted molecules designed to direct the preferential uptake by a specific target tissues<sup>76-78,107</sup>. Though siRNA therapy poses promising strategy for anti-cancer therapy, there is need for development for high specificity, limited side effects and potential for targeting a multitude of therapeutic targets.

### 3. HYPOTHESIS

Keeping the limitations of classical PDAC therapy and *In vivo* delivery of siRNA in mind, we hypothesize to develop a novel formulation that not only delivers the siRNAs adequately and specifically to the tumor site but also allows non-invasive imaging of the uptake of therapeutic agent. In order to accomplish this, we will design dual purpose functional probes comprising of dextran coated superparamagnetic nanoparticles as a delivery platform which can be detected by magnetic resonance imaging (MRI) and which will be further conjugated with streptavidin. Biotinylated MPAPs, for translocation of the complex into the cytosol by electrostatic interaction and biotinylated EPPT1, a non-immunogenic underglycosylated MUC1 peptide highly specific for MUC1 protein, for tumor specific intake will be further conjugated to delivery platform considering the fact that streptavidin-biotin as one of the strong covalent interaction. In addition, we will couple siRNA targeted against PLK1 to these nanoparticles Administration of these PLK1 targeting complex in tumor-bearing mice will allow monitoring of delivery to the tumor and metastasis by MRI imaging and should result in efficient silencing of the target genes.

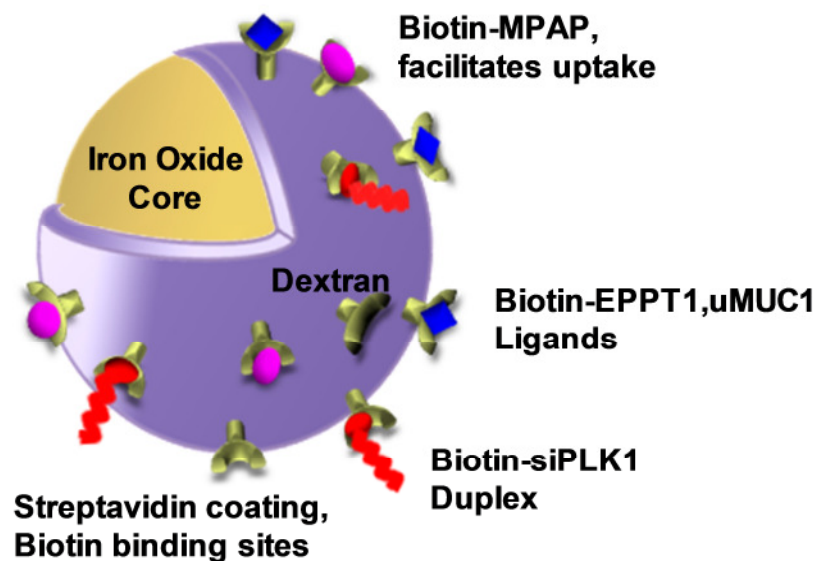


**Figure 7: schematic representation of siPLK1 coupled streptavidin conjugated dextran coated superparamagnetic iron oxide nanoparticles (siPLK1-StAv-SPIONs) conjugated to the membrane translocation peptide(MPAP), the underglycosylated MUC1 specific peptide (EPPT1) and siRNA molecules targeting PLK1 (siPLK1)**

## 4. MATERIALS AND METHODS

### 4.1 Materials

#### 4.1.1 Antibodies and growth factors

Anti-Biotin (PE Conjugated)	Biologend
Anti-CD11c (BV 605 Conjugated)	Biologend
anti-CD19 BV 421 Conjugated)	Biologend
Anti-CD3 (PerCP-Cy5.5 Conjugated)	Biologend
Anti-CD31	Dianova
Anti-EEA1	Cell signaling
Anti-F4/80 (PE Conjugated)	Biologend
Anti-GAPDH	Meridian
Anti-Gr1 (FITC Conjugated)	Biologend
Anti-Ki-67	Bethyl
Anti-Mouse-Alexaflour 488	Invitrogen
Anti-MUC1	Cell signaling
Anti-MUC1 (MH1)	Abcam
Anti-PCNA	Cell signaling
Anti-PLK1	Thermo scientific
Anti-streptavidin (FITC Conjugated)	Acris
Envision+system HRP labeled anti-Mouse IgG	Dako
Envision+system HRP labeled anti-Rabbit IgG	Dako
FITC-Conjugated anti-Mouse IgG	Jackson Laboratories
FITC-Conjugated anti-Rabbit IgG	Jackson Laboratories

#### 4.1.2 Enzymes, kits and substrates

3, 3'-diaminobenzadine (DAB) staining kit	Vector Laboratories
Accustain Iron staining kit	Sigma-Aldrich
Amexa cell line nucleofactor kit V	Lonza
CBA Kit	BD biosciences

ECL Reagent	Thermo scientific
In-situ cell detection kit, TMR red	Roche
Qiagen Mini RNA extraction kit	Qiagen
Quantitect reverse transcription kit	Qiagen
Ribogreen RNA quantification kit	Molecular Probes
Z-DEVD-R110	Invitrogen

#### **4.1.3 Peptides and siRNAs**

{Myr}ARRRRRRC-{Biotin-Lys}	Genscript
C{AHA}Y{Cys(ACM)}AREPPTRTFAYWG-{Biotin}	Genscript
Biotin-PEG-Cy5	Nanoc Inc.
Biotin-BSA	Thermo scientific
PLK1 siRNAs	Dharmacon

Sense: GCCUGAUUCUCUACAAUGAdGdT

Antisense: {Bi}-CAUUGUAGAGAAUCAGGCdGdT

Mismatch control	Dharmacon
------------------	-----------

Sense: UUCUCCGAAGCUGUCACGUdGdT

Antisense: {Bi}-ACGUGACACGUUCGGAGAAAdGdT

#### **4.1.4 Chemicals**

2'7' dichloroflourescein diacetate (DCFDA)	Sigma-Aldrich
5 Flourouracil	Activis
Acetone	J.T. Baker
Agarose	Roth
Ammonium acetate	Sigma-Aldrich
Ammonium chloride	Sigma-Aldrich
Ammonium Hydroxide	Sigma-Aldrich
Aprotinin	Sigma-Aldrich
APS	Sigma-Aldrich
Ascorbic acid	Sigma-Aldrich

Aurion BSA	Aurion
BI6727	Bohringer Ingelheim
Blotting Paper (Nitrocellulose)	GE Healthcare
Boranmethylamine	Sigma-Aldrich
BSA	GE Healthcare
Bradford reagent	Sigma-Aldrich
Bromophenol blue	Fluka
Calcium Chloride	Sigma-Alrich
DAPI	Fluka
Dextran T10	Pharmacosmos
Diethyl ether	Roth
DMSO	Roth
Dynasore	Sigma-Aldrich
EDTA	Sigma-Aldrich
Eosin	Sigma-Aldrich
Ethanol	J.T. Baker
Ethanolamine hydrochloride	Sigma-Aldrich
Ferric Chloride	Sigma-Aldrich
Ferrous Chloride	Sigma-Aldrich
Ferrozine	Sigma
Fluorescent mounting Media	Dako
Formaldehyde	Polyscience
Gemcitabine	Eli Lilly
Gluteraldehyde	Sigma-Aldrich
Glycerol	Merck
Glycidether	Raschig GmbH
Haematoxylin	Sigma-Aldrich
HEPES	Sigma-Aldrich

Hydrochloric acid	Merck
Hydrogen peroxide	Merck
Iron solution standard	Calbiochem
Ketamine	Selectavect
Leupeptin	Sigma-Aldrich
Magnesium chloride	Sigma-Aldrich
MDC	Sigma-Aldrich
Methanol	Roth
Millipore water	<i>In-house</i>
Neocuproine	Sigma-Aldrich
Nocodazole	Sigma-Aldrich
Oregon Green 488	Invitrogen
Osmium tetroxide	Sigma-Aldrich
Paraformaldehyde	Sigma-Aldrich
Pen-Strep	Gibco
PMSF	Sigma-Aldrich
Polyacrylamide	Roth
Potassium bicarbonate	Merck
Potassium chloride	Merck
Potassium dihydrogen phosphate	Merck
Potassium hydroxide	Merck
Potassium permanganate	Sigma Aldrich
Potassium phosphate	Merck
Propidium iodide	Sigma-Aldrich
RNAse free Water	Ambion
Saponin	Sigma-Aldrich
Sodium chloride	Roth
Sodium dodecyl sulphate	Sigma-Aldrich

Sodium dihydrogen phosphate	Merck
Sodium fluoride	Sigma-Aldrich
Sodium fumarate	Sigma-Aldrich
Sodium glutamate	Sigma-Aldrich
Sodium periodate	Sigma-Aldrich
Sodium Pyrophosphate	Sigma-Aldrich
Sodium pyruvate	Sigma-Aldrich
Streptavidin	iBA
SYBRGreen PCR master mix	Applied systems
TEMED	Roth
Tris	Roth
Triton-X100	Sigma-Aldrich
Tween 20	Sigma-Aldrich
Vectastain Mounting Media	Vector Laboratories
Xylazine	Selectavect
Xylol	J.T. Baker
$\beta$ -mercaptoethanol	Sigma-Aldrich

#### **4.1.5 Glasswares and labwares**

0.22 $\mu$ m Syringe filters	Roth
0.45 $\mu$ m Syringe filters	Roth
0.5ml Eppendorf tubes	Sarstedt
1.5ml Eppendorf tubes	Sarstedt
2ml Eppendorf tubes	Sarstedt
15ml centrifuge tubes	Sarstedt
1ml syringes	BD
24 wells cell-culture plates	Falcon
50ml centrifuge tubes	Falcon
6 wells cell-culture plates	Falcon

8 chamber microscopy slides	Grainer
96 wells cell-culture plates	Falcon
96 wells round bottom plates	Grainer
Cell culture accessories	Sarstedt
Cell strainer 70µm	BD
Cotton gauze	Fuhrmann
FACS tubes	Sarstedt
Glass coverslips	R. Langerbrink
Glass slides	Thermo scientific
Glass slides	R. Langerbrink
Haemocytometer	Roth
Heparinized capillaries	BRAND
Hybond-ECL nitrocellulose membranes	GE Healthcare
MACS LS Columns	Miltenyi Biotech
Microscopy plates, µ-dish, 35 mm	Ibidi
Needles (20-31G)	BD
PD10 Columns	GE Healthcares
Pipette tips	Sarstedt
Polystyrene membrane inserts	Costar
Round bottom flask	Roth
Silicon tips	Veeco Probes
Sterilized 10 ml conical flasks	Roth
Tissue-tek OCT	Tissue Tek
Vaccustainer	BD
Zeta-potential measurement cuvette	
Zetasizer cuvette	
<b>4.1.6 Cell-culture media and Buffers</b>	
Dako antigen retrieval buffer	Dako

DMEM with GlutaMax+		Gibco
Erythrocyte lysis Buffer		<i>In-house</i>
Ammonium chloride	155mM	
Potassium bicarbonate	10mM	
EDTA	0.1mM	
FACS Buffer		<i>In-house</i>
FCS	2%	
EDTA	1mM	
Sodium azide	0.1%	
PBS		
FACS cell permeabilisation buffer		Miltenyi Biotech
Faetal calf serum		Pan Biotech
Immunofluorescence Buffer, pH 7.4		<i>In-house</i>
BSA	0.2%	
Saponin	0.05%	
Sodium azide	0.1%	
Triton-X-100	0.01%	
PBS		
Laemilli Buffer (4X), pH6.8		<i>In-house</i>
Tris-HCl pH6.8	0.125M	
SDS	2%	
Glycerol	10%	
β-mercaptoethanol	0.5ml	
Commassie Blue	0.5%	
water	to 10ml	
Pen-Strep antibiotic solution		<i>In-house</i>
Phosphate Buffer Saline (PBS), pH 7.4		<i>In-house</i>
NaCl	8g	

KCl	0.2g	
Na <sub>2</sub> HPO <sub>4</sub>	0.24g	
KH <sub>2</sub> PO <sub>4</sub>	0.24g	
Distilled water	1000ml	
Phosphate Buffer, 10mM, pH 7.4		<i>In-house</i>
Na <sub>2</sub> HPO <sub>4</sub>	0.207%	
NaH <sub>2</sub> PO <sub>4</sub>	0.031%	
Phosphate Citrate Buffer, 50mM, pH 5.0		<i>In-house</i>
Na <sub>2</sub> HPO <sub>4</sub>	0.1M	
Sodium citrate	0.05M	
Ponceau S staining solution		<i>In-house</i>
Ponceau S	0.5%	
Acetic acid	3%	
RPMI with Glutamax+		Gibco
Stripping Buffer, pH 3.0		<i>In-house</i>
Glycine	15g	
SDS	1g	
Tween 20	10ml	
Distilled water	to 1000ml	
Towbin Transfer Buffer, pH 6.8		<i>In-house</i>
Tris	25mM	
Glycine	192mM	
SDS	0.1%	
Methanol	20%	
Tris Buffer Saline- Tween 20 (10X), pH 7.2		<i>In-house</i>
Tris-HCl, pH 6.8, 1M	100mM	
Sodium Chloride	1.5M	
Tween 20	0.5%	

Tris-Borate-EDTA Buffer (10X) pH 8.3	<i>In-house</i>
Tris-base	450mM
EDTA	10mM
Boric acid	27.5g
Distilled water	1000ml
Tris-Glycine-SDS Buffer (10X)	<i>In-house</i>
Tris-base	250mM
Glycine	1.92M
SDS	1%
Trypsin/EDTA solution	Gibco

#### **4.1.7 Instruments**

7 Tesla small animals MRI	Bruker
7500 real time PCR system	Applied systems
Atomic absorbance spectrometer	Contra700
Atomic force microscope	Leica
BD LSR II system	BD
Cell-culture Incubators	Binder
Centrifuges	Eppendorf
Cool-centrifuge	Eppendorf
Cryo-microtome	Leica
ELISA plate reader (Photometer)	Molecular Devices
Fine weighing balance	Sartorius
FluorStar Optima flourometer	Optima
Heating blocks	QBT
Inverted microscope	Zeiss
Leica Fluorescence microscope	Leica
MACS Magnetic separator	Miltenyi Biotech
Microtome	Leica

Millipore water cartridge	Millipore
Motorized Stirrer	MLW
Olympus FLUOVIEW FV1000 microscope	Olympus
pH Meter	Knick
PowerPac	Biorad
Qiagen Tissue lyser	Qiagen
Rotating shaker	Uniequip
Scanning electron microscope with EDX detectors	
SDS-PAGE apparatus	PeqLab
Semi-dry blotting apparatus	Biorad
Sterile laminar air flow cabinets	Thermo scientific
Sonicator, probe	Bandelin
Transmission electron microscope	Zeiss
TEM with EDX detectors	Phillips
Ultratome	Leica
Vacuum Dryer	Savent
Vibrating shaker	GrandBio
Vilber Photoimager	Vilber
Water bath	GFL and Julabo
Weighing balance	Ohaus
Zeiss microscope	Zeiss
Zetasizer	Malvern Instruments

#### **4.1.8 Cell-lines and Animals**

6606Liver cell-line	Prof. Dr. Tuveson's Lab
6606PDA cell-line	Prof. Dr. Tuveson's Lab
C57/BL6 mice	Charles River
LSL-Kras <sup>G12D</sup> , LSL-Trp53 <sup>R172H</sup> , Pdx-1-Cre mice	Prof. Dr. Tuveson's Lab
PanC02G cell-line	ATCC

**4.1.9 Software**

AidScans	Anyintelli
CellSens software	Olympus
DataAssist	Applied biosystem
FlowJo	FlowJo.LLC
Fluoview FV10-ASW	Olympus
GraphPad Prism	GraphPad Software
ImageJ	NIH
Leica MM AF 1.5	Leica
MATLAB	Mathworks
MS Office (Word, Excel, PowerPoint)	Microsoft Corporation
NanoScope 7.3	Leica
Osirix	Pixmeo
PKSolver	Open source software
PyMol	Schrodinger LLC
ScanScope	Aperio
SigmaPlot	Systat Software Inc.
SyngoFastview	Siemens
Zetasizer software	Malvern Instruments

## 4.2 Methods

### 4.2.1 siRNAs

The PLK1 siRNA duplex, directed against sense sequence: GCCUGAUUCUCUACAAUGAdGdT, and antisense: {Bi}-CAUUGUAGAGAAUCAGGCdGdT with biotin at 5 prime of the antisense strand was designed and synthesized to target *in vivo* PLK1 by Dharmacon (Thermo Scientific, MA, USA). siRNA for mismatch control with sense sequence: UUCUCCGAAGCUGUCACGUdGdT, and antisense: {Bi}-ACGUGACACGUUCGGAGAAAdGdT) was designed and synthesized analogous to siPLK1. Myristoylated poly arginine peptide, MPAP and underglycosylated non-immunogenic MUC1 specific peptide, EPPT1 peptides were designed and synthesized by Genscript Corporation, NJ, USA. All the reagents were purchased from Sigma-Aldrich unless otherwise mentioned.

### 4.2.2 siPLK1-StAv-SPIONs synthesis

Synthesis of dextran coated magnetic nanoparticles (SPIONs) was performed from the method adopted and modified from US patent 5262176<sup>108</sup>. Briefly, nitrogen purged cooled 76.2 ml solution of Dextran T10 (34.1 g) and ferric chloride (6.31g) were added to freshly prepared 8.6 ml solution of ferrous chloride (2.51g) with vigorous stirring on ice. The resultant solution was rapidly neutralized by addition of ammonium hydroxide solution (9 ml) to get green slurry. This green slurry with nitrogen purging was heated over the period of one hour in water bath gradually increasing the temperature from 75°C to 85°C and further heated for another hour at 85°C. On cooling, this magnetic slurry was purified using magnetic-activated cell sorting (MACS) LS columns followed by concentration using ultrafiltration. Concentrated SPIONs were characterized to measure hydrodynamic diameter, iron content and zeta potential.

Aliquots of SPIONs were suspended in phosphate citrate buffer (50mM, pH 5.0) and allowed to react with 1 mg/mg sodium periodate equivalent to iron at 4°C overnight. The resultant solution was diluted with phosphate buffer (10 mM, pH 7.4) and excess of sodium periodate was washed in PD10 desalting columns equilibrated with phosphate buffer 10mM pH 7.4. These columns were eluted with phosphate buffer 10 mM pH 7.4 in a tube containing 2 mg streptavidin (iBA GmbH). Streptavidin conjugated solution was incubated at 4 °C overnight with gentle shaking. Conjugation reaction was stopped by addition of 140 mM borandimethylamine and incubated at 4°C for 6-8 hours. The excess of aldehyde formed during reaction was neutralized using 0.5M ethanolamine at 4°C overnight. The resultant particles (StAv-SPIONs) were purified in magnetic-activated cell sorting (MACS) LS columns and resuspended in ultrapure nuclease free water.

The StAv-SPIONs were conjugated with 10 $\mu$ M biotinylated siRNA duplex with biotin coupled to 5' end of antisense strand at 4 $^{\circ}$ C for 1 hour. Further, 10 $\mu$ g/ $\mu$ l of MPAP peptide [{{Myr}ARRRRRRC-{{Bi-Lys}}] and 10 $\mu$ g/ $\mu$ l of underglycosylated nonimmunogenic peptide, EPPT1 [C{{AHA}Y{{Cys(ACM)}}AREPPTRTFAYWG-{{Bi}}] were conjugated with StAv-SPIONs at 4 $^{\circ}$ C for 1 hour to get siPLK1-StAv-SPIONs. siPLK1-StAv-SPIONs were purified to remove unconjugated siRNA duplex and peptide ligands using magnetic-activated cell sorting (MACS) LS columns and resuspended in ultrapure nuclease free water.

#### **4.2.3 Characterization of SPIONs**

The shape, size, composition and lattice structure of the siPLK1-StAv-SPIONs were investigated with a transmission electron microscope (TEM) with a FEI Tecnai G220 S-Twin TEM and PhilipsCM200/FEG high-resolution TEM (HRTEM) operated at 200 kV which was equipped with an energy dispersive X-ray detector (EDX). The TEM grids were prepared for imaging by placing a small drop of the specimen solution on a copper grid having an amorphous carbon film less than 20 nm thick and allowing it to dry completely in air at ambient temperature.

To characterize the structural features of the nanoparticles in air, AFM imaging was performed using a BioScope II scanning probe microscope. Nanoparticle solutions were placed on freshly cleaved mica, glued to a glass slide. After 10 seconds of incubation, samples were washed with ultrapure water and imaged in tapping mode at room temperature, using a silicon tip (Drive frequency of 320 kHz, radius 8 nm, TESP). Images (10 x 10  $\mu$ m<sup>2</sup>) were analyzed using NanoScope 7.3 software. In house script in MATLAB was used to analyze the height distribution of the features imaged with AFM tapping mode as previously described<sup>109</sup>. Briefly, the script scans over the images looking for the highest point within a moving 17x17 points rectangle. To avoid crosstalk with measurement noise, a 0.9 nm threshold was used in this study. The grains found in this process were saved with their position and height. The height values were then merged and plotted into frequency distributions.

The hydrodynamic diameter and effective surface charges ( $\zeta$ -potential) of siPLK1-StAv-SPIONs were measured with samples thermostated at 25 $^{\circ}$ C using Malvern Instruments Zetasizer.

To evaluate binding efficiency of streptavidin, StAv-SPIONs were treated with biotinylated BSA (range: 100ng to 500ng) and change in hydrodynamic diameter was measured over a period of 1 hour with samples thermostated at 25 $^{\circ}$ C using Malvern Instruments Zetasizer.

The quantification of siRNA binding was performed using 2% agarose gel electrophoresis using Tris-borate-EDTA buffer after pretreatment of the nanoparticles solutions with 1% SDS

with 5 min boiling to release siRNA duplex from siPLK1-StAv-SPIONs. The band thus obtained was quantified using ImageJ software. For quantification of bound siRNA in nanoparticle solution, Ribogreen RNA quantification kit was used as prescribed in manufacturer's instruction.

Predicted protein structures of streptavidin for PyMOL analysis were retrieved from the protein data bank and were used for molecular docking with biotinylated siRNA duplex in their 3D conformation using PyMOL software.

#### **4.2.4 Animal strains**

All animals studies were approved by local institutional animal care committee of the Ernst-Moritz-Arndt University, Greifswald and complied with the NIH guidelines on handling of experimental animals. C57BL/6N mice were purchased from Charles-River Inc. and housed under standard conditions and after one week of acclimatization, 6606PDA cells were implanted in animals by syngenic orthotopic injection in head of the pancreas<sup>110,111</sup>. 14 days after tumor implantation animals were randomized to three groups to receive 3qD intravenous injections (i.v.) of siPLK1 (100nM/kg), siControl-StAv-SPIONs (5 mg/kg of iron) or siPLK1-StAv-SPIONs (5 mg/kg of iron) respectively. The treatment schedule was maintained for 4 weeks and on completion of treatment, animals were euthanized to evaluate the influence of treatment regimen.

The LSL-Kras<sup>G12D</sup>, LSL-Trp53<sup>R172H</sup>, Pdx-1-Cre (KPC) strains of mice have been generated as previously described<sup>30,112</sup>. 16-20 weeks old mice were randomized to three groups. Animals were treated by randomized double blind study for 2 weeks to receive 3qD intravenous injections (i.v.) of siPLK1 (100nM/kg), siControl-StAv-SPIONs (5 mg/kg of iron) or siPLK1-StAv-SPIONs (5 mg/kg of iron) respectively. Tumor growth were monitored by ultrasound imaging as explained previously<sup>113</sup>.

Stably transfected pancreatic ductal adenocarcinoma cells, 6606PDA were maintained in culture as described previously<sup>110</sup>.

#### **4.2.5 Measurement of iron content**

Quantitative determination of siPLK1-StAv-SPIONs probes uptake were performed after 2 and 4 hours of incubation with 50µM siPLK1-StAv-SPIONs followed by extraction and measurement of iron calorimetrically as described previously<sup>114</sup>. Briefly, aliquots of cell lysates were mixed with 10mM HCl and iron releasing reagent (a freshly mixed solution of equal volumes of 1.4M HCl and 4.5%w/v KMnO<sub>4</sub>). On 2 hours at 60°C incubation of this mixture, iron detection reagent (6.5mM ferrozine, 6.5mM neocuproine, 2.5M ammonium acetate, and 1M ascorbic acid) was added and after 30 minutes, absorbance was measured at 550nm. The iron content of the sample was calculated by comparing its absorbance to that

of a range of standard iron concentrations. The intracellular iron concentration determined for each well of a cell culture was normalized against the protein content.

#### **4.2.6 Cell cycle analysis**

For cell cycle analysis, cells were treated for 18 hours with siControl-StAv-SPIONs, 5FU (10 $\mu$ M), gemcitabine (Actavis, 10 $\mu$ M), nocodazole (30 $\mu$ M), BI6727 (30nM) and siPLK1-StAv-SPIONs. siControl and siPLK1 transfection were served as a mismatch control and transfection efficiency control. Cell cycle analysis was performed as described previously<sup>115</sup>. Briefly, about 1 $\times$ 10<sup>6</sup> cells were trypsinized, washed twice with PBS, and fixed in 70% ice-cold ethanol. Cell pellet was resuspended in 1ml of propidium iodide (PI) staining solution I and incubated for 30 min at room temperature. Cell-cycle distributions were determined using BD LSR II system. The fluorescence signal was detected through the FL2 channel and the percentage of cells in G<sub>0</sub>/G<sub>1</sub>, S or G<sub>2</sub>/M phase was analyzed by FlowJo.

#### **4.2.7 Proliferation assay**

To assess the influence on proliferation, 6606PDA cells were treated with different subsets of treatment regimens and cell proliferation ELISA. BrdU (colorimetric) were performed as per manufacturer's instruction at 0, 6, 18, 24, 36 and 48 hours. siPLK1 transfection by means of electroporation using Amexa cell line nucleofactor kit V served as control for transfection efficiency.

#### **4.2.8 In solution stability of siPLK1-StAv-SPIONs**

To determine the in solution stability, we incubated siPLK1-StAv-SPIONs in nuclease free saline at 37<sup>o</sup>C for duration ranging from 0 to 14 days and checked for siPLK1 efficiency using FACS cell cycle analysis. Cell cycle analysis was performed as described<sup>115</sup>. Percent of the cells in G<sub>2</sub>/M phase of cell cycle were analyzed as efficiency parameter.

#### **4.2.9 In vitro toxicity**

To determine generation of reactive oxidative species (ROS), approx. 1  $\times$  10<sup>6</sup> cells were incubated with siPLK1-StAv-SPIONs for 2 and 4 hours followed by 1 hour of 50 $\mu$ M of cell permeable dye 2',7'-dichlorofluorescein diacetate (DCF-DA) which convert to fluorescent 2',7'-dichlorofluorescein, when oxidized by ROS. Cells were repeatedly washed with PBS and cell lysates were prepared. The fluorescence of cell lysates thus obtained, were measured in FluorStar Optima fluorometer (and corrected to the protein content of the lysates).

#### **4.2.10 Live cell imaging and uptake measurement**

For fluorescent live cell imaging siPLK1-StAv-SPIONs were further conjugated with biotinylated Cy5. Cells were treated with 50 $\mu$ M of siPLK1-StAv-SPIONs with and without EPPT-1 and MPAP and live cell confocal laser scanning microscopy was carried out for 30

min at 37°C under controlled atmosphere with 5% carbon dioxide supply and heated chambers. On Olympus FLUOVIEW FV1000 microscope. Cells were preincubated with DAPI for 30 min, which was used for nuclear counterstain. Image processing and analysis were performed with CellSens software.

#### **4.2.11 Fluorescence Immunostaining**

Cells were treated either with anti-MUC1 antibody (concentration range 0.5µg/ml to 2µg/ml), Dynasore (concentration range 10-50µM) or MDC (concentration range 10-50µM) 30 minutes prior to biotinylated Cy5 coupled siPLK1-StAv-SPIONs. After treatment regimen, cells fixed with 4% paraformaldehyde in PBS at 4°C for 30 minutes. Fixed cells were permeabilized using 0.01% Triton-X100 for 5 minutes and washed with immunofluorescence buffer, incubated 5 minutes with DAPI and Oregon Green 488 to counterstain nuclei and plasma membrane respectively. Immunostaining of MUC1 antibody was performed with anti-rabbit-Alexa flour 488 as secondary antibody. Images were captured on Olympus FLUOVIEW FV1000 microscope and images were processed on CellSens software. For quantification of Cy5 approximately 100 random cells were selected to calculate mean fluorescent intensity of Cy5. Region of interest were selected according to the plasma membrane staining.

For colocalization analysis of Cy5 coupled-siPLK1-StAv-SPIONs with endosomal marker EEA1, 6606PDA cells were incubated with Cy5 coupled-siPLK1-StAv-SPIONs for period ranging from 0 to 30 min and slides were fixed using 4% paraformaldehyde in PBS at 4°C for 30 minutes. Fixed cells were permeabilized using 0.01% Triton-X100 for 5 minutes and incubated 1 hour with immunofluorescence buffer (0.2%BSA, 0.05%Saponin, 0.01%Triton-X100 in PBS and incubated with anti-Rabbit EEA1 (Cell signaling) overnight at 4°C. Slides were washed three times with immunofluorescence buffer and incubated with FITC coupled anti rabbit secondary antibody for 1 hour at room temperature. Slides were washed again three times with immunofluorescence buffer. Slides were counterstained with DAPI and fixed with fluorescence mounting media. Images were captured on Olympus FLUOVIEW FV1000 microscope and processed on CellSens software. Quantification of colocalization was performed using colocalization plugin of ImageJ software using stacked sections for each time point.

#### **4.2.12 Transmission electron microscopy**

For transmission electron microscopy, For transmission electron microscopy, cells were grown on polycarbonate mesh and at 0 min, 5 min and 30 min treatment with siPLK1-StAv-SPIONs, the membrane was immersed in iced 2% gluteraldehyde/ 2% formaldehyde solution at pH 7.4 with 0.1 M cacodylate buffer. Blocks were post-fixed in 1% osmium tetroxide and embedded in Glycidether 100 (formerly called Epon 812), cut with diamond knives with a Leica ultratome to 500 and 750 nm thick semi-thin slides and stained according to

Richardson<sup>116</sup>. Ultrathin sections of 70-90 nm were stained with uranyl acetate and lead citrate and examined with a Libra 120 electron microscope from Carl Zeiss (Jena, Germany).

#### **4.2.13 Flow cytometric analysis**

To analyze uptake of siPLK1-StAv-SPIONs in 6606PDA cells,  $1 \times 10^6$  cells were treated for 30 minutes with different subsets of biotinylated Cy5 conjugated nanoparticles with or without peptide ligands such as MPAP(-)EPPT1(-)siPLK1-StAV-SPIONs, MPAP(-)EPPT1(+)siPLK1-StAV-SPIONs, MPAP(+)EPPT1(-)siPLK1-StAV-SPIONs and MPAP(+)EPPT1(+)siPLK1-StAV-SPIONs for 30 minutes. After incubation, cells were washed, trypsinized and pellets were resuspended in 1 ml of FACS buffer. Cells were permeabilized using permeabilisation buffer (Miltenyi Biotech, USA) for 30 minutes as per manufacturer's instructions.

To analyze uptake mechanism, cells were treated with MUC1 antibody (concentration range 0.5-2 $\mu$ g/ml) and in another set with Dynasore (concentration range 10-100 $\mu$ M) 30 minutes prior to siPLK1-StAv-SPIONs treatment and cells were processed analogous to the uptake experiments.

Cells immunolabeled with Cy5 conjugated nanoparticles were recorded using the BD LSR II system (Becton Dickinson, USA). The result was analysed using FlowJo software.

#### **4.2.14 MRI analysis**

*In vivo* 7 Tesla small animals MRI imaging was performed in tumor bearing mice before and 2 hours after injections of 5 mg/kg of iron of siPLK1-StAv-SPIONs were using Bruker, ClinScan, 7.0 Tesla, 290 mTesla/m gradient strength as described previously<sup>110</sup>. For in-situ tumor volume analysis, MRI imaging was performed at 14, 21, 28 and 40 days after tumor implantation analogous to single measurement. Generated images were analyzed employing AidScans. All image slices of the tumors were marked with regions of interest (ROI) which facilitated the calculation of the tumor volume. Quantitative determination of iron overload in tumor calculated using R2\* fat corrected single peak echos collected during MRI imaging using Osirix Diacom viewer software. The color contrast images were processed using SPIN. For checking the influence of different ligands on tumor specificity, we injected MPAP(-)EPPT1(-)siPLK1-StAV-SPIONs, MPAP(-)EPPT1(+)siPLK1-StAV-SPIONs, MPAP(+)EPPT1(-)siPLK1-StAV-SPIONs and MPAP(+)EPPT1(+)siPLK1-StAV-SPIONs 2 hours prior to MRI. Quantitative determination of iron overload in tumor calculated using R2\* fat corrected single peak echos collected during MRI imaging using Osirix Diacom viewer software.

#### **4.2.15 Iron staining in tumor section (Perl's staining)**

Mice were treated with siPLK1-StAv-SPIONs and after 6 hours of treatment, tissues were harvested, Tissues were fixed in 4% neutral buffered formalin, dehydrated and embedded in

paraffin. The deparaffinized sections were stained for iron staining using Accustain iron staining kit (Sigma-Aldrich) as per manufacturer's instructions.

#### **4.2.16 Pharmacokinetics**

The pharmacokinetic profiling of siPLK1-StAv-SPIONs was carried out after single intravenous injection in mice and harvesting serum at 0, 3, 5, 10, 30, 60, 240, 480 min by retro-orbital bleeding. These serum samples were analysed for iron using Atomic absorbance spectroscopy (contrAA 700, ASpect CS 2.0.1.0). Control mice bleeding at time equivalents were considered as blank for respective groups. The results were analyzed using PKSolver 2.0<sup>17</sup>. Non-compartmental analysis of plasma data after intravenous bolus input was considered for model approximation.

#### **4.2.17 Immunoblotting**

1 g of tumor tissue samples for immunoblotting was homogenized in precooled Qiagen tissue lyser in 250  $\mu$ l lysis buffer (25mM HEPES pH 7.5, 75mMNaCl, 0.5% Triton X-100, 5% glycerol, 1mM EDTA, 10mM NaF, 5mM Na<sub>4</sub>P<sub>2</sub>O<sub>7</sub>, 1mM PMSF and 1 mg/ml aprotinin), followed by centrifugation of lysate at 14,00rpm at 4<sup>o</sup>C for 10 minutes. Protein content of the supernatants thus obtained, were determined by Bradford Protein determination assay as per standard laboratory protocol. In all, 50  $\mu$ g samples of total protein prepared in 4x Laemalli buffer were loaded on 12.5% SDS-polyacrylamide separating gels (Tris, pH 8.8, 1M, 3.75 ml; 30% Polyacrylamide, 4.17ml; 10%SDS, 0.1 ml; 10% APS, 0.1 ml, TEMED, 0.01 ml, Water 1.88 ml) complimented with 4% stacking gel (Tris, pH 6.8, 1M, 1.25 ml; 30% Polyacrylamide, 1ml; 10%SDS, 0.1 ml; 10% APS, 0.1 ml, TEMED, 0.01 ml, Water 7.6 ml) casted in Peqlab SDS PAGE apparatus. The gels were subjected to electrophoresis at constant 20mA current in Tris-Glycine-SDS buffer. After completion of run, gels were transferred to nitrocellulose membranes for immunoblotting using semidry blotting apparatus using presoaked thick blotting pads in Towbin transfer buffer as per standard instrument program (Biorad-Minigel-StandardSD). After completion of transfer, nitrocellulose membranes were stained with Ponceau staining solution to check for transfer. Nitrocellulose membranes were blocked for 1 hour using 5% BSA in TBST for 1 hour and incubated with antibodies overnight at 4<sup>o</sup>C. Anti-PLK1 (cell signaling, 1:1000 in TBST), anti-PCNA (cell signaling, 1:1000 in TBST) were used for the immunoblotting and anti-GAPDH (Meridian, 1:1000 in TBST) was used for loading control. After washing of blots with TBST for 15 minutes at room temperature each for 3 times, blots were incubated with respective secondary antibodies (1:15000 in TBST) for 1 hour, followed by 3\*15 minutes washes of TBST. After completion of washing, blots were developed using ECL reagent and visualized in Photoimager for chemiluminescence.

#### 4.2.18 Quantitative real-time PCR analysis

Total RNA was isolated from tumors using a Qiagen Mini RNA extraction kit as per the manufacturer's instructions. After quantification, RNA quality was assessed using agarose gels. From isolated RNA, cDNA synthesis was performed using Quantitect reverse transcription kit. Real time PCR were carried out for *plk1* and *rp132* using SYBRGreen PCR master mix in 7500 real time PCR system. Gene expression was standardized using *rp132* as a candidate control. Data is expressed as fold changes with respect to control in mean  $\pm$  SD. All the primers were designed and synthesized by Invitrogen.

*plk1* Sense: TAATGACTCAACACGCCTGATT  
 Antisense: AGCTCAGCAGCTTGTCTACCAT  
*rp132* Sense: AACCCAGAGGCATTGACAAC  
 Antisense: CACCTCCAGCTCCTTGACAT

#### 4.2.19 Caspase 3 activity measurement

Tumors tissues were homogenized in PBS pH 7.0, centrifuged at 14,00rpm at 4°C for 10 min, and caspase 3 activity of the supernatant (10 $\mu$ l) was measured by fluorometric enzymatic kinetics (excitation-485nm, emission-530nm) over a period of 30 minutes at 37°C using 1 $\mu$ M of z-DEVD-R110 (90 $\mu$ l) as substrate. The caspase 3 activity of samples was a measure of change in slope per minute and was corrected by protein content.

#### 4.2.20 Histology and immunohistochemistry

For Histological evaluation of tumor, 2  $\mu$ m deparaffinized sections were incubated with Haematoxylin for 5min and followed by washing with running tap water. The sections were counterstained with Eosin (1:10 in distilled water) for 1 minute and were dehydrated as per standard lab protocol and fixed in Vectamount mounting medium. Slides were evaluated using high field magnification (20x).

For immunohistochemistry staining, the 2  $\mu$ m hydrated deparaffinized sections were incubated with 10mM antigen retrieval buffer (Dako) for 30 min in pressure cooker. The sections then treated with 0.3% H<sub>2</sub>O<sub>2</sub> for 20min and then blocked with 1% Aurion BSA for 1 hour. The section were immunolabeled using anti-Ki67,(Bethyl laboratories Inc., 1:200), anti-PLK1 (cell signaling, 1:100) and anti-CD31 (Abcam, 1:500) overnight at 4°C. The immunobound antibodies were detected using Envision+system HRP labeled polymer secondary antibodies for 1 hour and sections were developed using 3,3'-diaminobenzadine (DAB) staining using Vector peroxidase substrate kit and section were further counterstained with haematoxylin. The sections were dehydrated using standard lab protocol and fixed in VectaMount mounting medium. The number of DAB+ nuclei were analysed from 8-10 visual

fields from each sections and quantitatively analysed using NIH ImageJ analysis software. Alternatively slides were scanned using slide scanner and evaluated for staining using Aperio software.

The apoptotic cells were detected from deparaffinized sections by TUNEL assay using *in-situ* cell detection kit, TMR red (Roche Diagnostics) as per manufacturer's instruction.

#### **4.2.21 Macrophages isolation**

For macrophages isolation from bone marrow, mice were euthanized and femur and tibia were harvested in sterile condition. Femurs and tibia were flushed with 20 ml PBS using 26G syringes in 50 ml falcon tube complimented with 70  $\mu$ m cellstrainer. Isolated bone marrow cells were centrifuged at 1500 rpm for 10 min at 4°C. Cells pellets were suspended in 10 ml of PBS and cells were counted using haemocytometer. Resultant cell suspension was again centrifuged at 1500 rpm for 10 min at 4°C. The final pellet thus obtained was suspended in RPMI media with 10%FCS and 1% Pen-strep.  $1 \times 10^6$  cells/well were seeded in 6 wells plates. 6 hours after seeding, media was removed and fresh RPMI media with 10%FCS and 1% Pen-strep supplemented with 20 ng/ml M-CSF were added and this media were changed every alternate day for 7 days.

After 7 days, cells were trypsinized and seeded in 96 well plates for BrdU proliferation assay. On 60-70% confluency, cells were treated with siControl-StAv-MNPs and siPLK1-StAv-MNPs and plates were harvested for BrdU proliferation as explained in **4.2.7**.

#### **4.2.22 Splenocytes isolation**

For splenocytes isolation from spleen, spleen was harvested from euthanized animal and smashed with 10 ml PBS and filtered through 70  $\mu$ m cell-strainer. Cell suspension was centrifuged at 2800 rpm for 5 min at 4°C. The resultant pellets were suspended in 5 ml of erythrocyte lysis buffer for 5min. After addition of 10 ml of PBS in consequential suspension, it was centrifuged at 2800 rpm for 5 min at 4°C followed by resuspension of  $1 \times 10^6$  cells/ml cells in 10% DMEM media with 10% FCS and 1% Pen-Strep. After 24 hours culture in 96 well plates, cells were treated with siPLK1-StAv-MNPs for duration of 0, 5, 15 and 30 minutes and processed of cytostaining as explained in section **4.2.13**. Antibodies used for FACS were FITC conjugated F4/80 (1:1000 in FACS buffer), FITC conjugated Gr1 (1:1000 in FACS buffer), FITC conjugated CD11c (1:1000 in FACS buffer), FITC conjugated CD3 (1:1000 in FACS buffer) and FITC conjugated CD19 (1:1000 in FACS buffer). Cells immunolabeled with Cy5 conjugated nanoparticles and different cell markers were recorded using the BD LSR II system (Becton Dickinson, USA). The result was analysed using FlowJo software.

#### **4.2.23 Electrophoretic mobility**

In order to determine the influence of binding of siRNA, EPPT-1 and MPAP on change in surface charge of StAv-SPIONs, electrophoretic mobility of StAv-MNPs on agarose gel electrophoresis with wells casted at the centre of 0.5% agarose gel. Gel was subjected to electrophoresis using TBE buffer at 145V for 1 hour. Agarose gel then stained using mixture of equal volumes of 4% potassium ferrocyanide and 1.2mM hydrochloric acid for 10 min at room temperature. Gel was washed for nonspecific staining using distilled water. Gel was photographed in photoimager and distance traveled at either electrode was evaluated using Image J software.

#### **4.2.24 Serum biochemical estimation**

Blood samples were collected before euthanization by retro-orbital bleeding. Blood samples were centrifuged at 4°C (3000g, 10 minutes) and serum was stored at -20°C for further studies. Serum glucose, bilirubin, blood urea nitrogen, creatinine, aspartate and alanine aminotransaminase were measured using automated blood analyzer at the Institute of clinical chemistry and laboratory medicine, Medical University of Greifswald, Germany.

Serum mouse Cytokine determination CBA kit was used for determination of serum cytokines concentrations (IL6, IL10, IL12p70, and MCP-1. TNF- $\alpha$  and IFN $\gamma$ ) as per manufacturer's instruction briefly, specific cytokine conjugated fluorescence beads were used to couple specific serum cytokine and flow cytometric analysis were performed to determine the cytokine concentration.

#### **4.2.25 Survival analysis**

Tumor bearing mice were enrolled 14 days after syngenic orthotopic tumor implantation. Animals were randomized into three groups to receive siControl-StAv-SPIONs (mismatch control), gemcitabine or siPLK1-StAv-SPIONs respectively. Gemcitabine was administered intraperitoneally (i.p.) twice weekly at a dosage of 50mg/kg. siControl-StAv-SPIONs and siPLK1-StAv-SPIONs were administered intravenously (i.v.) twice weekly at a concentration of 5mg/kg of iron. Treatment schedule was maintained for maximum 12 weeks after initiation of the treatment. Objective response was monitored daily by visual examination of the animals and endpoint criteria were defined as general morbidity, lethargy or lack of social interaction.

#### **4.2.26 Statistical analysis**

Data are expressed as mean  $\pm$  SD unless otherwise stated and analysed using GraphPad Prism 5.0, CA, USA. Normally distributed two-grouped data were analysed using Mann-Whitney test. Multigroup data were analysed by Kruskal-Wallis test followed by Dunn's multiple comparison post-hoc test. Kaplan-Meier survival data was analysed using a log rank

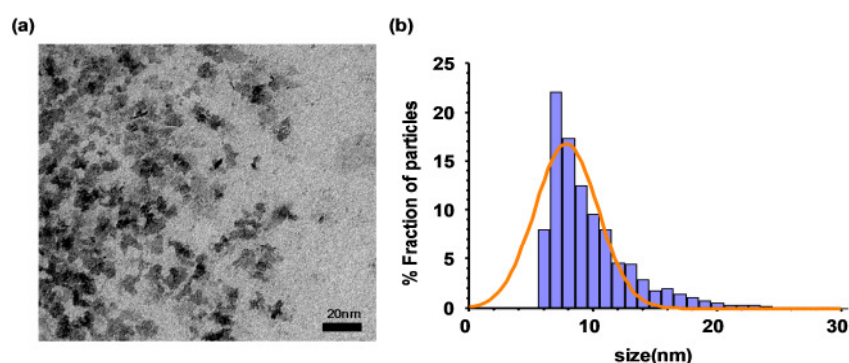
test. Statistical correlations were analysed using Pearson test.  $P < 0.05$  was considered statistically significant.

## 5. RESULTS

### 5.1 siPLK1-StAv-SPIONs congregate the characteristics of superparamagnetic nanoparticles

As a part of systematic effort to minimize the limitations of classical pancreatic ductal adenocarcinoma (PDAC) therapy, we designed dual purpose functional probes comprising of dextran coated superparamagnetic iron oxide nanoparticles (SPIONs) a backbone which can be detected by magnetic resonance imaging (MRI) and which can be further conjugated with StAv. Reflecting the fact of StAv and biotin as the strongest covalent binding, we coupled biotin conjugated myristoylated polyarginine peptides (MPAP-) for translocation of the complex into the cytosol by electrostatic interaction. Underglycosylated MUC1 (uMUC1) is a hallmark of early tumorigenesis, highly expressed and ubiquitously expressed in PDAC. We coupled biotin conjugated EPPT1, a synthetic non-immunogenic peptide sequence derived from tandom repeats of MUC1, targeted to MUC1, allow tumor specific uptake. Moreover we linked biotin conjugated siRNA duplexes targeted against a therapeutic target. The synthesis of PLK1 targeting complex, siPLK1-StAv-SPIONs, resulted in triple-labeled nanoparticles specifically targeted to the pancreatic cancer cells.

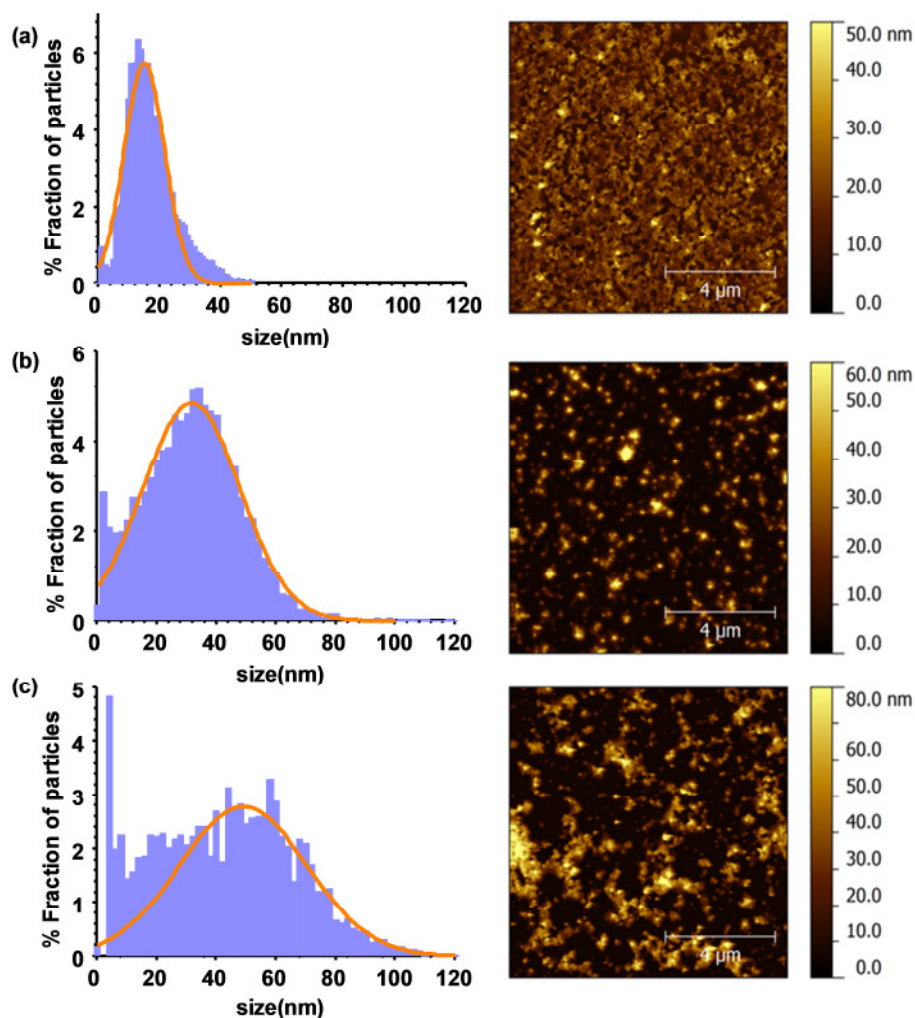
To evaluate the structural features, surface morphology and particle size distribution, we characterized the siPLK1-StAv-MNPs using high resolution transmission electron microscopy (HR-TEM). We adsorbed siPLK1-StAv-SPIONs on copper grids and washed the grids with acetone to remove contamination. HR-TEM microscopy revealed the average SPION core diameter as 10 nm (mean = 9.81 nm) evaluated by using c10 different high magnification fields in Image-J. SPIONs possess characteristic of flakes like structure (**Figure 8**).



**Figure 8: Physical characterization of siPLK1-StAv-SPIONs.** (a) TEM image of SPION core (scale bar = 20nm). (b) Frequency distribution chart showing mean diameter of SPION core is 10nm.

To characterize the surface modifications and structural features of the siPLK1-StAv-MNPs, Atomic force microscopy (AFM) imaging was performed. AFM imaging showed a change in the surface morphology of siPLK1-StAv-SPIONs after conjugations of peptide ligands and

siPLK1 duplex compared to SPIONs alone (**Figure 9**). Frequency distribution charts for height distribution of the grains for SPIONs, StAv-SPIONs and siPLK1-StAv-MNPs showed surface modification and change in diameter of siPLK1-StAv-MNPs. SPIONs showed an even distribution (95% CI: 14.58 to 15.62) over the sections whereas siPLK1-StAv-MNPs showed size distribution over a wide range, (95% CI: 57.53 to 60.52) depicting conjugation with MPAP-, EPPT1- and siPLK1.

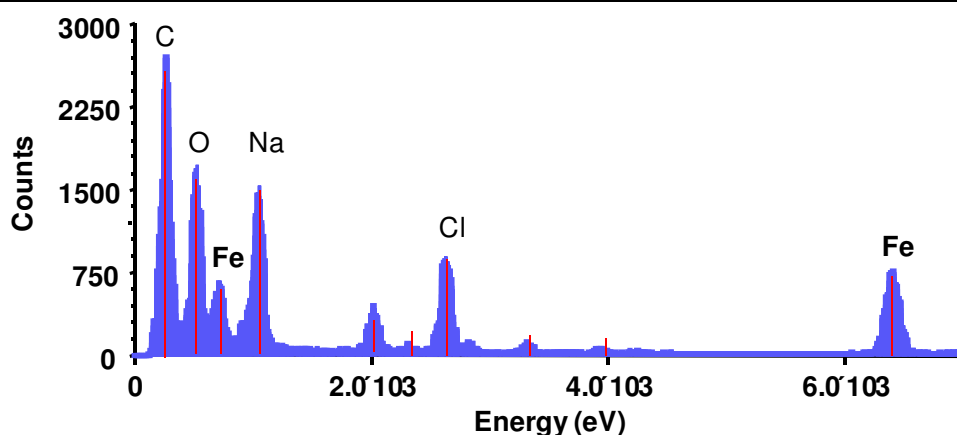


**Figure 9: Surface characterization of siPLK1-StAv-SPIONs.** Diagram shows Atomic Force Microscopy (AFM) images of (a) SPIONs, (b) StAv-SPIONs and (c) siPLK1-StAv-SPION. Bar diagrams represent the size distribution of the respective group.)

In order to evaluate the composition of siPLK1-StAv-SPIONs, we performed electron dispersive X ray spectroscopy (EDX) coupled to HR-TEM and we evaluated the obtained spectra for K-lines of different elements (**Figure 10**). EDX spectral analysis showed composition of siPLK1-StAv-SPIONs as described in **Table 6**. siPLK1-StAv-SPIONs consists of around 45% Iron.

**Table 6: The composition of siPLK1-StAv-SPIONs as determined by Energy-dispersive X-ray spectroscopy**

Element	Line Type	Apparent Concentration	k Ratio	Wt%	Wt% Sigma
C	K series	13.65	0.13645	30.83	0.37
O	K series	39.82	0.13399	21.48	0.23
Na	K series	0.38	0.00162	0.36	0.05
Cl	K series	5.66	0.04949	2.56	0.05
Fe	K series	92.77	0.92769	44.76	0.29
<b>Total:</b>				<b>100.00</b>	

**Figure 10: Composition of siPLK1-StAv-SPIONs.** Bar chart of Energy dispersive X-ray spectroscopy spectra for siPLK1-StAV-SPIONs illustrating characteristics Iron oxide (magnetite) peaks.

With the intention to confirm the crystal nature of magnetite nanoparticles, we performed single area electron diffraction (SAED) analysis coupled to HR-TEM (**Figure 11a**). The diffraction rings in the SAED pattern are well-pronounced, which demonstrates a highly crystalline structure of the SPIONs with rather uniform crystallite size. The lattice parameter for SAED analysis calculated using the diffraction ring profiler revealed siPLK1-StAv-SPIONs are in agreement with the spinel crystal structure of bulk magnetite crystals. It is likely that the single equidimensional particle is magnetite, and responsible for some of the spectral spots on the diffraction pattern in **Figure 11b**. In fact, most of the  $d$  spacings evaluated for crystal structure characterization are a close match to the magnetite standard ( $d$  spacing data in Appendix I).

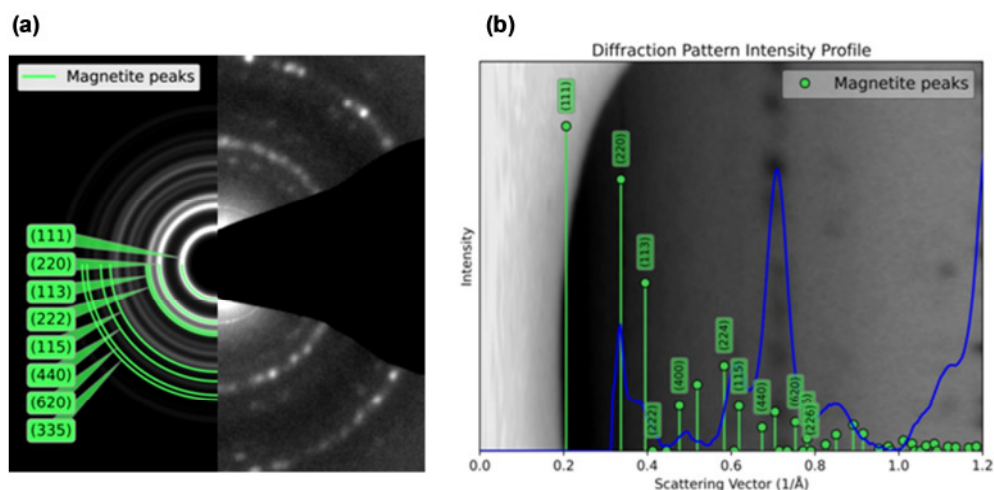


**Figure 11: SAED patterns for siPLK1-StAv-SPIONs, redrawn using diffraction ring profiler.** (a) SAED pattern shows polycrystalline pattern, line numbers assigned as per standard crystal lattice peaks (hkl). (b) SAED single crystal diffraction pattern spots of the siPLK1-StAv-SPIONs are labeled with crystallographic planes of magnetite based on the measured  $d$  spacings. Green spectral lines illustrate standard magnetite diffraction pattern whereas blue illustrates siPLK1-StAv-SPIONs crystal diffraction pattern spots.

Having confirmed the structural features and composition of siPLK1-StAv-SPIONs, we performed dynamic light scattering spectroscopy (DLS) to determine the physiochemical properties and size distribution profile of siPLK1-StAv-MNPs in solution. We evaluated hydrodynamic diameter, the polydispersity index and zeta-potential. When a dispersed particle moves through solution, electric dipole layer adhere to its surface and influence the movement of particles in solution. Hydrodynamic diameter is the measure of a particle core along dipole layers. Hydrodynamic particle diameters with DLS are mostly above the diameter of that measured with TEM or AFM. Zeta potential is the potential difference between the solution and attached stationary dipole layer to the particles. Zeta potential is a key indicator of the stability of nanoparticles in solution. The magnitude of zeta potential indicates the degree of electrostatic repulsion between adjacent, similarly charged particles in a dispersion and zeta potential in the range of  $\pm 30$  to  $\pm 40$  mV determining moderately stable nanoparticles in solution. The polydispersity index depicts the nanoparticles size distribution in the solution. The prepared siPLK1-StAv-SPIONs had a hydrodynamic diameter of  $123 \pm 14$  d.nm. and effective surface charges ( $\zeta$ -potential) of  $-31.20$  mV (**Table 7**).

**Table 7: Physicochemical characterization of siPLK1-StAv-SPIONs**

Parameters	Z-Average (d. nm)	PDI	Zeta Potential (mV)
Dextran-SPIONs (SPIONs)	39 ± 9	0.25	-4.63
StAv-SPIONs	71 ± 18	0.29	-29.6
siPLK1-StAv-SPIONs	123 ± 14	0.21	-31.2

Since StAv conjugation to SPIONs forms the basis for other ligand binding, we evaluated the binding efficiency of StAv to SPIONs. We incubated different concentration of biotinylated BSA (100ng, 200ng and 500ng) with StAv-SPIONs over a period of 60 minutes at 25°C and we measured the hydrodynamic diameter in DLS. We found a concentration dependent stoichiometric increase in the hydrodynamic diameter with a plateau followed by one phase decay (**Figure 12**). Biotinylated BSA (100ng) showed plateau at 90.98 d.nm. whereas biotinylated BSA (550ng) reached the plateau at 129.6 d.nm.

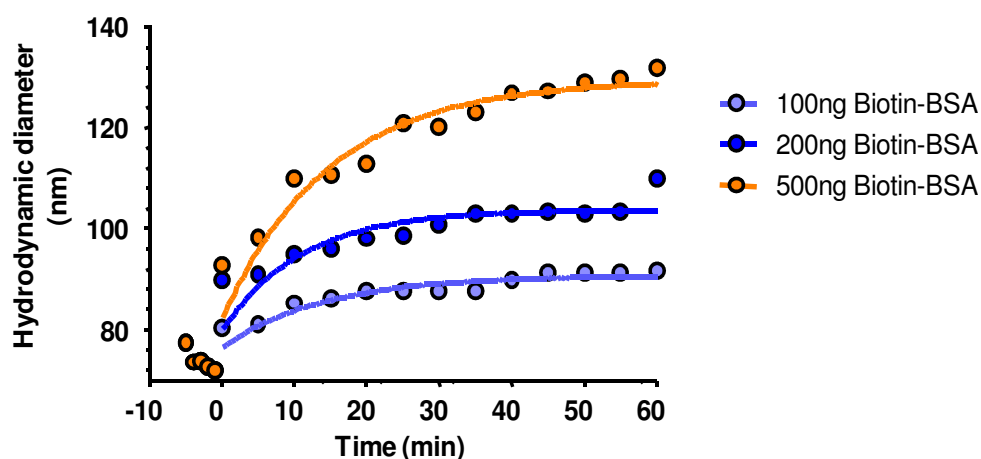


**Figure 12: Evaluation of StAv (StAv) binding efficiency to SPIONs.** Diagram showing binding efficiency of StAv on coupling with SPIONs. Time dependent change in hydrodynamic diameter (d.nm) on incubation of different concentration of biotylated BSA over the period of 60 minutes. Higher concentration of biotinylated-BSA showed time dependent increment in hydrodynamic diameter of particles revealing binding of StAv to SPIONs.

With the intention to evaluate the entrapment of siPLK1 to StAv-SPIONs, we performed quantification of siPLK1 using Ribogreen fluorescence RNA quantification assay and directed against siPLK1 content with  $2.0672 \pm 0.2692$   $\mu\text{g/ml}$  with an entrapment efficiency of  $30.08 \pm 3.91\%$ . We corroborated the siPLK1 duplex binding to StAv-SPIONs using agarose gel electrophoresis (**Figure 13**). We used standard siPLK1 dilutions to establish a standard siPLK1 curve and used 1% SDS to cleave biotin-StAv bonds. We subsequently evaluated released siPLK1 from siPLK1-StAv-SPIONs. We evaluated the intensity of each band using ImageJ. Extrapolation of the intensity to standard curve revealed the siPLK1 content as  $2.0626 \pm 0.6489$   $\mu\text{g/ml}$ . siPLK1-StAv-SPIONs did not show any band revealing binding of siPLK1 to StAv-SPIONs.

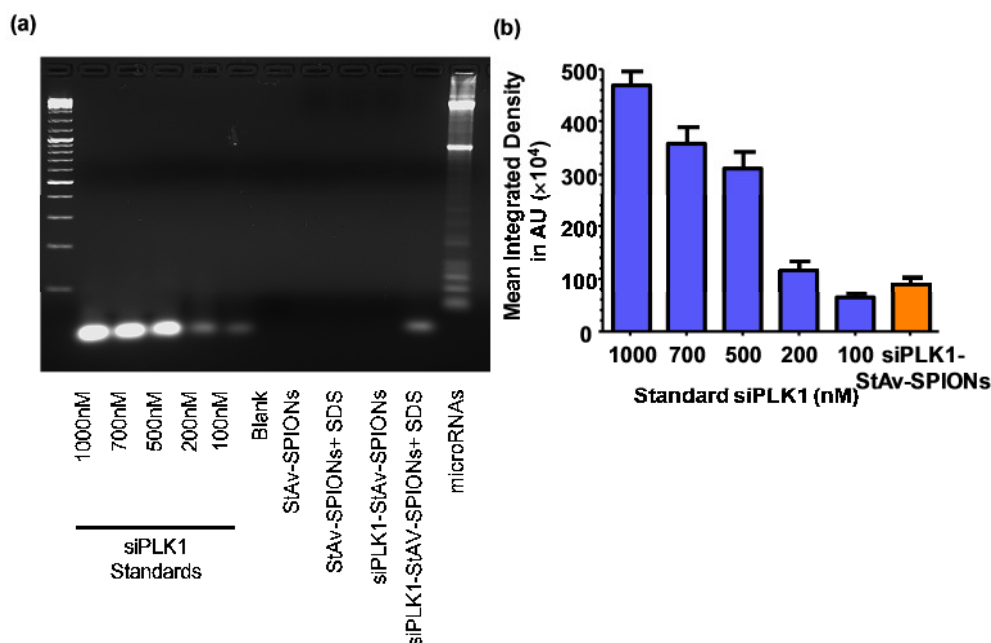


**Figure 13: siPLK1 binding evaluation to StAv-SPIONs.** (a) 2% Agarose gel electrophoresis was performed with standard siPLK1 of different concentrations (100nM to 1000nM) and siPLK1-StAv-SPIONs with and without treatment of 1%SDS. siPLK1 released on SDS treatment was quantified for mean integrated density. (b) Bar diagram showing quantification siPLK1 corresponding to quantification of different concentrations of siPLK1. Data was expressed as mean  $\pm$  SD (n=4).

To evaluate charge differences on conjugation with MPAP and EPPT1 on StAv-SPIONs, we performed electrophoretic mobility on agarose gel followed by iron staining to detect running front of SPIONs. siPLK1, EPPT1 and MPAP conjugation together to StAv-SPIONs showed differential migration than that of conjugation of separate ligands to StAv-SPIONs (**Figure 14**).

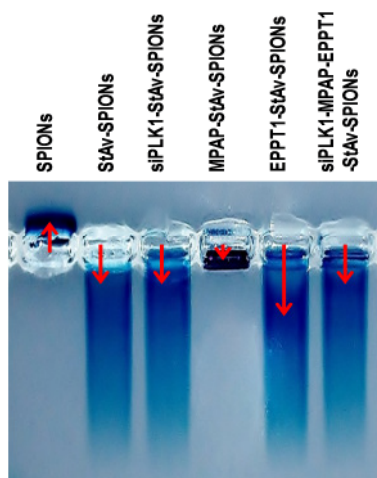


**Figure 14: Electrophoretic mobility of siPLK1-StAv-SPIONs.** Agarose gel electrophoresis of StAv-SPIONs with and without EPPT1 and MPAP, followed by Iron staining revealed

differential migration of SPIONs in presence and in absence of MPAP and EPPT1. Red arrows indicate migration fronts of SPIONs.

Our major concern was entrapment of siPLK1 in StAv coating and therefore its unavailability for a therapeutic effect. With the intention to answer this question, we performed *in silico* docking of biotinylated siPLK1 duplex with StAv (PDB: 1MM9). We performed docking using the PyMol software using default setting. siRNA duplex binding to StAv resulted in siRNA duplex always outside of the StAv with biotin binding to biotin binding site of StAv and not getting entrapped in StAv coating (**Figure 15a**). Thus, siRNA duplex from siPLK1-StAv-SPIONs should always be bioavailable. The other problem related to biotinylated-siRNA was the change in binding efficiency of StAv. In order to evaluate this, we used SwissDock using StAv (PDB: 1MM9) with a biotinylated siRNA duplex. We used biotin as standard. Standard biotin showed strong covalent binding to StAv with a relative free energy of -18.05 kcal/mol depicting stable binding in conjugation with relative free energy of biotin-StAv (**Figure 15b-c**). The biotinylated-siRNA duplex showed relative free binding energy to be decreased to -11.52 kcal/mol (**Figure 15d**), due to the cancellation of dispersion and repulsion cavity effects. In a protein, very small free energy price must be paid to create a cavity since one cavity already exists. These results are consistent with the interpretation that the entropy increase to be expected from hydrophobic interactions from biotin is counterbalanced by a decrease in entropy accompanying the formation of hydrogen bonds by siRNA duplex.

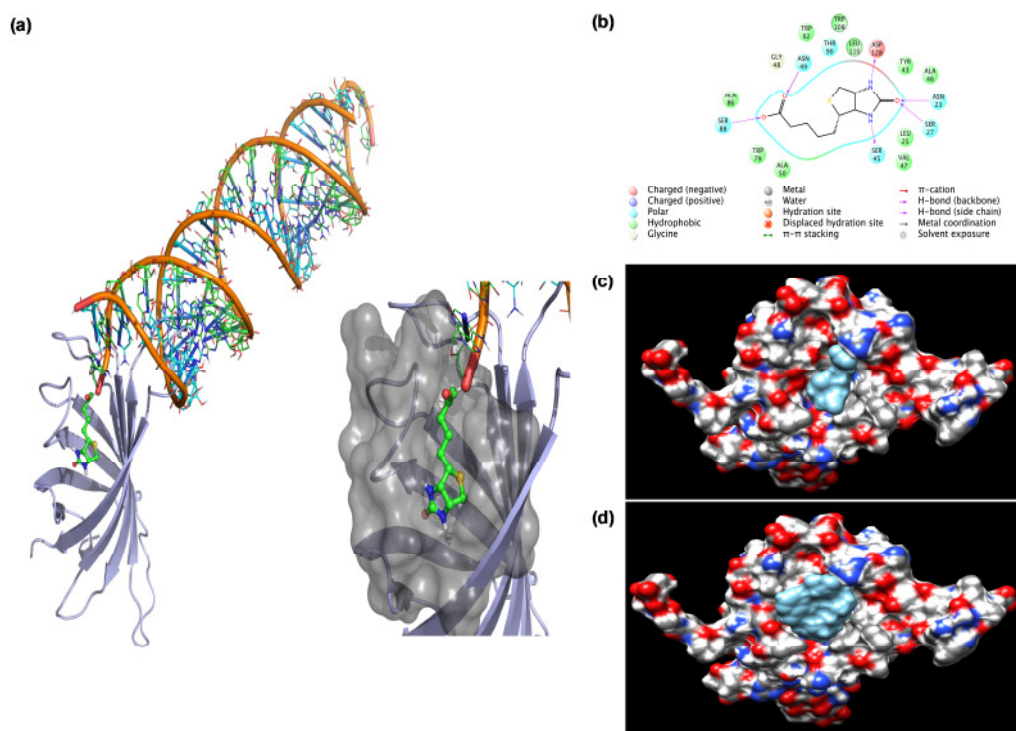


**Figure 15: *In-silico* modeling of siPLK1 binding to StAv.** (a) *In-silico* modeling of conjugation of biotinylated siRNA (Green Biotin) with StAv (gray ribbons) revealed the binding of siRNA is always above the surface of StAv and not interacting with StAv coating. Diagram in insert shows biotin binding to biotin binding pockets of StAv. (b) *In-silico* docking

illustrating biotin binding in biotin binding pockets of StAv. (c) *In-silico* docking of Biotin with StAv at relative free binding energy as -18.03 kcal/mol. Biotin (in blue) depicts binding to StAv. (d) *In-silico* docking of biotinylated-siRNA with StAv at relative free binding energy as -11.89 kcal/mol. Biotinylated siRNA (in blue) depicts binding to StAv. with no interaction of siRNA with StAv.

In order to evaluate theoretical binding of siPLK1 and StAv, we performed stoichiometric calculations considering the fact of core diameter of SPIONs, crystal structure and 4 biotin binding sites per StAv molecule. Stoichiometric calculations revealed approximately 45 actual biotin binding sites per SPIONs with approximately 5 siPLK1 binding per SPIONs (**Table 8**, complete calculations in Appendix II and III).

**Table 8: Stoichiometric calculations for binding and conjugation on SPIONs**

Parameters	unit value
Average diameter of SPION core	10 nm
Average number of StAv molecules/SPIONs (Theoretical)	~60
Average number of Biotin binding sites/SPIONs (Theoretical)	~240
Average number of Biotin binding sites/SPIONs (Actual)	~45
Average number of siRNAs/SPIONs	~5

In all, these results suggest the synthesis of well characterized triple-labeled and functional siPLK1-StAv-SPIONs for targeted delivery towards the tumor.

### 5.2 PLK1 targeting by means of siPLK1-StAv-SPIONs impede tumor cell growth

Our study was based on hypothesis that suppression of PLK1 would prevent tumor proliferation by arresting the cells in G2/M phase of mitosis. We first sought to analyze the uptake of the siPLK1-StAv-SPIONs in tumor cells. We incubated the pancreatic ductal adenocarcinoma cell-line, 6606PDA with 50 $\mu$ M siPLK1-StAv-SPIONs and found a brownish tinge after 2 hour treatment in the cell pellets compared to control cells with white pellets (**Figure 16a-b**). To quantify the uptake and efficiency of siPLK1-StAv-SPIONs directed against PLK1, we incubated, 6606PDA cells with 50 $\mu$ M siPLK1-StAv-SPIONs and analysed the amount of intracellular iron uptake after 2 and 4 hours of incubation using a colourimetric intracellular iron uptake assay. There was a significant increase in intracellular iron concentration reflecting increased uptake of siPLK1-StAv-SPIONs by the cells (**Figure 16c**). Dextran-SPIONs did not show any significant intracellular iron content after 2 and 4 hours of treatment (data not shown).

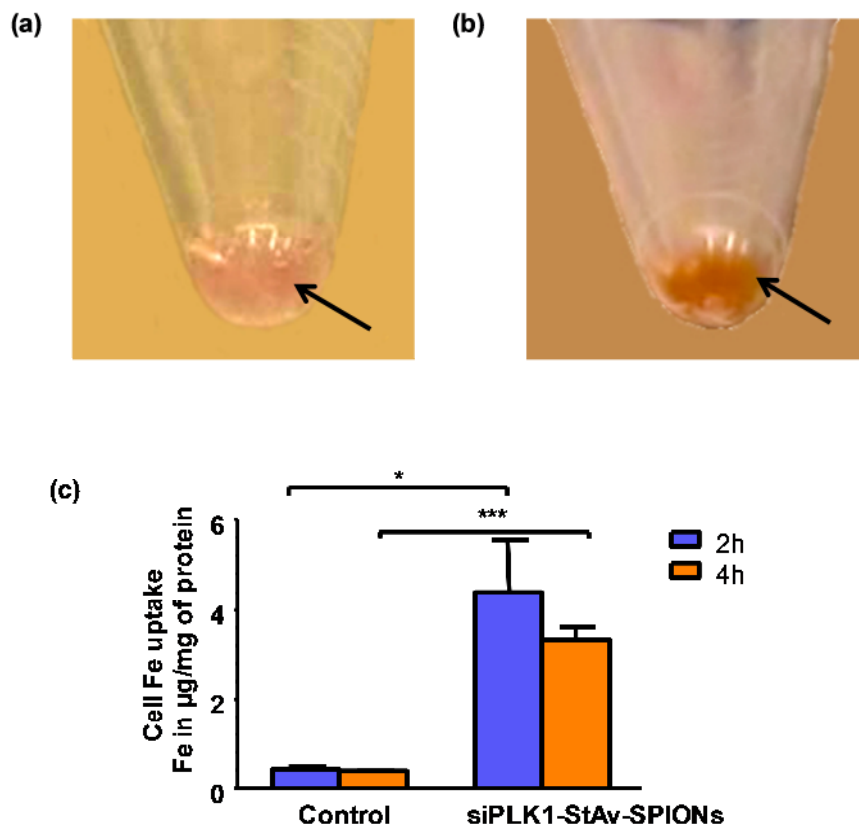


**Figure 16: Quantitative analysis of the uptake of siPLK1-StAv-SPIONs into tumor cells.** (a-b) Representative images of control cells, a, and siPLK1-StAv-SPION treated cells, b, 2 hours after treatment of 50  $\mu$ M of siPLK1-StAv-SPIONs. After 2 hours treatment, cells were washed with PBS and trypsinized and pellet was collected. (b) Graphical representation of quantitative siPLK1-StAv-SPIONs uptake was estimated by iron content in cell lysates after 2 and 4 hours treatment showing significant uptake of Iron in cells on 2 hours and 4 hours incubation. Data represented as mean  $\pm$  SD (n =3-6).

6606PDA cells derived from LSL-Kras<sup>G12D</sup>, Pdx-1-Cre (KC) mice, regained their diploid chromosome ( $2n$ ) content for 18 hours under normal circumstances. In order to evaluate the efficiency of siPLK1-StAv-SPIONs in inhibiting the cell cycle in  $G_2/M$  phase transition thus providing stagnancy in  $G_2/M$  phase, we incubated cells for 18 hours with siPLK1-StAv-SPIONs in comparison to control untreated cells, naked siPLK1 duplex, 5 Fluorouracil (5FU), Gemcitabine, Nocodazole, BI6727, siPLK1 transfection by means of electroporation and siControl-StAv-SPIONs. Untreated control served as negative control; naked siPLK1 duplex and siControl served as mismatch controls, 5FU and Gemcitabine as S phase inhibitor ( $G_1$  phase stagnancy), Nocodazole as  $G_2/M$  phase transition inhibitor, whereas BI6727 resembles a PLK1 specific inhibitor with high bioavailability. siPLK1 transfection by electroporation provided the efficiency of siPLK1 in silencing PLK1. After 18 hours of incubation, we collected the cells and performed cell cycle cell cytometric analysis using propidium iodide. Cell cytometric analysis revealed a pronounced increase in the number of cells in  $G_2/M$  phase (266% increase) up on treatment with siPLK1-StAv-SPIONs. The PLK1

inhibitor, BI6727 confirmed a corresponding increase in the G<sub>2</sub>/M phase, pointing to equal efficacy of siPLK1-StAv-SPIONs in silencing PLK1 in tumor cells. siPLK1 transfection showed similar trend compared to siPLK1-StAv-SPIONs treatment. Mismatch control siControl-StAv-SPIONs did not show any alteration in cell cycle progression. 5FU and gemcitabine showed mitotic arrest in the G<sub>1</sub> phase while nocodazole arrested the cell cycle in the G<sub>2</sub>/M transition phase (**Figure 17**).

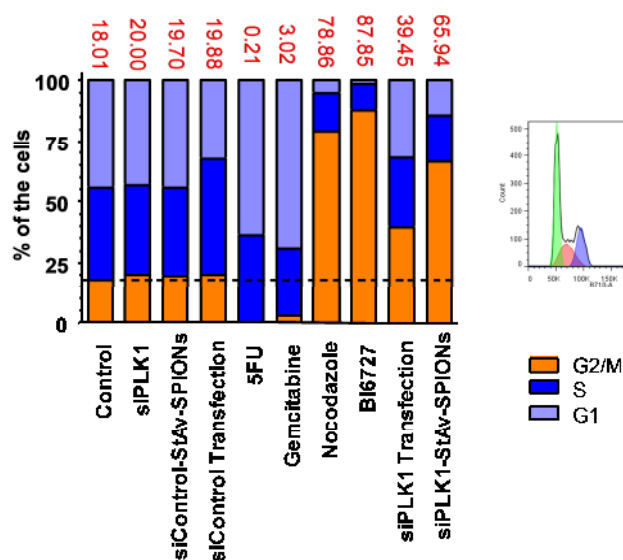


**Figure 17: siPLK1-StAv-SPIONs are efficacious in silencing PLK1 and thus manifesting its effect on cell division.** The silencing effect of PLK1 by siPLK1-StAv-SPIONs was manifested as the change in % of cells in the cell cycle of analysed using FACS analysis. siPLK1-StAv-SPIONs treatment showed stagnancy of the cells in G<sub>2</sub>/M phase of cell cycle (~66%) compared to that of control (~18%). 5-FU (G<sub>1</sub> stagnancy), gemcitabine (G<sub>1</sub> stagnancy), Nocodazole (G<sub>2</sub>/M stagnancy) and BI6727 (specific PLK1 small molecule inhibitor, G<sub>2</sub>/M stagnancy) served as controls for respective phases of cell cycle. Diagram in insert showing cell cycle peaks illustrating G<sub>1</sub>, S and G<sub>2</sub>/M phase.

In order to illustrate the efficacy of PLK1 silencing by on siPLK1-StAv-SPIONs, we measured the influence of siPLK1-StAv-SPIONs on proliferation of 6606PDA cells. We treated 6606PDA cells with siPLK1-StAv-SPIONs. Untreated control cells, mismatch siRNA control, siControl-StAv-SPIONs, siPLK1 and siControl transfection by electroporation served as controls while measuring BrdU proliferation. Following incubation for 0, 6, 18, 24, 36 and 48 hours, we confirmed the silencing efficacy of siPLK1-StAv-SPIONs represented by apparent suppression in proliferation of 6606PDA cells ranging from 18 to 36 hours compared to that of negative control. In siPLK1-StAv-SPIONs treatment, we found suppression in the rate of proliferation of 6606PDA cells. Mismatch control siControl-StAv-SPIONs did not demonstrate effect on proliferation over the period of 48 hours. siPLK1 transfection by electroporation served as positive control (**Figure 18**).

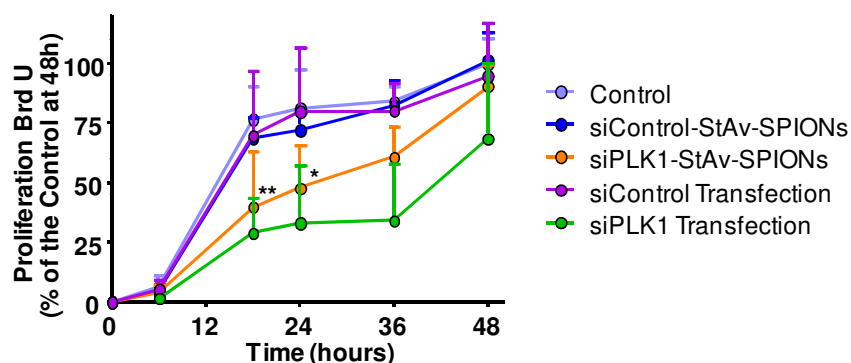


**Figure 18: siPLK1-StAv-SPIONs are efficacious in reducing tumor cell proliferation *in vitro*.** Quantitative estimation of BrdU positive cell proliferation over a period of 48 hours showed a significant decrease in proliferation of the murine pancreatic cancer cell-line 6606PDA on treatment of siPLK1-StAv-SPIONs. Data represent mean  $\pm$  SD (n= 3 individual experiments), \*\*\* p<0.001, \*\* p<0.01, \* p<0.05.

One of the concerns with siPLK1-StAv-SPIONs was a non-specific effect of SPIONs owing to generation of reactive oxidative species (ROS) and thus contributing to cytotoxicity. In order to test whether siPLK1-StAv-SPIONs lead to generation of ROS, we performed DCFDA fluorescent assay. After 2 and 4 hours incubation of 50 $\mu$ M siPLK1-StAv-SPIONs with 6606PDA cells showed no toxicity and less ROS production (**Figure 19**).

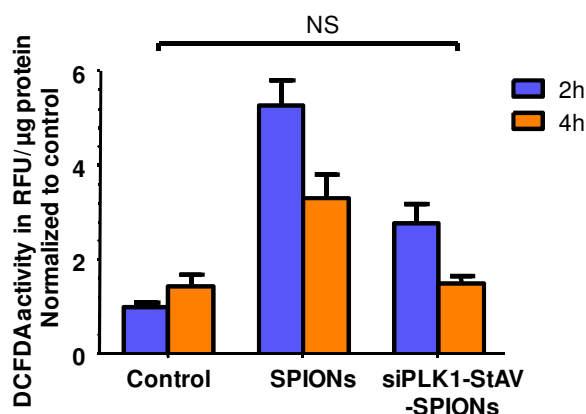


**Figure 19: *In vitro* tolerance on generation in reactive oxygen species on treatment of siPLK1-StAv-SPIONs.** DC-FDA fluorescence was evaluated after 2 and 4 hours of treatment of MNPs and siPLK1-StAv-SPIONs showed better tolerance than siPLK1-StAv-SPIONs. Data was expressed as mean  $\pm$  SD (n=3).

We performed in-solution stability with the aim to establish duration of solution stability. We incubated siPLK1-StAv-SPIONs in nuclease free saline at 37<sup>o</sup>C for 0, 4, 7 and 14 days and evaluated the efficacy on cell cycle upon 18 hours of incubation on 6606PDA cells. siPLK1-StAv-SPIONs are stable in solution for around 4 days (**Figure 20**).

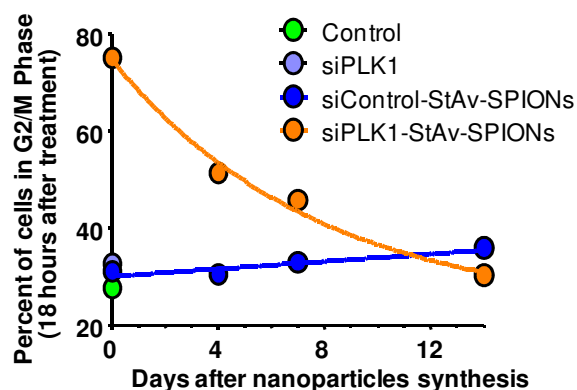


**Figure 20: In solution stability of siPLK1-StAv-SPIONs.** siPLK1-StAv-SPIONs were incubated in nuclease free saline at 37°C for 0, 4, 7 and 14 days. The influence of siPLK1-StAv-SPIONs on stabilizing G2/M phase of cell cycle was evaluated. It was observed that siPLK1-StAv-SPIONs are stable in solution for around 4 days.

The aforementioned results exhibit the functional efficacy of siPLK1-StAv-SPIONs with better tolerance in *in-vitro* system determining successful delivery of siPLK1-StAv-SPIONs to the tumor cells.

### 5.3 Uptake of siPLK1-StAv-SPIONs is specific for tumor cells and depends on clathrin mediated endocytosis

We next sought to assess the uptake specificity and possible uptake mechanism of siPLK1-StAv-SPIONs to the tumor cells. Underglycosylated MUC1 (uMUC1) expression on tumor cell surface form the basis of specificity of siPLK1-StAv-SPIONs. We confirmed the abundance of uMUC1 expression on cancer cells with apparent predominance on the cell surface (**Figure 21**) using immunofluorescence staining of MUC1 in 6606PDA cells.

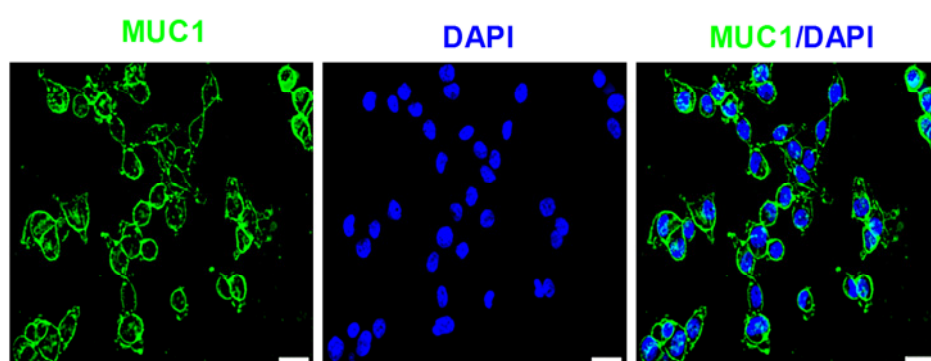


**Figure 21: Immunofluorescence staining of MUC1 showing surface localization of the MUC1 on the pancreatic cancer cell-line, 6606PDA.** Scale bar = 50µm.

To monitor specific uptake of siPLK1-StAv-SPIONs, we performed confocal live cell imaging with Cy5 labeled siPLK1-StAv-SPIONs. We incubated Cy5 labeled siPLK1-StAv-SPIONs with and without MPAP and EPPT1 peptides over the period of 30 minutes. We monitored the uptake using time-lapse live cell imaging. We found evident uptake of MPAP (+) EPPT1

(+) Cy5 labeled siPLK1-StAv-SPIONs in cancer cells starting as early as after 5 minutes. MPAP (-) EPPT1 (-) Cy5 labeled siPLK1-StAv-SPIONs didn't show marked increase in uptake over the period of 30 minutes (**Figure 22a**). Analysis of the mean fluorescent intensity for Cy5 for approximately 100 random cells using CellSens software revealed significant increase in MPAP(+)/EPPT1(+)/Cy5 labeled siPLK1-StAv-SPIONs compared to corresponding control without peptide ligands conjugated to SPIONs (**Figure 22b**).

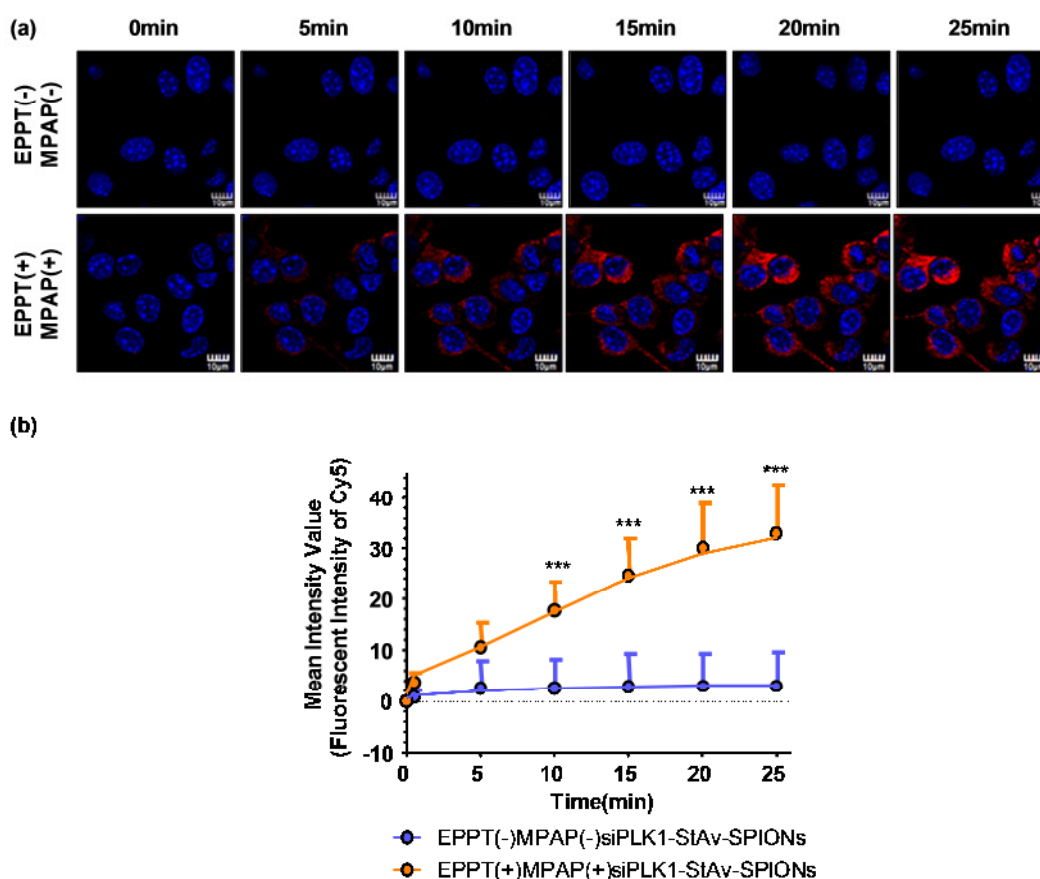


**Figure 22: Uptake of siPLK1-StAv-SPIONs is mediated by uMUC1 and MPAP.** (a) Confocal microscopy showed accumulation of siPLK1-StAv-SPIONs coupled to EPPT1 and MPAP (MPAP (+) EPPT1 (+) siPLK1-StAv-SPIONs) in 6606PDA cells over the time period of 30 minutes. In contrast, for siPLK1-StAv-SPIONs without EPPT1 and MPAP (MPAP (-) EPPT1 (-) SPIONs) we did not detect uptake of nanoparticles over the time period of 30 minutes. Red fluorescence depicts nanoparticles (Cy5) and blue depicts nuclei (DAPI); (scale bar=10 $\mu$ m). (b) Quantification of confocal images recorded over the time period of 30 minutes. SiPLK1-StAv-SPIONs uptake was quantified as mean fluorescence intensity of Cy5. Data are expressed as mean  $\pm$  SD. \*\*\* $p$ <0.001, \*\* $p$ <0.01, \* $p$ <0.05 considered statistically significant.

We confirmed this findings using flow cytometric analysis, on incubation with MPAP (+) EPPT1 (+) Cy5 labeled siPLK1-StAv-SPIONs for a period of 30 minutes. Upon treatment with Cy 5 (red) conjugated siPLK1-StAv-SPIONs, cells were fixed, permeabilized and evaluated for Cy5 (red) positive cells marking siPLK1-StAv-SPIONs. Flow cytometric analysis showed high siPLK1-StAv-SPIONs uptake in MPAP(+)/EPPT1(+)/Cy5 labeled siPLK1-StAv-SPIONs

treated cells compared to no or one of the peptide ligands conjugated Cy5 labeled siPLK1-StAv-SPIONs (**Figure 23**).

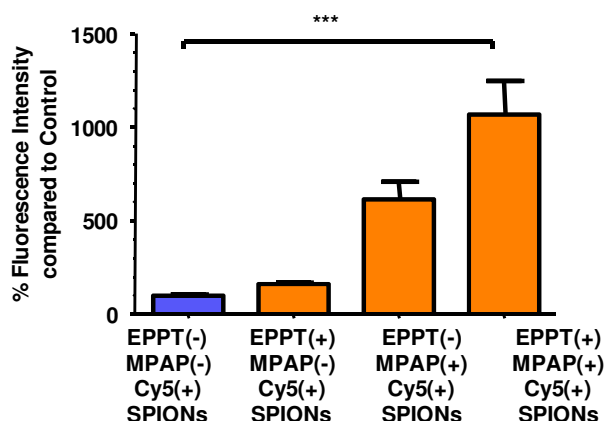


**Figure 23: *In-vitro* uptake analysis of siPLK1-StAv-SPIONs using fluorescence associated cell sorting.** Quantitative analysis showed the percentage of uptake of siPLK1-StAv-SPIONs with EPPT1 and MPAP [MPAP (+) EPPT1 (+) SPIONs] in 6606PDA. SiPLK1-StAv-SPIONs without EPPT1 and MPAP [MPAP (-) EPPT1 (-) SPIONs] were taken up to a lesser extent. \*\*\* $p < 0.001$ , \*\* $p < 0.01$ , \* $p < 0.05$  considered statistically significant.

These previous set of experiments lead us to the requirements of MPAP and EPPT1 for the uptake in tumor cells. In order to evaluate the specificity of uptake to tumor cells, we incubated 6606PDA cells for 30 minutes with increasing concentration of uMUC1 antibody (0.5 to 2.5  $\mu\text{g/ml}$ ) to block the uMUC1 sites for specific uptake prior to treatment of Cy5 labeled siPLK1-StAv-SPIONs. We found a decrease in uptake of Cy5 labeled siPLK1-StAv-SPIONs, stoichiometric to the uMUC1 antibody concentration (**Figure 24a**). Analysis of approximate 100 random cells showed significant decrease in Cy5 fluorescent intensity compared to corresponding control. Oregon green 488 served as marker for cell borders for the analysis (**Figure 24b**). MUC1 antibody pre-treatment blocks the extracellular MUC1 binding site of EPPT1 thus rendering its effectiveness to specific targeting to the tumor cells. The decreased uptake of Cy5 labeled siPLK1-StAv-SPIONs revealed a MUC1 specific uptake mechanism of siPLK1-StAv-SPIONs.

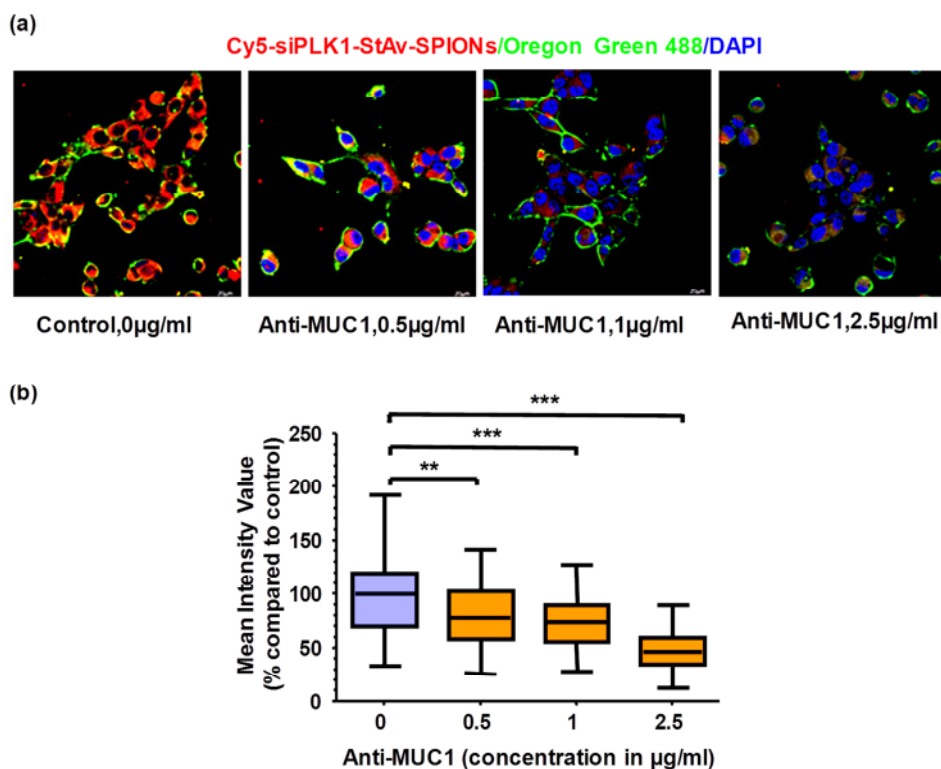


**Figure 24: Uptake of siPLK1-StAv-SPIONs is tumor specific and mediated by MUC1.** (a) Blockage of MUC1 by Anti-MUC1 antibody showed a concentration dependent reduction in the uptake of siPLK1-StAv-SPIONs. (b) Quantification of mean intensity value of Cy5 in relation to anti-MUC1 antibody concentration blocking the uptake of siPLK1-StAv-SPIONs (n= 80-100 cells from 4 different experiments). \*\*\*p<0.001, \*\*p<0.01, \*p<0.05 considered statistically significant.

We corroborated these results with flow cytometric analysis. uMUC1 antibody treated cells 30 minutes prior to Cy5-labeled siPLK1-StAv-SPIONs incubation, showed a concentration dependent decrease in siPLK1-StAv-SPIONs uptake as monitored by Cy5 fluorescent intensity compared to corresponding controls (**Figure 25**). This set of data revealed the uptake of siPLK1-StAv-SPIONs is EPPT1 and MPAP dependent and is specific for tumor cells by selective anchorage dependent uptake by EPPT1.

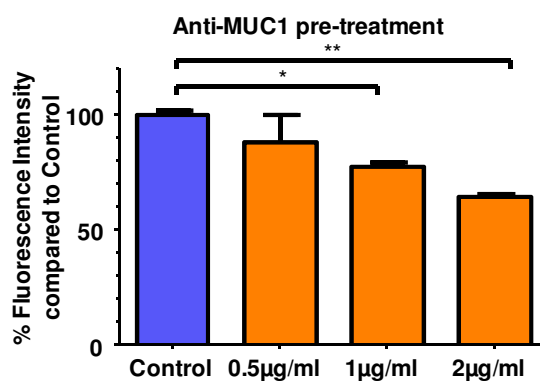


**Figure 25: Uptake of siPLK1-StAv-SPIONs is tumor specific and mediated by MUC1 as evaluated by FACS.** Quantitative analysis showed a decrease in uptake of siPLK1-StAv-

SPIONs after anti-MUC1 treatment. \*\*\* $p < 0.001$ , \*\* $p < 0.01$ , \* $p < 0.05$  considered statistically significant.

To assess the possible functional mechanism of uptake in cells, we hypothesized endocytosis as the possible mechanism for uptake considering the size, particle charge and physical characteristics which determine the chances of passive diffusion or active transport. To further validate this notion, we treated 6606PDA cells with increasing concentration of clathrin dependent endocytosis inhibitor, Dynasore (0 to 50 $\mu$ M) 30 minutes prior to the siPLK1-StAv-SPIONs incubation. We found that endocytosis inhibition abated siPLK1-StAv-SPIONs uptake (**Figure 26a**). We analysed approximate 100 random cells that showed significant decrease in Cy5 fluorescent intensity compared to corresponding controls (**Figure 26b**).

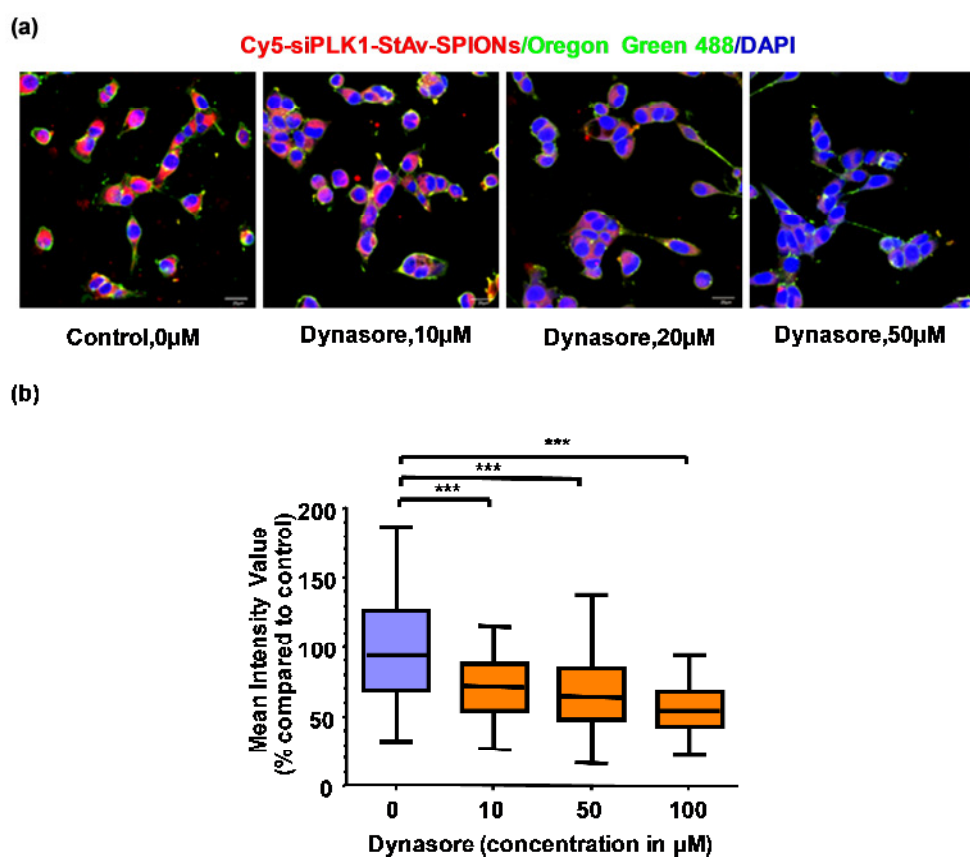


**Figure 26: Uptake of siPLK1-StAv-SPIONs is mediated by clathrin dependent endocytosis.** Quantitative analysis showed a decrease in uptake of siPLK1-StAv-SPIONs after Dynasore treatment. \*\*\* $p < 0.001$ , \*\* $p < 0.01$ , \* $p < 0.05$  considered statistically significant.

We confirmed this finding with flow cytometric analysis. Dynasore treated cells preceding to Cy5-labeled siPLK1-StAv-SPIONs incubation, showed deflated siPLK1-StAv-SPIONs uptake over the concentration range of 10-100 $\mu$ M (**Figure 27**).

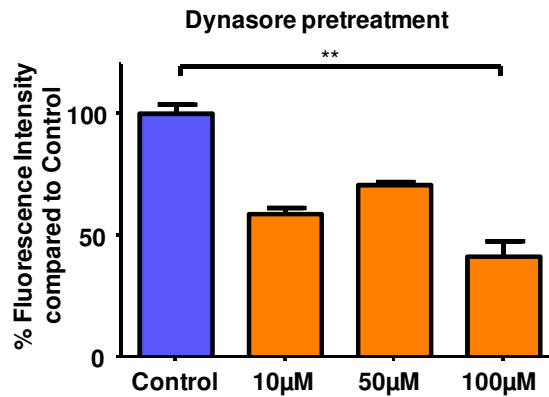


**Figure 27: Uptake of siPLK1-StAv-SPIONs is mediated clathrin dependent endocytosis evaluated using FACS.** Quantitative analysis showed a decrease in uptake of siPLK1-StAv-SPIONs after Dynasore treatment. \*\*\* $p < 0.001$ , \*\* $p < 0.01$ , \* $p < 0.05$  considered statistically significant.

To further substantiate this finding, we evaluated the subcellular localization of siPLK1-StAv-SPIONs on TEM imaging. We incubated 6606PDA cells with 50µM siPLK1-StAv-SPIONs for 30 minutes and fixed the membrane as mentioned in materials and methods. We detected endosomal localization of siPLK1-StAv-SPIONs as early as 5 min after siPLK1-StAv-SPIONs treatment (**Figure 28**) while cytoplasmic localisation became apparent at later time points. 0 minute images did not show any accumulation of siPLK1-StAv-SPIONs.

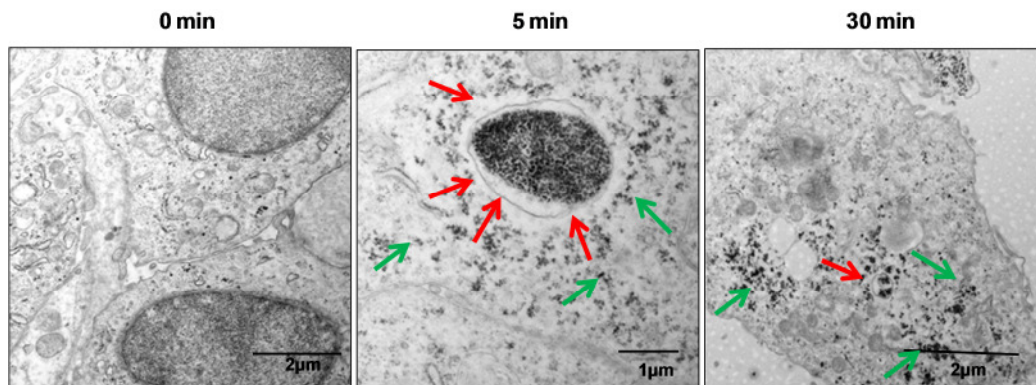


**Figure 28: Uptake of siPLK1-StAv-SPIONs is mediated clathrin dependent endocytosis evaluated using TEM imaging.** Representative images of transmission electron microscopy revealed absent SPIONs at 0 min and uptake of siPLK1-StAv-SPIONs into the endosomal compartment (red arrow) as early as 5 minutes. After 30 minutes, most of the siPLK1-StAv-SPIONs are detected in the cytoplasm (green arrows). The release from endosomal compartment to cytoplasm is believed to be due to the proton sponge effect.

TEM imaging revealed siPLK1-StAv-SPIONs accumulation in early endosomes as early as 5 minutes after treatment. To mediate effective RNAi, the siRNA needs to undergo dissociation from the nanoparticle complex, followed by endosomal escape and entry into the cytosol, where RNA-induced silencing complex (RISC) assembly and target mRNA degradation takes place. Our SPIONs are capable of endosomal escape most likely due to the proton sponge effect exerted by the presence of secondary and tertiary amines coupled to SPIONs, namely

MPAP, which ensure a significant proton buffering. We corroborated these findings using immunofluorescence analysis. Co-localization with the early endosomal marker, EEA1 over a period of 30 minutes revealed that siPLK1-StAv-SPIONs were not completely co-localized with EEA1 over a period of 30 minutes. This notion was supported by quantitative analysis of co-localization using Pearson co-localization coefficient. Pearson co-localization coefficient is in range of 0 to 1, 0 being no colocalization whereas 1 being complete colocalization. It showed siPLK1-StAv-SPIONs and EEA1 were localized in different subcellular compartments (**Figure 29**).

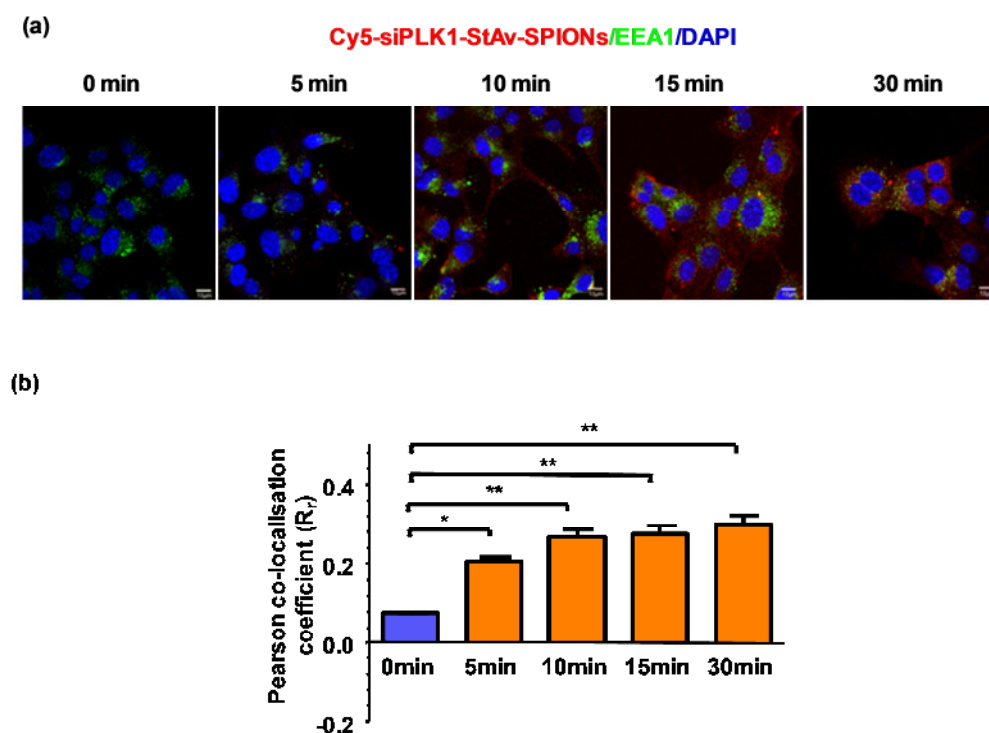


**Figure 29: Co-localization of siPLK1-StAv-SPIONs with endosomes.** Treatment of Cy5 conjugated siPLK1-StAv-SPIONs for 0, 5, 10, 15 and 30 min showed co-localization of Cy5 conjugated siPLK1-StAv-SPIONs with EEA-1, an endosomal marker as early as 5 min. (a) Representative images showed co-localization at different time points. (b) Pearson co-localization coefficient, depicting approx. 20% Cy5 conjugated siPLK1-StAv-SPIONs co-localized with EEA1 at a given time point as shown in the bar diagram. Data expressed as mean  $\pm$  SD from 4 individual experiments. \*\* $p < 0.01$ , \* $p < 0.05$  considered statistically significant.

This data set support the notion that uptake of siPLK1-StAv-SPIONs explicit to the tumor cells, dependent on MPAP and MUC1-selective peptide and is driven by clathrin mediated endocytosis.

#### 5.4 siPLK1-StAv-SPIONs selectively taken up in the tumor and are detected by MRI imaging

To monitor the delivery of siPLK1-StAV-SPIONs to the tumor we employed magnetic resonance imaging in mice bearing syngenic orthotopic tumors before and 6 hours after

intravenous injection of siPLK1-StAv-SPIONs. Superparamagnetic iron-oxide nanoparticles possess predominant proton relaxation rates of the surrounding water proton spins which is associated with the magnetic susceptibility of the particles leading to  $T_2$  relaxation and giving rise to signal reduction on  $T_2$  weighted images. As per our anticipation, siPLK1-StAv-SPIONs showed significant diminution in  $T_2$  relaxivity as evident by decrease in contrast in tumor compared to tumor before siPLK1-StAv-SPIONs treatment 6 hours after intravenous application (**Figure 30**).

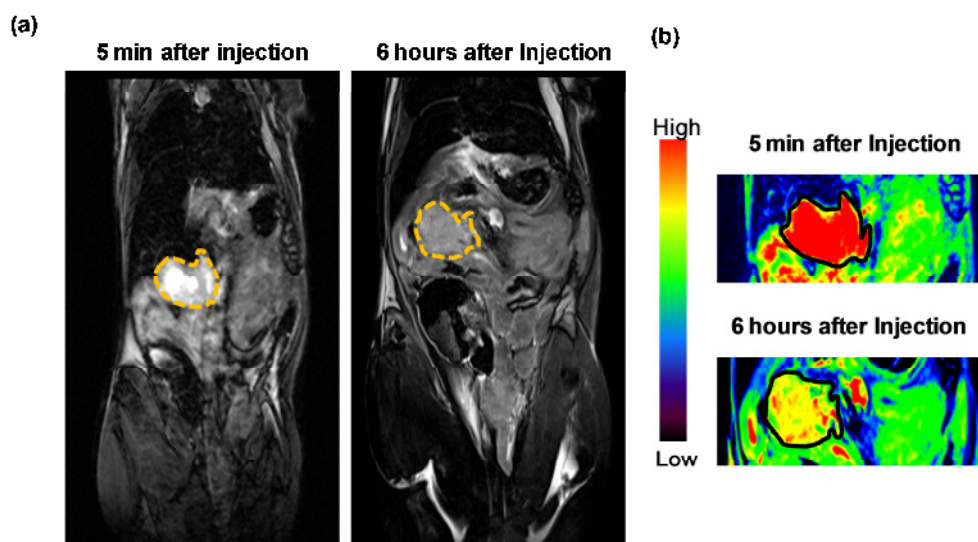


**Figure 30: *In vivo* imaging of delivery of siPLK1-StAv-SPIONs to the tumor.** (a) *In vivo* MRI was performed on the mice bearing syngenic orthotopic tumors before and 6 hours after intravenous administration of siPLK1-StAv-SPIONs. After injection of siPLK1-StAv-SPIONs, there was reduction in  $T_2$  relaxivity in the tumors as evident by a decrease in contrast. (Dotted lines mark the periphery of tumor). (b) Color contrast images show reduction in  $T_2$  relaxivity compared to that before injection.

We further validated the accumulation of the siPLK1-StAv-SPIONs in tumor using quantitative analysis for iron overload calculating using  $R_2^*$  single peak fat corrected echo images. A  $R_2^*$  value over  $100\text{s}^{-1}$  as considered to show surfeit of iron in the tissue. siPLK1-StAv-SPIONs treated animals showed a significant increment in  $R_2^*$  values if compared to control (**Figure 31**).

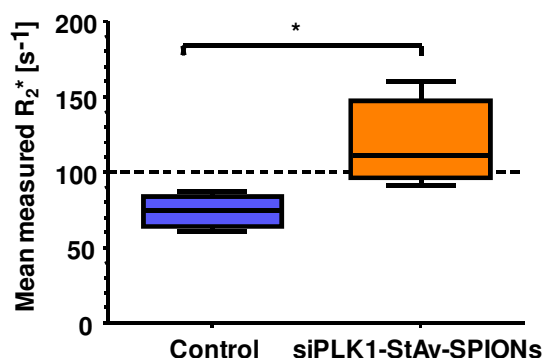


**Figure 31:** *In vivo* MRI was performed on the mice bearing a syngenic orthotopic tumor before and 2 hours after intravenous administration of siPLK1-StAv-SPIONs. Quantitative analysis of iron overload in tumor calculated using  $R_2^*$  fat corrected single peak echo images. siPLK1-StAv-SPIONs treated animals showed a significant iron overload in the tumor (n= 4-5). \*\*\* $p < 0.001$ , \*\* $p < 0.01$ , \* $p < 0.05$ .

We also confirmed accumulation of siPLK1-StAv-SPIONs using Perl's iron staining in tumors harvested after 6 hour of treatment with siPLK1-StAv-SPIONs. The images show accumulation of siPLK1-StAv-SPIONs (blue) in the tumor tissue (**Figure 32**).

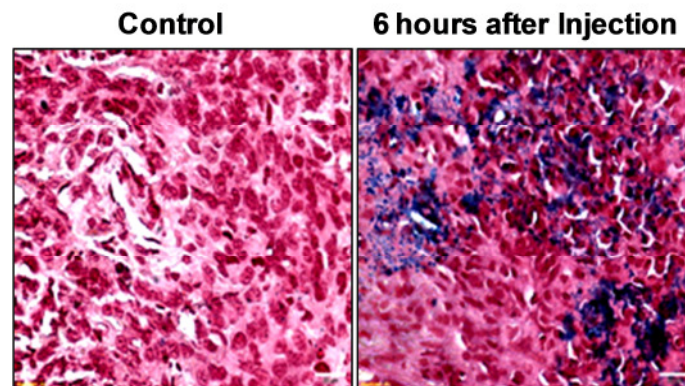


**Figure 32:** Perl's iron staining in tumors 6 hours after injection indicated presence of siPLK1-StAv-SPIONs inside the tumor (Blue), confirming delivery of siPLK1-StAv-SPIONs to the tumor. (scale bar=20 $\mu$ m).

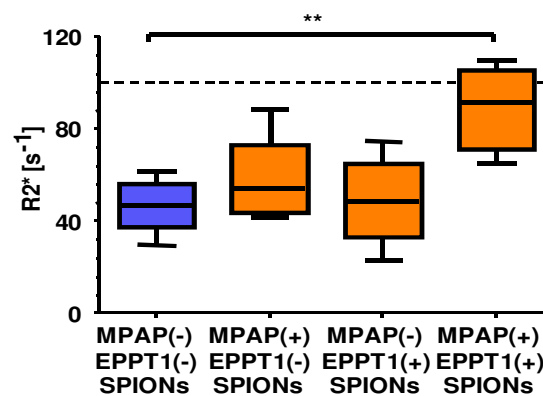


**Figure 33:** Influence of MPAP and EPPT1 on iron overload in tumor. Iron overload was calculated using quantitative analysis of  $R_2^*$  fat corrected single peak echo images. MPAP(+)EPPT1(+) siPLK1-StAv-SPIONs treated animals showed significant iron overload. \*\*\* $p < 0.001$ , \*\* $p < 0.01$ , \* $p < 0.05$ .

We confirmed the uptake of siPLK1-StAv-SPIONs and importance of MPAP and EPPT1 for tumor specific uptake in the syngenic orthotopic tumor model of siPLK1-StAv-SPIONs with and without MPAP and EPPT1. MPAP and EPPT are necessary for siPLK1-StAv-SPIONs tumor specific uptake (**Figure 33**).

We confirmed MPAP and EPPT1 assuming for tumor specific uptake using intracellular tumor Iron content. We found that MPAP and EPPT1 conjugated siPLK1-StAv-SPIONs showed significant Iron overload if compared to that of control (**Figure 34**).

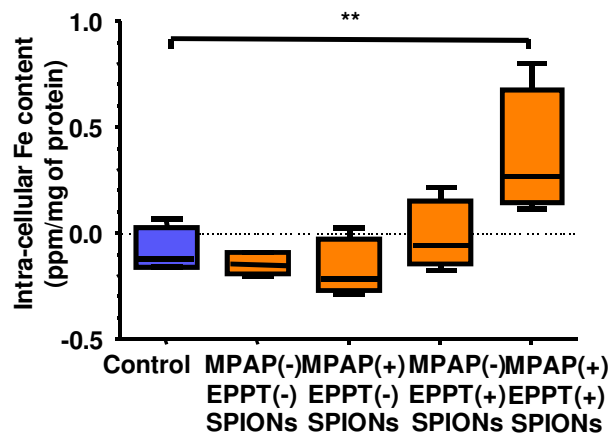


**Figure 34: Intracellular iron concentration in tumors 6 hours after siPLK1-StAv-SPIONs treatment.** \*\*\* $p < 0.001$ , \*\* $p < 0.01$ , \* $p < 0.05$ .

Altogether, these results suggest that there is significant delivery of siPLK1-StAv-SPIONs to the tumor as detected by *in vivo* magnetic resonance imaging.

### 5.5 siPLK1-StAv-SPIONs targeting hinder tumor burden and improves the disease response and overall survival

To address the efficacy of siPLK1-StAv-SPIONs targeting against PLK1, we performed a randomized, placebo controlled study in mice bearing syngenic orthotopic tumors. This involved intravenous injection twice a week for the duration of 4 week (3qD×4 weeks) and animals were recruited to the study 14 days after tumor cells implantation in the pancreas. Studies were performed on separate cohorts to assess end point and intermediate treatment effects and to ascertain overall survival of the treatment.

We found a drastic decrease in the harvested tumor volume after 4 weeks of siPLK1-StAv-SPIONs treatment. Interestingly, siPLK1 and mismatch control treated groups did not show any deviation in tumor volume (**Figure 35**).

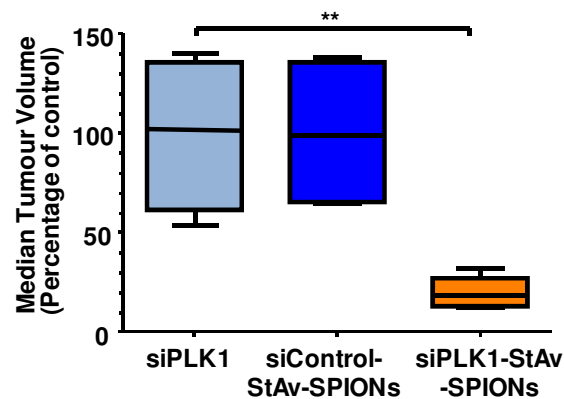


**Figure 35: siPLK1-StAv-SPIONs arrest tumor progression in a syngenic orthotopic tumor model.** Tumor bearing mice were injected intravenously with either siPLK1-StAv-SPIONs, naked siPLK1 or mismatch control siRNA-StAv-SPIONs 14 days after tumor

implantation for 3qD over a time period of four weeks. (a) Median tumor volume after completion of therapy shows significant reduction in tumor volume of siPLK1-StAv-SPIONs treated animals compared to either naked siPLK1 or mismatch-control- siRNA-StAv-SPIONs ( $n = 5$ ). \*\*\* $p < 0.001$ , \*\* $p < 0.01$ , \* $p < 0.05$ .

To monitor the influence of siPLK1-StAv-SPIONs treatment on the tumor growth, we performed magnetic resonance imaging at weekly intervals for 4 weeks and we analysed the tumor growth during the period of treatment. Of note, siPLK1 and siControl-StAv-SPIONs treated group showed no change in tumor growth. In contrast, the siPLK1-StAv-SPIONs treated group showed stagnant tumor growth. Quantitative tumor volume analysis confirmed significant differences in tumor volumes ranging at 28 days and 40 days (**Figure 36a-b**).

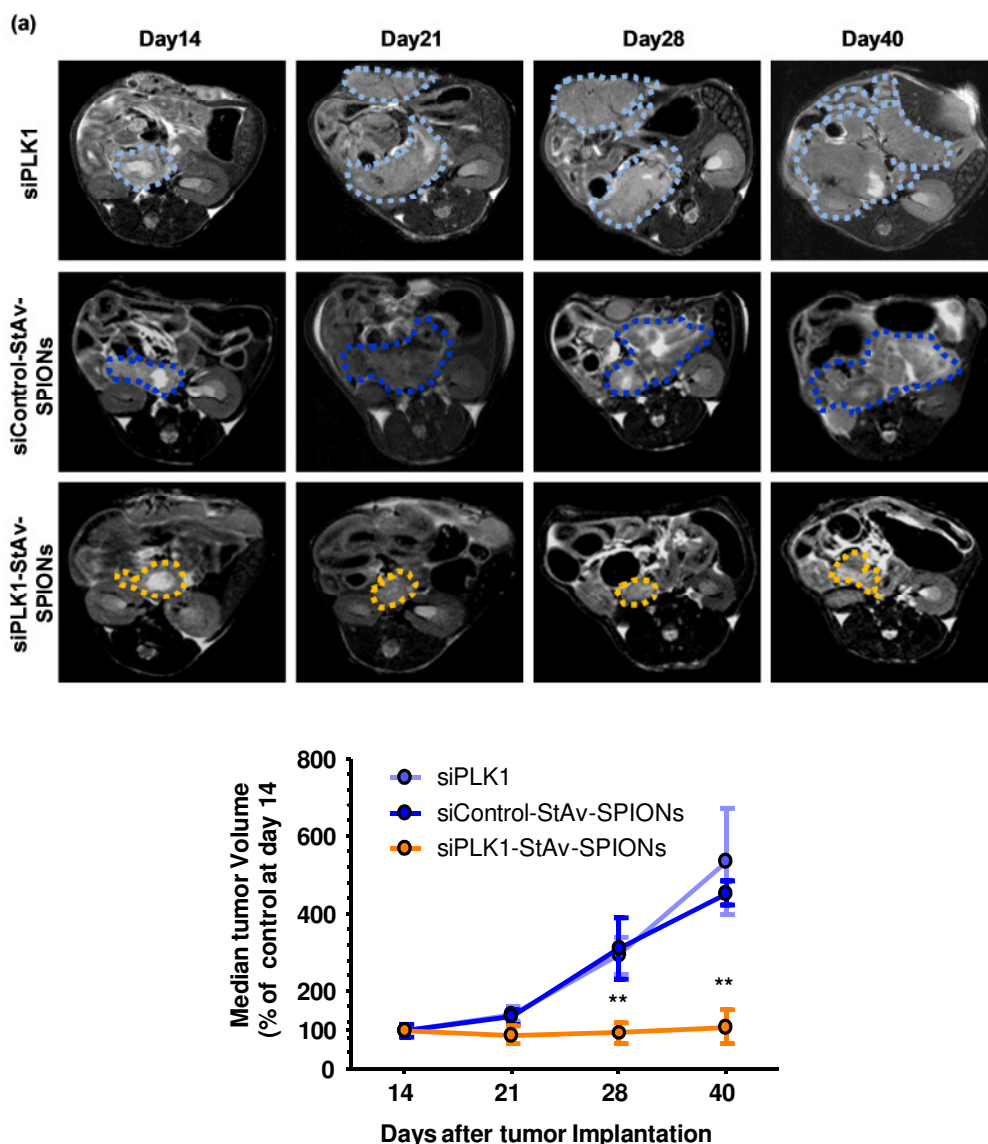


**Figure 36: *In situ* tumor measurement using MRI showed staggancy of tumor growth on siPLK1-StAv-SPIONs treatment.** (a) *In situ* measurement of tumor volume using MRI. Mice bearing a syngenic orthotopic tumor were imaged for tumor volume measurement at 14, 21, 28 and 40 days after siPLK1, siControl-StAv-SPIONs and siPLK1-StAv-SPIONs treatment (twice a week for four weeks) starting at day 14 after tumor implantation. Figures show representative image per time point. (b) *In situ* tumor measurement using MRI showed

stagnancy of tumor growth in the siPLK1-StAv-SPION treated group over the period of treatment. siControl-StAv-SPIONs or naked siPLK1 did not show any effect on tumor volume (n=4). \*\*\*p<0.001, \*\*p<0.01, \*p<0.05.

Immunoblotting of harvested tumors showed significant silencing of siPLK1 in the tumor upon siPLK1-StAv-SPIONs treatments. Quantitative analysis revealed the significant influence of siPLK1-StAv treatment on siPLK1 expression (**Figure 37**). These results prove the fact that siPLK1-StAv-SPIONs are not only available to the tumor but also signify the tumor siPLK1 silencing.

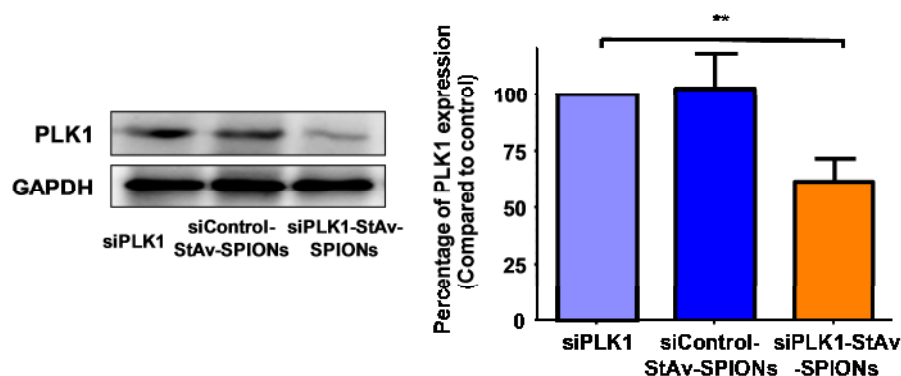


**Figure 37: Immunoblotting of PLK1 revealed a decrease in PLK1 expression the siPLK1-StAv-SPIONs treated group.** Quantification of the expression level showed a significant decrease in PLK1 expression. Data represent mean  $\pm$  SD of three different experiments.

We validated the nonspecific effect of siPLK1-StAv-SPIONs in silencing of siPLK1, through the aid of quantitative real time PCR performed from any different organs harvested after completion of treatment. We any significant down-regulation in siPLK1 RNA expression in organs other than tumors, indicating absence of cytotoxicity instigated by siPLK1-StAv-SPIONs treatment (**Figure 38**).

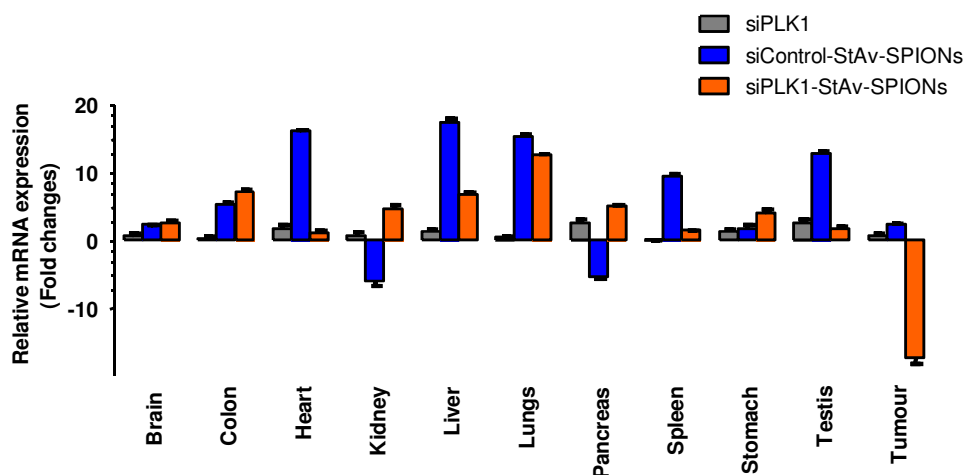


**Figure 38: Differential expression of PLK1 upon siPLK1-StAv-SPIONs treatment.** Total mRNA was isolated from different organs after siPLK1, siControl-StAv-SPIONs and siPLK1-

StAv-SPIONs treatment. plk1 mRNA expression levels were quantified by reverse transcription-polymerase chain reaction. Data are expressed as fold changes with respect to control in mean  $\pm$  SEM (n=3). These data confirm the selective delivery in vivo of siPLK1-StAv-SPIONs to the tumor upon treatment with siPLK1-StAv-SPIONs.

A major apprehension related to siPLK1-StAv-SPIONs treatment was nonspecific silencing of siPLK1 in other organs leading to cellular toxicity. We did not detect any toxicity in siPLK1-StAv-SPIONs treated mice as analysed by serum biological measurement of glucose, creatinine, blood urea nitrogen, bilirubin, alanine aminotransferase and aspartate aminotransferase, when compared to non-treated controls (**Table 9**).

In addition, we did not find accumulation of siPLK1-StAv-SPIONs in pancreas, kidney, liver and tumor as analysed by Perl's iron staining harvested 3 days after final injection. This points to rapid clearance of siPLK1-StAv-SPIONs from the organs and thus better tolerability of siPLK1-StAv-SPIONs (**Figure 39**).

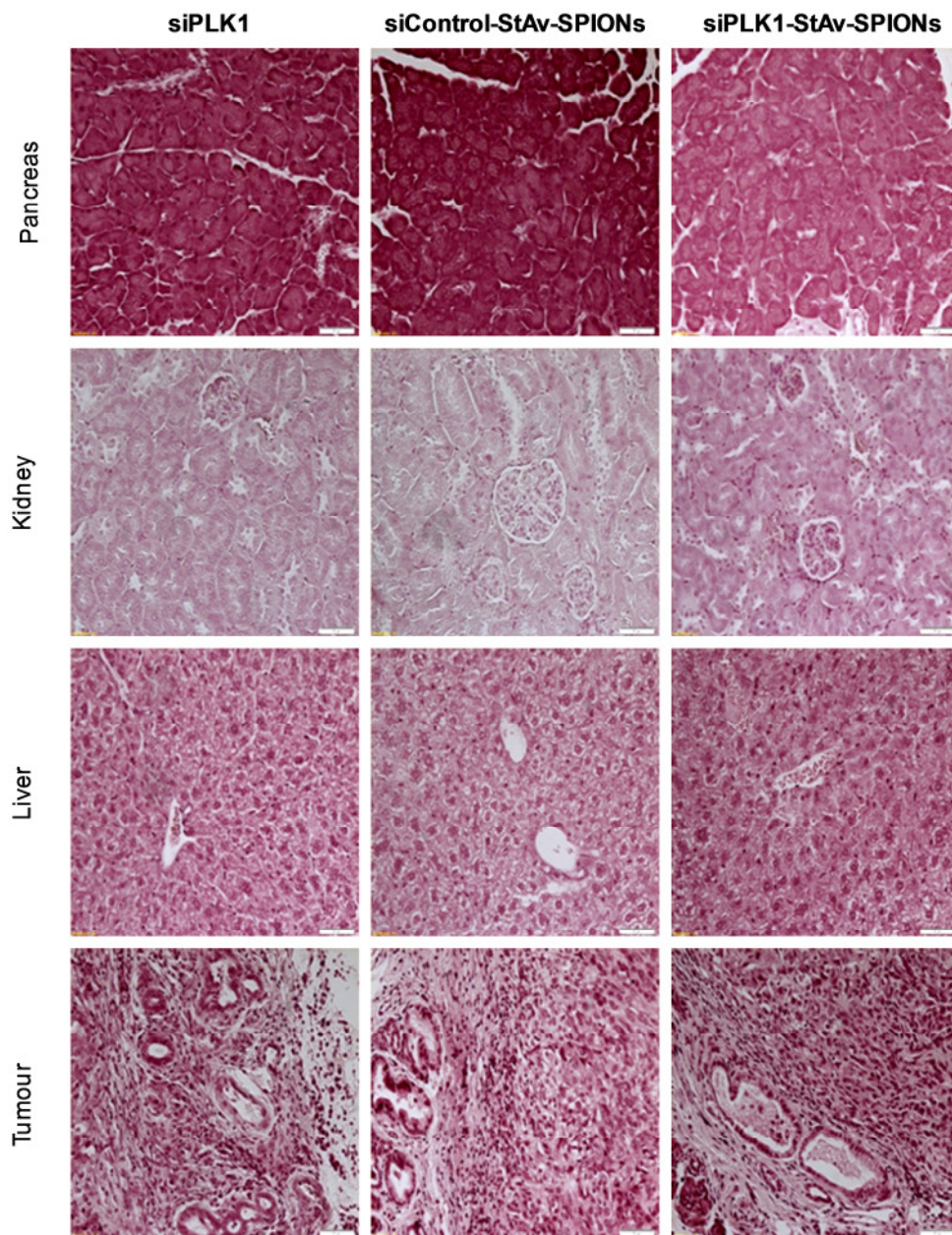


**Figure 39: Perl's Iron staining showing rapid clearance of siPLK1-StAv-SPIONs from tumors, liver and kidney.**

**Table 9: Table showing change in clinical serum parameters on the treatment of siPLK1-StAv-SPIONs in syngenic orthotopic tumor mice. siPLK1-StAv-SPIONs treatment did not show any significant deviation in serum markers corresponding to that of controls. BUN: blood urea nitrogen, AST; Aspartate aminotransferase, ALT: Alanine aminotransferase**

	Units	Reference Values	Control			siPLK1				siControl-StAv-MNPs				siPLK1-StAv-MNPs			
			MEAN	SD	N	MEAN	SD	N	P	MEAN	SD	N	P	MEAN	SD	N	P
Glucose	mmol/l	3.5-9.5	8.23	1.04	4	8.85	1.13	4	0.90	8.30	1.26	4	0.76	8.26	1.80	5	0.40
Creatinine	μmol/l	17-79	12.25	0.50	4	12.25	0.50	4	1.00	13.50	1.00	4	0.28	12.60	0.55	5	0.92
BUN	mmol/l	2.85-11.80	5.03	1.61	4	6.80	0.24	4	<b>0.01</b>	6.13	4.05	4	0.16	6.38	0.95	5	0.34
ALT	μKatal/l	0.02-1.30	0.37	0.27	4	0.84	0.57	4	0.25	0.40	0.25	4	0.89	0.72	0.26	5	0.87
AST	μKatal/l	0.9-4.3	1.73	0.56	4	3.44	3.61	4	<b>0.01</b>	1.62	1.65	4	0.11	2.40	0.57	5	1.00
Bilirubin	μmol/l	0-15	2.03	0.40	4	2.15	0.97	4	0.18	1.75	0.10	4	<b>0.05</b>	1.68	0.15	5	0.08

With these supplementary set of data, we feel convinced that the observed effects of siPLK1-StAv-SPIONs were not the results of cellular toxicity but specific silencing of PLK1 in the tumor.

Having ascertained the viability of our delivery strategy in these proof-of-principle experiments, we sought to characterize the mechanism of reduced tumor burden. We confirmed finding of silencing of PLK1 using immunohistochemistry on siPLK1-StAv-SPIONs treatment. Quantitative analysis revealed the significant reduction in PLK1 expressions corresponding to that of mismatch controls (**Figure 40**).

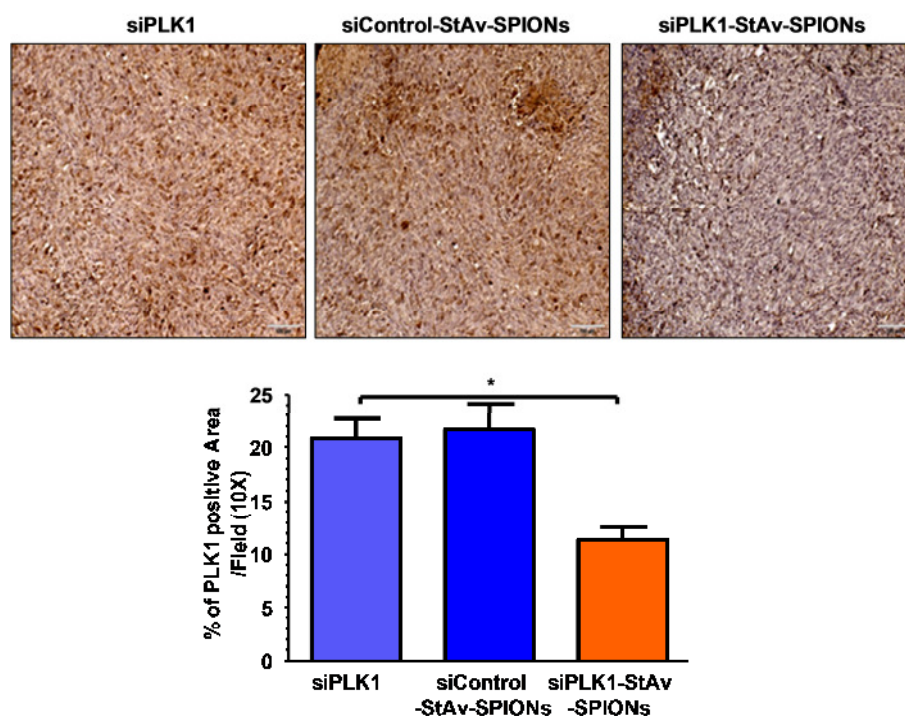


**Figure 40: Influence of siPLK1-StAv-SPIONs treatment on PLK1 expression.** Quantitative analysis of the percentage of PLK1 expression in tumor resection specimen proved a significant decrease in expression of PLK1 in the siPLK1-StAv-SPIONs treated group (n=4-5). \*\*\*p<0.001, \*\*p<0.01, \*p<0.05.

We performed immunohistochemistry for PLK1, the proliferation marker, Ki67 and the neo-angiogenesis marker, CD31. In addition we performed TUNEL assay to determine the efficacy on apoptosis. The silencing effect of PLK1 resulted in a marked decrease in proliferation, quantified by Ki67 positive nuclei in immunohistostaining. Quantitative analysis of Ki67 positive nuclei revealed significant decrease in proliferation in tumors treated with siPLK1-StAv-SPIONs (**Figure 41**).

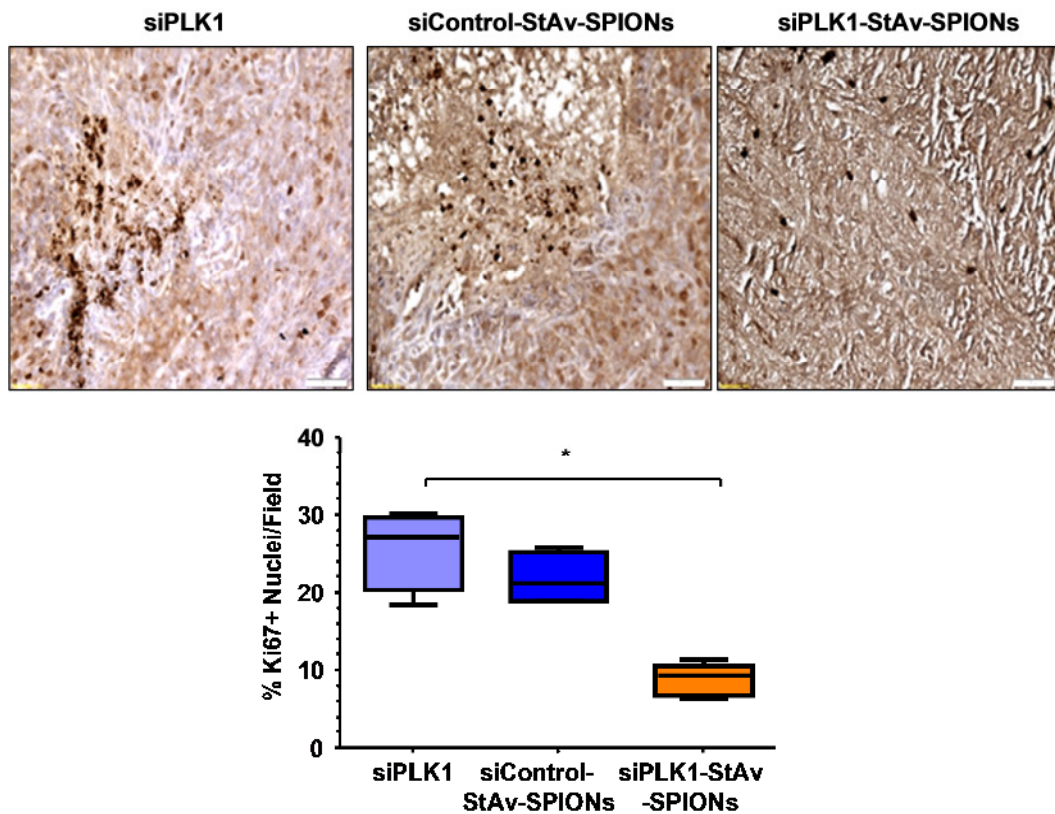


**Figure 41: Immunohistochemistry of Ki67 showing decrease proliferation on siPLK1-StAv-SPIONs.** Quantitative analysis of the percentage of Ki67 positive nuclei in tumor resection specimen proved a significant decrease in proliferation in the siPLK1-StAv-SPIONs treated group (n=5). \*\*\*p<0.001, \*\*p<0.01, \*p<0.05.

This effect was accompanied by marked increase in siPLK1-StAv-SPIONs treatment associated tumor apoptosis measured using TUNEL positive cells corresponding to mismatch controls (**Figure 42**).

To validate these findings, we performed caspase 3 activity measurement using the fluorogenic substrate, R110-DEVD in tumors harvested after the completion of treatment regimen. We validated remarkable increase in caspase 3 activity in tumors treated with siPLK1-StAv-SPIONs, which supports our notion that the tumor siPLK1 silencing leads to a characteristic increase in apoptosis (**Figure 43**).

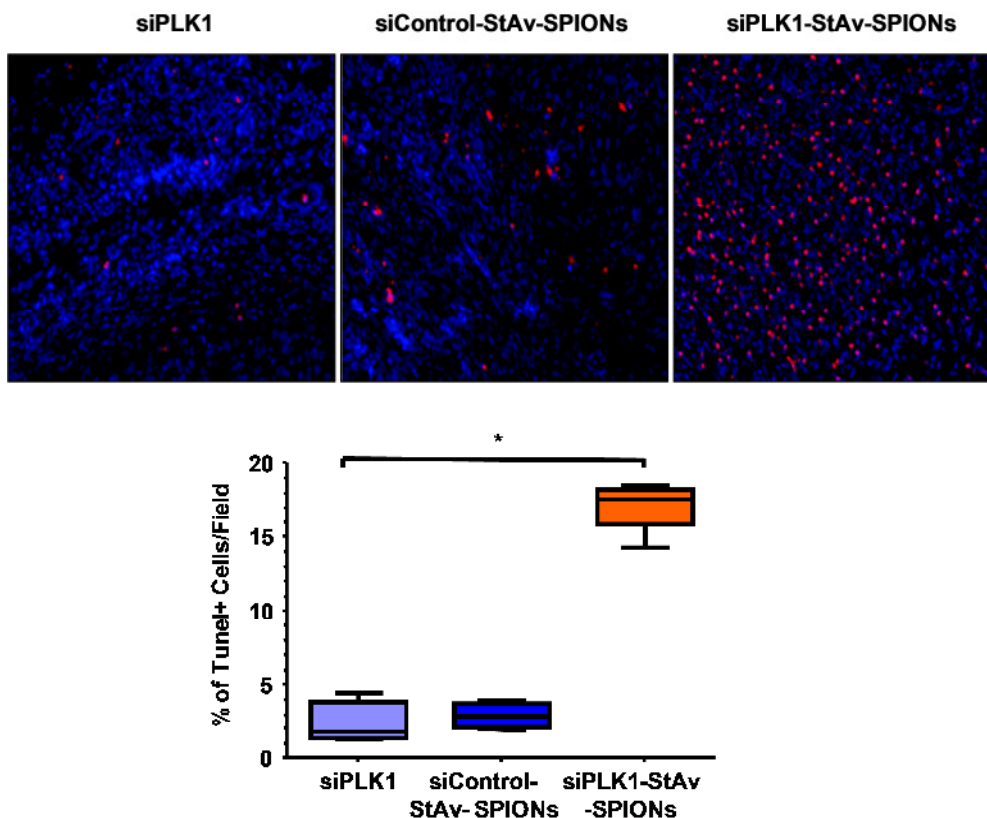


**Figure 42: TUNEL assay showing significant increase in apoptotic nuclei upon siPLK1-StAv-SPIONs treatment.** Quantitative analysis of the percentage of Ki67 positive nuclei in tumor resection specimen proved a significant decrease in proliferation in the siPLK1-StAv-SPION treated group (n=5). \*\*\*p<0.001, \*\*p<0.01, \*p<0.05.

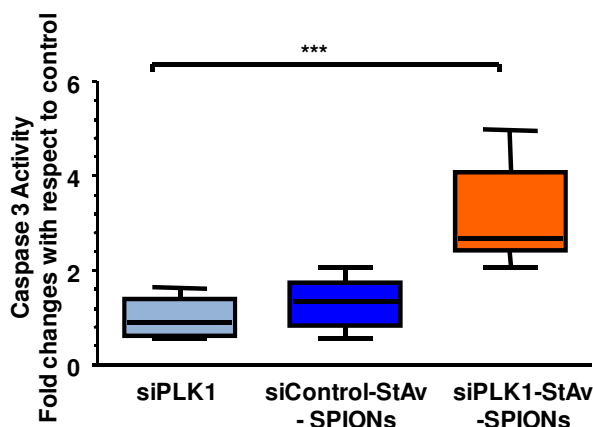


**Figure 43: Influence of siPLK1-StAv-SPIONs treatment on caspase 3 activity.** Caspase 3 activity in tumor tissue of different treatment groups was measured using the fluorogenic substrate R110-DEVD (n= 4-5). \*\*\*p<0.001, \*\*p<0.01, \*p<0.05.

To determine the influence of siPLK1-StAv-SPIONs on angiogenesis in tumors, we performed immunohistochemistry for CD31. siPLK1-StAv-SPIONs did not affect neo-angiogenesis (**Figure 44**).

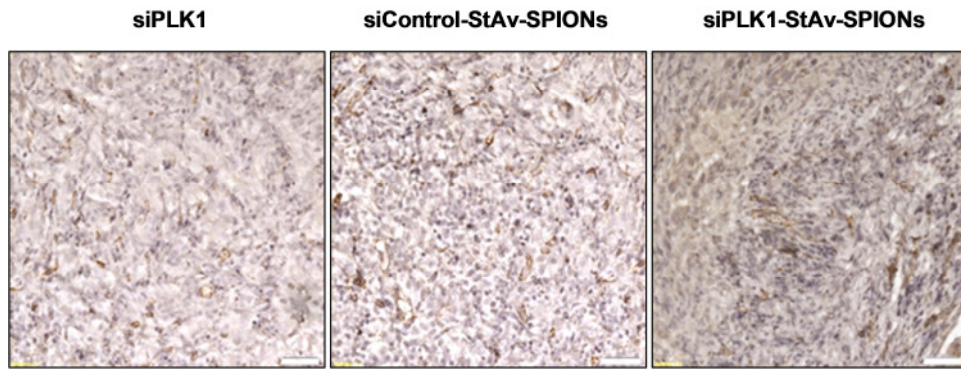


**Figure 44: Influence of siPLK1-StAv-SPIONs treatment on neo-angiogenesis.** Immunohistochemistry of CD31 revealed no change in angiogenesis potential of tumors on siPLK1-StAv-SPIONs.

A major apprehension related to *in vivo* siRNA delivery using nanoparticle systems deals with the induction of type I interferon and inflammatory Cytokines. We performed serum cytokines measurements using micro-CBA kit and found no significant change in levels of cytokines, namely, IL6, IL10, IL12, TNF- $\alpha$ , MCP1 and Interferon- $\gamma$ , suggesting the absence of immunostimulatory properties of the siPLK1-StAv-SPIONs (**Table 10**).

These results underscored the feasibility of siPLK1-StAv-SPIONs as a potential therapeutic strategy.

The aforementioned encouraging results needed ultimate proof for a most clinically significant endpoint, eg. survival. Thus, we performed a prospective, randomized, placebo control trial in mice bearing syngenic orthotopic tumor in pancreas with overall survival as a primary endpoint. We detected an increase in median overall survival to siPLK1-StAv-SPIONs from 76 days in mismatch controls to the 97 days for siPLK1-StAv-SPIONs. Standardized treatment option, gemcitabine revealed a median survival of 96 days similar to that of siPLK1-StAv-SPIONs (**Figure 45**).

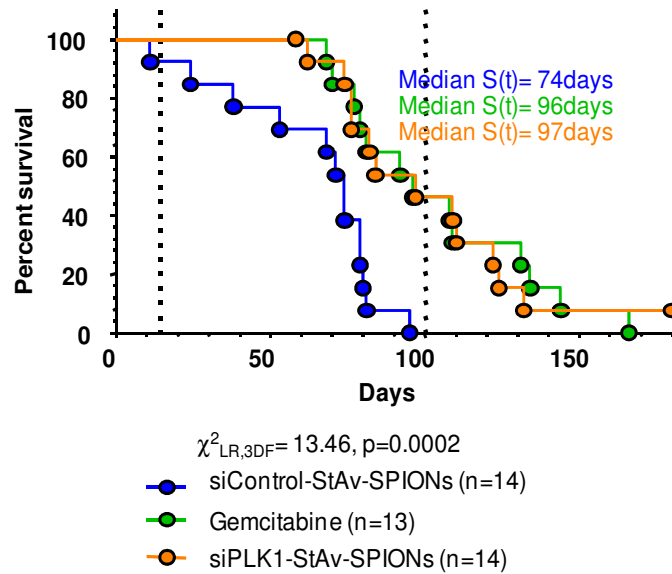


**Figure 45: siPLK1-StAv-SPIONs treatment improves the survival in syngenic orthotopic tumor mouse model.** Kaplan Meier survival analysis from the time of enrollment to treatment with siControl-StAv-SPIONs (n=14), Gemcitabine (n=13) or siPLK1-StAv-SPIONs (n=14). Dotted line window indicates maximum duration of therapy. Median survival time of siPLK1-StAv-SPIONs treatment (96 days) was significantly different to the siControl-StAv-SPIONs treatment (74 days). \*\*\* $p < 0.001$ , \*\*  $p < 0.01$ , \*  $p < 0.05$ .

The tumor burden was significantly diminished on siPLK1-StAv-SPIONs treated tumors over the period of overall survival as shown by tumor growth per day (**Figure 46**).

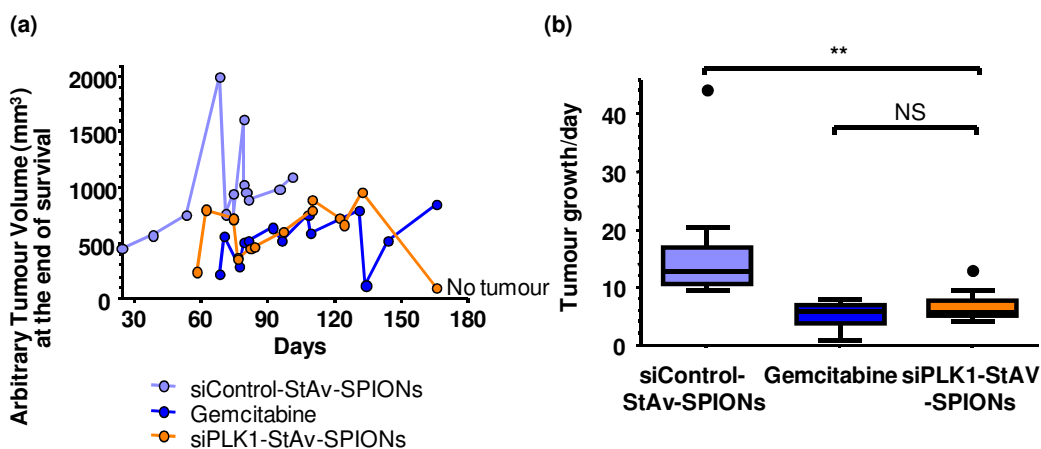


**Figure 46: Diagram illustrating the influence of siPLK1-StAv-SPION treatment on tumor volume over survival duration.** (a) siPLK1-StAv-SPIONs showed lesser tumor burden and increased survival compared to siControl-StAv-SPIONs treatment. (b) siPLK1-StAv-SPIONs showed a delayed tumor growth per day compared to siControl-StAv-SPIONs treatment. \*\*  $p < 0.01$  considered statistically significant (n=13-14).

With these additional results, we feel confident that the observed effects were not the result of cellular toxicity but rather represented gene specific delivery.

**Table 10: Table showing changes in cytokine and chemokines on the treatment of siPLK1-StAv-SPIONs in tumor bearing mice.**  
 siPLK1-StAv-SPIONs treatment did not show any significant deviation in chemokines and cytokines levels corresponding to that of control

Cytokines in pg/ml	Control			siPLK1				siControl-StAv-MNPs				siPLK1-StAv-MNPs			
	MEAN	SD	N	MEAN	SD	N	P	MEAN	SD	N	P	MEAN	SD	N	P
<i>IL12p70</i>	2.92	2.34	4	120.47	183.717	4	0.26	1250.5	2151.59	4	0.06	396.38	600.68	4	<b>0.03</b>
<i>TNF<math>\alpha</math></i>	4.94	3.37	4	10.03	4.43	4	0.11	9.97	12.36	4	1.00	7.47	4.12	4	0.48
<i>IFN<math>\gamma</math></i>	0.36	0.33	4	1.61	0.67	4	<b>0.03</b>	26.53	44.68	4	0.23	4.12	5.58	4	0.13
<i>MCP1</i>	25.22	12.16	4	33.42	6.88	4	0.34	46.13	48.01	4	0.63	28.48	15.98	4	0.89
<i>IL10</i>	2.60	4.51	4	26.09	31.95	4	0.30	391.84	634.87	4	0.11	98.79	158.81	4	0.30
<i>IL6</i>	15.44	14.32	4	160.33	279.49	4	0.85	125.04	213.40	4	1.00	44.69	65.95	4	0.88

### 5.6 siPLK1-StAv-SPIONs represent pharmacokinetic profile suitable for in vivo delivery of siPLK1 to tumor

A major concern related to the in vivo delivery of a metallic nanoparticle delivery system is the rapid clearance of nanoparticles from the body, thus limiting its efficacy owing to a low plasma half-life. In order to determine the pharmacokinetic profiling of siPLK1-StAv-SPIONs, we collected blood 0 min, 3 min, 5 min, 10 min, 30 min, 1 hour, 4 hours and 8 hours after siPLK1-StAv-SPIONs single bolus intravenous injection. We used saline treated animals as a baseline Control. We performed the serum iron quantification using AAS and we obtained a peculiar Iron concentration curve showing a first order kinetics (**Figure 47**).

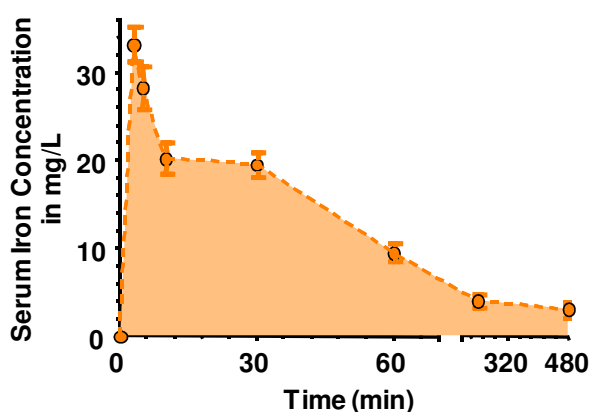


**Figure 47: Time dependent change in serum iron concentration after single dose of siPLK1-StAv-SPIONs.**

The corrected serum iron values when subjected to a non-compartmental first order kinetic model, gave us a serum plasma half-life of siPLK1-StAv-SPIONs of approximately 210 min. Thus, in the array of experimentation to prove the efficacy of the proposed system, pharmacokinetic studies revealed higher bioavailability and higher plasma half-life with significant higher mean plasma mean residual time, thus explaining the fact that siPLK1-StAv-SPIONs were bioavailable exert efficacy. **Table 11** shows the pharmacokinetic profiling following intravenous administration of siPLK1-StAv-SPIONs after its quantification using a non-compartmental modeling.

**Table 11: Table illustrating pharmacokinetic profiling following intravenous administration of siPLK1-StAv-SPIONs. L**

Parameter	Unit	MEAN	SEM	N
Lambda_z	1/min	0.0048	0.00076	5
<b>t1/2</b>	<b>min</b>	<b>208.189</b>	<b>22.559</b>	<b>5</b>
<b>Tmax</b>	<b>min</b>	<b>3.4</b>	<b>0.17889</b>	<b>5</b>
Cmax	mg/L	34.6781	2.07401	5
C0	mg/L	51.6514	6.37048	5
Clast_obs/Cmax		0.11246	0.01686	5
AUC 0-t	mg/L*min	3155.76	210.244	5
AUC 0-inf_obs	mg/L*min	4223.87	283.025	5
AUC 0-t/0-inf_obs		0.76883	0.02655	5
AUMC 0-inf_obs	mg/L*min <sup>2</sup>	1359200	162995	5
<b>MRT 0-inf_obs</b>	<b>min</b>	<b>292.161</b>	<b>32.511</b>	<b>5</b>
Vz_obs	(mg/kg)/(mg/L)	0.18401	0.0141	5
Cl_obs	(mg/kg)/(mg/L)/min	0.00074	8.55E-05	5
vss_obs	(mg/kg)/(mg/L)	0.17465	0.01552	5

Lambda\_z: Terminal elimination rate constant, t1/2: Half-life, Tmax: Time to reach maximum concentration, Cmax: Concentration at Tmax, C0: Concentration without distribution, Clast\_obs/Cmax: Last observed concentration, AUC 0-t: Area under curve from 0 to Clast\_obs, AUC 0-inf\_obs: Area under curve from 0 to infinity, AUC 0-t/0-inf\_obs AUMC 0-inf\_obs: Area under first moment curve, MRT 0-inf\_obs: Mean residual time, Vz\_obs: Volume of distribution at terminal state, Cl\_obs: Total clearance, vss\_obs: Volume of distribution at steady state

### 5.7 siPLK1-StAv-SPIONs though taken up by immune cells, do not influence immunostimulatory effects

One of the major concerns of metallic nanoparticles is of nonspecific uptake by macrophages. We determined changes in proliferation on isolated macrophages after siPLK1-StAv-SPIONs treatment. We found that siPLK1-StAv-SPIONs did not exert any significant deviation on proliferation (**Figure 48**). **Appendix IV** illustrates uptake assay for different subtypes of immune cells 30 min after treatment of siPLK1-StAv-SPIONs.

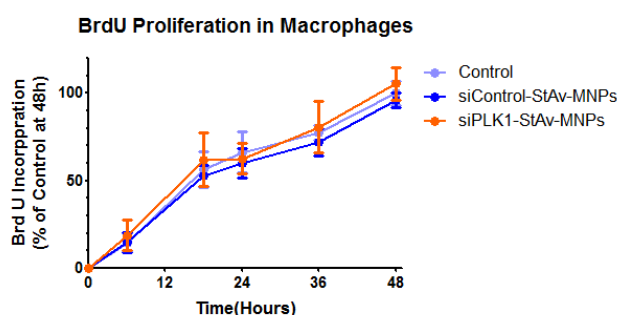


**Figure 48: siPLK1-StAv-SPIONs did not influence the proliferation of macrophages.** BrdU proliferation assay was performed on 48 hours of siPLK1-StAv-SPIONs treatment on macrophages and we observed no significant deviation on the proliferation.

### 5.8 siPLK1-StAv-SPIONs targeting to tumor halt tumor progression KPC mice

The orthotopic syngenic tumor model has been previously criticized for a less developed tumor vasculature and tumor microenvironment compared to an endogenous tumor model. LSL-Kras<sup>G12D</sup>, LSL-Trp53<sup>R172H</sup>, Pdx-1-Cre (KPC) mice, spontaneously develop immunocompetent PDAC that resemble histopathologic and molecular features of human PDAC. This preclinical mouse model is accepted as a model to predict treatment efficacy in patients.

We replicated a prospective, randomized, double blind, placebo control pilot trial in KPC mice to evaluate treatment efficacy of siPLK1-StAv-SPIONs on tumor progression in established tumors. Tumor bearing mice were randomized at the age 16-20 weeks old and were injected intravenously with siPLK1-StAv-SPIONs, StAv-SPIONs or siControl-StAv-SPION for 3qD for two weeks. The investigator was blinded to the treatment. We analysed the tumor growth using ultrasound imaging and found halted growth one week after siPLK1-StAv-SPION treatment whereas control-siRNA-StAv-SPIONs did not reveal any effect (**Figure 49**).

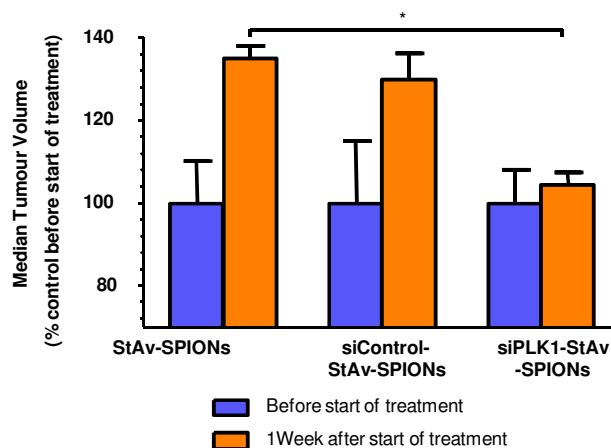


**Figure 49: siPLK1-StAv-SPIONs prevent tumor progression in LSL-Kras<sup>G12D</sup>, LSL-Trp53<sup>R172H</sup>, Pdx-1-Cre (KPC) mice.** Median tumor volume one week after start of therapy showed stagnancy in tumor growth in the siPLK1-StAv-SPIONs treated animals compared to either StAv-SPIONs or siControl-StAv-SPIONs (n = 3-4). *In situ* tumor measurement using ultrasound showed significant stagnancy in tumor growth in siPLK1-StAv-SPION treated group over the period of treatment. siControl-StAv-SPIONs or StAv-SPIONs did not have any effect on tumor volume. \*\* p<0.01, \* p<0.05.

Tumors harvested after two weeks of treatment subjected to immunoblotting and quantitative real time PCR for *PLK1 mRNA* showed significant decrease in *PLK1 mRNA* and protein expression upon treatment with siPLK1-StAv-SPIONs (**Figure 50**).

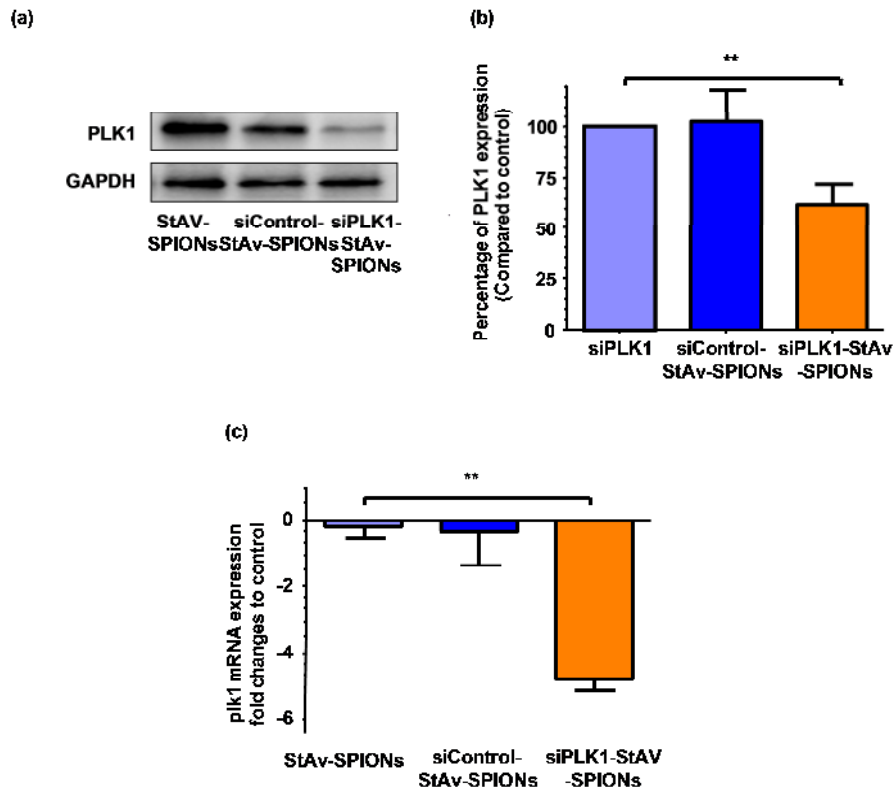


**Figure 50: Quantitative RT-PCR and immunoblotting of PLK1 showed a decrease in PLK1 expression in the siPLK1-StAv-SPIONs treated group.** (a) Immunoblotting showing decrease in PLK1 expression compared to corresponding controls. (b) Quantitative analysis of immunoblotting showed a significant decrease in PLK1 expression in respect to control. Data represent mean  $\pm$  SD (n=3). (c) Quantitative estimation of PLK1 mRNA expression showed significant decrease compared to that of corresponding control. \*\* p<0.01, \* p<0.05.

The underlying mechanism for the change in proliferation of tumor cells showed a decrease in tumor the expression of Ki67. Quantitative assessment of Ki67 immunohistochemistry staining revealed a significant decrease in proliferation upon siPLK1-StAv-SPIONs treatment (Figure 51).

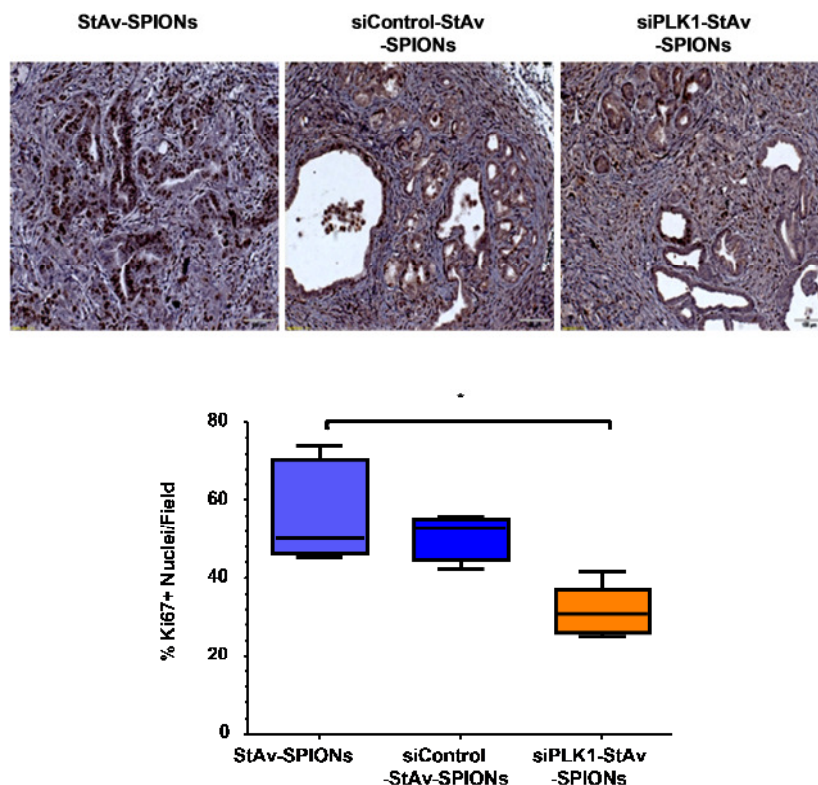


**Figure 51: siPLK1-StAv-SPIONs prevents tumor progression in LSL-Kras<sup>G12D</sup>, LSL-Trp53<sup>R172H</sup>, Pdx-1-Cre (KPC) mice by decreasing proliferation.** Quantitative analysis of the percentage of Ki67 positive nuclei on immunohistochemistry on tumor sections revealed a significant decrease in proliferation in siPLK1-StAv-SPIONs treated animals (n = 4). \*\* p<0.01, \* p<0.05.

Quantitative assessment of Tumor assay revealed a significant increase in apoptosis of tumors treated with sPLK1-StAv-SPIONs (**Figure 52**).

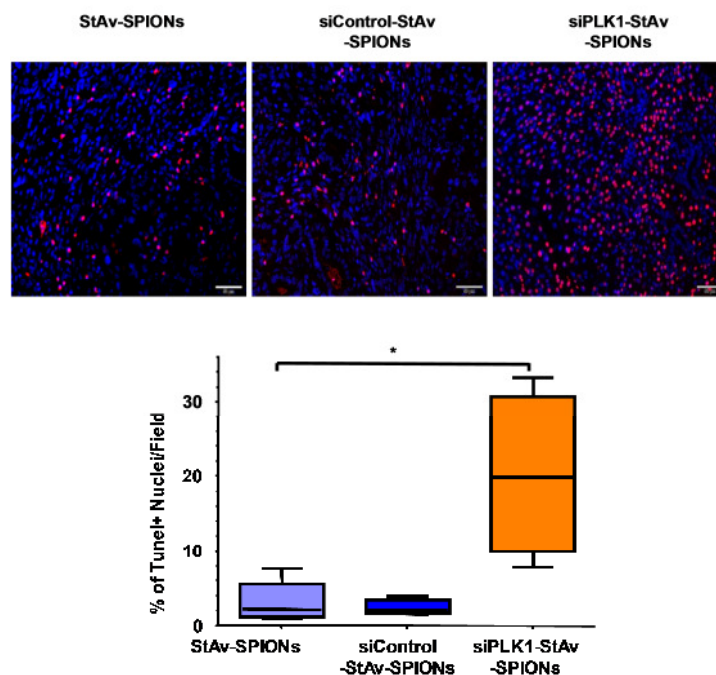


**Figure 52: siPLK1-StAv-SPIONs prevent tumor progression in LSL-Kras<sup>G12D</sup>, LSL-Trp53<sup>R172H</sup>, Pdx-1-Cre (KPC) mice by increasing apoptosis.** Tumor assay showed a

significant increase in apoptotic TUNEL positive cells upon siPLK1-StAv-SPION treatment (n = 4). \*\* p<0.01, \* p<0.05.

Of interest, immunohistochemistry of tumor specimens treated with siPLK1-StAv-SPIONs showed absence of PLK1 expression only in tumor cells, but the surrounding stroma still stained positive for PLK1 proving the specificity of the SPIONs to cancer cells. **(Figure 53)**. The theranostic SPIONs presented in this study have overcome previous experimental and therapeutic limitations.

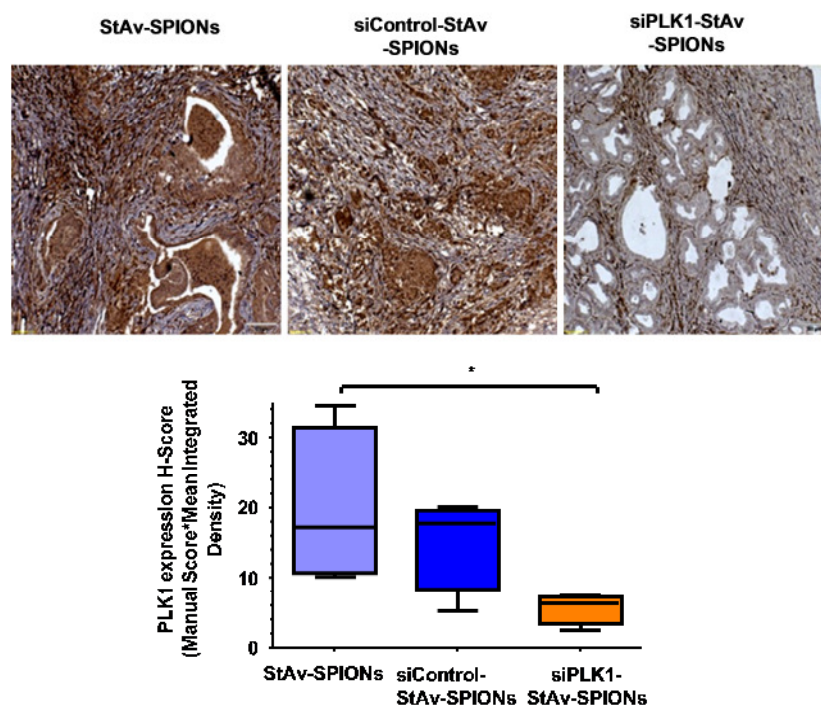


**Figure 53: Change in PLK1 expression in KPC mice upon siPLK1-StAv-SPION treatment.** After 2 weeks of siPLK1-StAv-SPION treatment, tumor showed significant reduced PLK1 expression if compared to controls (n=4). \*\* p<0.01, \* p<0.05.

In conclusion, siPLK1-StAv-SPIONs are specifically delivered to pancreatic ductal adenocarcinoma in a clinical relevant endogenous pancreatic cancer mouse model. siPLK1-StAv-SPIONs show significant treatment efficacy without relevant toxicity and biodistribution can be monitored by MRI. Drug delivery via siPLK1-StAv-SPIONs can therefore overcome systemic dose limitations and are a promising tool for future treatment.

## 6. DISCUSSION

The goal of our study was to design and characterize functional dual purpose SPIONs for noninvasive *in-vivo* imaging as well as siRNA delivery to silencing of PLK1 in PDAC. Our results demonstrate a technology to deliver diagnostics and therapeutics into PDAC using a unique tumor-specific metallic nanoparticle delivery system, siPLK1-StAv-SPIONs. This theranostics application of siPLK1-StAv-SPIONs based on the rationale of non invasive visualization by means of MRI followed by its therapeutic efficacy in reducing tumor burden by selected targeting siRNA the cell cycle regulator, PLK1.

The novel therapeutic approach to target drugs specifically to the tumor cells with effort to minimize the ineffectiveness with traditional chemotherapeutic drugs requires consideration of different sequential approaches such as localisation of drug with its carrier to site of interest, its recognition and interaction with specific tumor cells and its delivery at therapeutic concentration to tumor sites with minimum influence on non-tumor cells. Carrier must be physiologically non-reactive and it must protect drug from degradation. Once it reaches to the site of interest it should not interfere with drug or must not induce unusual toxicity. In order to reduce toxicity, carrier should be biodegradable, inert, non-immunogenic and should not harbor adverse effects to the tumors<sup>8</sup>.

Tumor specific delivery can be achieved either by 'passive targeting' or 'active targeting'. Passive targeting is exploitation of natural distribution of drug carriers *in vivo* by means of increasing permeability of vasculature, increasing retention effects and modulating tumor microenvironment. Active targeting involves alteration of natural disposition pattern of drug carriers, directing it to specific cells by surface antigen or receptor ligand expression, internalization of targeted conjugates<sup>8,9,118</sup>. Although passive targeting approaches form the basis of clinical therapy, they suffer from several limitations. Ubiquitously targeting cells within a tumor is not always feasible because some drugs cannot diffuse efficiently and the random nature of the approach makes it difficult to control the process. This strategy is further limited because certain tumors may not exhibit same vasculature throughout a single tumor. One way to overcome these limitations is to program the carriers so they actively bind to specific cells after extravasation. This binding may be achieved by attaching targeting agents such as ligands, molecules that bind to specific receptors on the cell surface, to the surface of the carrier by a variety of conjugation chemistries. Carriers will recognize and bind to target cells through ligand-receptor interactions, and bound carriers are internalized before the drug is released inside the cell. To maximize specificity, a surface marker (antigen or receptor) should be overexpressed on target cells relative to normal cells<sup>8,9,118,119</sup>.

Most of the particulate carriers fall under 'nanomaterials'. Nanomaterials usually consist of metallic atoms, non-metallic atoms or mixtures of metallic, non-metallic and organic

compounds. The surface of nanomaterials usually coated with biodegradable polymers of biorecognition molecules for improved bioavailability and selectivity. Owing to their properties are similar in scale of two biological molecules, nanomaterials are now being designed to aid transport of diagnostics and therapeutic agents to gain access to site-specific delivery. Nanomaterials have high ratio of surface area to volume as well as tunable optical, electronic, magnetic and biological properties that can be engineered in various size, shapes, chemical composition and morphological shapes. Incorporation of these properties in new generation of drug delivery carriers, contrast agents and diagnostic agents lead to development of novel site-specific delivery<sup>8,9,69,120</sup>. Examples of carriers most commonly used for site-specific delivery design are listed in **Table 12**.

Together with the increased understanding disease pathogenesis, reasons behind therapeutic incompetence to treat solid tumors and advances in tumor-specific delivery carriers suggests the potential for the development of multifunctional nanoparticles that may facilitate the realization of individualized cancer therapy. Suitability of novel site-specific drug carriers as multifunctional nanoparticles that can be applied for simultaneous *in vivo* imaging and treatment of tumor as well as their added advantage over traditional drug delivery (minimum adverse events, tumor specificity and less chemoresistance) provide insight in future drug development.

Colloidal iron oxide nanoparticles have been used in the clinic as MRI contrast agents, mostly for improving the visibility of lesions. Due to their ultra-fine sizes, biocompatibility and superparamagnetic properties, magnetite nanoparticles are emerging as promising candidates for drug delivery and biomedical imaging applications<sup>90</sup>. Although the feasibility of using SPIONs for cancer detection and drug delivery has been demonstrated<sup>11</sup>, a major obstacle limiting their clinical application is that non-targeted nanoparticles are unable to reach sufficient concentrations in the tumor site to either produce a strong signal for tumor imaging or to carry optimal amounts of therapeutic agents into tumor cells. One approach to overcome this problem is to develop tumor targeted SPIONs that are highly sensitive imaging probes and/or are capable of conjugating large amounts of therapeutic agents. Several multifunctional SPIONs have been evaluated preclinical setup to-date considering multimodal and multifunctionality, ease of surface modification and biocompatibility of SPIONs, are listed in **Table 13**<sup>121,122</sup>.

For engineering SPIONs, different ligands such as antibodies, peptides and small molecules targeting receptor specific to the tumor cells and are highly expressed in tumors, are conjugated with SPIONs. Increasing evidence shows that the selective delivery of therapeutic agents into a tumor mass may minimize toxicity to normal tissues and improve bioavailability of cytotoxic agents. However, there are still many obstacles for successful

tumor-targeted SPIONs as theranostics *in vivo*, because of functional group modification of the drugs during conjugation may change their chemical properties, rendering it ineffective, lower drug loading efficiency to exploit pharmacological efficacy, release of conjugated or encapsulated drugs from SPIONs in the blood before entering into tumor mass, nonspecific uptake by macrophages and release of drug in lysosomes but not in cytoplasm within targeting cells, embedding part of the ligand binding site in SPIONs may decrease the targeting ability, and loss in magnetization of the core magnetic material during multistep chemical reaction<sup>121-125</sup>.

The recent past has observed considerable progress in the way human tumors are characterized with a particular gain in knowledge of cancer at the molecular level. This has resulted in a shift toward using molecularly targeted therapies for cancer, necessitating the development of corresponding molecular tools to determine which patients are most likely to benefit from particular therapies<sup>126</sup>. Consequently, the capacity to noninvasively assess tumor anatomy and physiology is essential for early diagnosis and effective treatment<sup>99,105,127</sup>.

The crucial properties of PDAC are the affinity for metastatic spread and a notorious resistance to traditional chemotherapies. These features in turn establish the major hurdles to meaningful treatment of the disease. A characteristic feature of this treatment failure is inability of traditional chemotherapies to reach the site of action. An unexpected, but critically important, barrier to systemic therapy is a profoundly diminished functional vasculature in PDAC. Primary mechanism limiting perfusion in PDAC is a significant collapse of resident vessels by inordinately high fluid pressures in interstitium impeding cytotoxic drug delivery to the tumor<sup>113,128,129</sup>.

The theory directing the movement of fluid and solute across a semi-permeable membrane dividing two compartments is derived from fundamental thermodynamic principles and integrates hydrostatic and osmotic pressure gradients as the primary source of fluid flow, and concentration gradients as the driving force for solute flux. This explains the inability of effective chemotherapy concentrations in PDAC owing to high interstitial fluid pressures. This assumption predict contingency of the intravascular and interstitial compartments suggesting that changes in high fluid pressures in interstitium is direct reflection of intratumoral vascular pressures largely as a consequence of leaky vasculature<sup>128,130</sup>. The basis of using SPIONs for theranostics is justified by their proven properties of ultra-fine sizes, biocompatibility, hydrophilicity to avoid nonspecific uptake by RES and aggregation, superparamagnetic properties and by their proven accumulation in tumors resulting from enhanced permeability and retention effect associated with leaky vasculature and by increased endocytosis by actively proliferating tumor cells<sup>90,131-133</sup>.

The tumor directed accumulation is further substantiated using tumor specific peptides conjugated to siPLK1-StAv-SPIONs. The synthesized multimodal probe demonstrated specificity toward an uMUC1 overexpressed on the tumor surface owing to the peptide ligand EPPT1. The uMUC1 specific siPLK1-StAv-SPIONs probe introduced here can significantly advance our current ability to detect PDAC as well as tumor metastases because the targeted antigen is also ubiquitously expressed on metastasizing cancer cells<sup>100,134</sup>. Therapeutic strategies implying siRNA are unique because they would involve the modular design of RNA duplexes capable of mediating phenotypic reprogramming over a broad range of disease applications. The interest in developing siRNA into a therapeutic modality has engendered a variety of ideas and approaches that have as their final goal the transformation of the siRNA duplexes into a molecular drug. Several of these approaches are undergoing clinical trials<sup>135</sup>. Therapeutic efficacy of siPLK1-StAv-SPIONs is demonstrated using siPLK1 conjugation to SPIONs targeted against the cell cycle regulator, PLK1. siPLK1 duplex, conjugated to SPIONs by means of streptavidin-Biotin interaction, remains tethered to SPIONs without compromising its silencing efficiency. Our *in-silico* data showed the binding efficiency of biotinylated-siPLK1 to streptavidin. Furthermore, previous results suggest that covalent conjugation of siPLK1 to SPIONs does not comprise silencing<sup>104,131</sup>. In fact, the presence of a siRNA carrier preserved biological activity and enhances stability<sup>136</sup>. Further conjugation with the cell membrane peptide, MPAP peptide was used in order to increase the electrostatic interactions through the positively charged arginine motives and their hydrophobic interaction leading to direct translocation through the negatively charged glycocalyx. On the other hand, it has been described that the addition of a myristoylated group can facilitate the insertion of peptides, proteins and other cargoes into a lipid bilayer due to direct hydrophobic interaction, allowing the translocation of both positively and negatively charged peptides and their cargoes throughout the lipid bilayer of plasma membrane either by endocytic or energy-independent mechanisms<sup>101,104,131,137,138</sup>. Our delivery strategy allowed us to achieve substantial silencing of PLK1 overexpressed during the progression of PDAC.

Table 12: Most commonly used site specific delivery carriers

Carriers	Structure/Description	Characteristics/Functions	References
<b>Biological macromolecular ligands</b>			
Antibodies	Human antibodies, humanized antibodies, chimeric antibodies or smaller fragments of antibodies (F <sub>ab</sub> fragments) targeted for cell specific antigens	Engineered with altered properties, such as antigen-binding affinity, molecular architecture and homodimerization state to enhance their tumor targeting and potency, very high selectivity, can be conjugated with nanoparticles to improve potency	118,139,140
Viral-based nanoparticles	Nanoassembled structures in which virus protein cages, which are multivalent, self-assembled structures are used for geometric shape, well characterized surface properties and nanoscale dimensions	Fusogenic cell receptor-binding properties, high transfection efficiency, Large number of molecules can be presented in context of defined environment with control over spacing and orientation, multivalency, monodisperse size, better characterized, Biological compatibility, inert, tumor specificity	9,141-143
Nucleic acid based carriers	Nucleic acid based carriers, Aptamers, are single-stranded oligonucleotide short sequences with intermolecular Watson Crick interactions, contributes to unique conformational structure	Stable, high target affinity, Low immunogenicity, can be easily synthesized and reproducible, cost-effective, manageable via modifications for improving pharmacokinetics and resistance to biodegradation, cell specific	74,139,144,145
Protein-based carriers	Oligopeptides differentiated from their larger counterparts by having sequences limited to less than about 50 residues and having simple three dimensional confirmation, peptides-chimeras	Attractive alternative to antibodies, small size, low immunogenicity, higher stability and ease of manufacture, specificity of delivery, high biostability	139,146,147
<b>Nanomaterials</b>			
<b>Polymer-based carriers</b>			
Polymeric micelle	Consists of two spherical concentric regions, a densely packed core of hydrophobic polymeric blocks and a shell of dense brush of poly(ethylene oxide)	Suitable carrier for hydrophobic drugs, Biocompatible, self-assembling in core shell structure, Biodegradable, Ease of functional modification, high targeting potential, control release potential, lengthy retention time	9,76,148
Dendrimers	Unique hyper-branched repeated sequenced polymeric macromolecules, resulting in a nearly perfect three dimensional geometric pattern	monodisperse size, modifiable surface functionality, multivalency, water solubility, and available internal cavity make them attractive for drug delivery, internal void space helps for encapsulation, low	9,149-151

Carriers	Structure/Description	Characteristics/Functions	References
		immunoreactivity	
Liposome	Consists of colloidal solution of amphiphilic molecules that self-assemble in water, composed of lipid bilayers and have a spherical shape in which an outer lipid bilayer surrounds a central aqueous space	Biocompatibility, Biodegradability, flexibility of size and surface manipulations (stealth liposomes), biologically inert, low cytotoxicity, can provide sustained release of drug, low immunoreactivity	9,79,80,94,152
<b><i>Metallic carriers</i></b>			
Iron oxide nanoparticles	Superparamagnetic iron oxide core (SPIONs) consisting of colloidal, magnetite cubic inverse spinel tetrahedral nanocrystals, surrounded by different biocompatible coating; Ferrofluids	Exhibits superparamagnetic phenomenon and quantum tunneling of magnetization, unique mesoscopic physical, chemical, thermal and mechanical properties, biocompatible and nonanaphylactic, Easily engineered for surface modification for bioconjugation and biomodification, can be used for cell imaging, MRI imaging, hyperthermia, drug delivery, magnetofections etc.	87,122,153-156
Gold nanoparticles	Noble, chiral, colloidal gold nanoparticles	High surface-plasmon resonance absorption; photodynamic therapy, tunable optical properties, non-immunogenic and non-cytotoxic, Facilitate bioconjugation and biomodification	119,123,157-159
Silica nanoparticles	Mesoporous silica nanoparticles functionalized by surface hyper-branching polymers	Multifunctionality, Tunable porosity at nanometer scale, high loading capacity, Can be engineered for specific cell recognition	160-162
Nanoshells	Dielectric core nanoparticles surrounded by ultrathin metal shells with tunable plasmon resonance	High scattering optical cross sections; contrast agent of optical coherence imaging, Can be engineered to monitor particular wavelength which aid in dual imaging and therapy option, photodynamic therapy	163-165
Quantum dots	2-100nm sized semiconductor metalloids nanocrystals	Biocompatible, can be easily conjugated with biorecognition molecules, fluorescence imaging, photosensitizes, photodynamic therapy	118,166-168

Carriers	Structure/Description	Characteristics/Functions	References
Fullerenes	Bucky-balls, buckminsterfullerenes. Consists of sixty carbon atoms arranged in soccer ball structures	Biocompatible and non-toxic, owing to condensed aromatic rings; significant absorption of visible light, useful for photodynamic therapy, Convenient three dimensional scaffolding for covalent attachment of multiple drugs	120,169-171

**Table 13: Different types of multifunctional SPIONs for cancer theranostics (Table adopted from Xiang-Hong Peng *et al*, 2008)**

SPIONs	Target	targeting ligands	Tumors
USPIONs	Surface antigen	Monoclonal antibody-610	Colon carcinoma cell-lines
SPIONs	Carcinoembryonic antigen (CEA)	Antibody to CEA	Colon tumors
MIONs	Surface antigen	Monoclonal antibody-L6	Intracranial tumor LX-1
USPIONs	Transferrin receptor	Transferrin	Mammary carcinoma
Streptavidin Conjugated SPIONs	Her-2/neu receptor	Monoclonal antibody-Her/Neu	Breast cancer
CLIONs-NH <sub>2</sub>	underglycosylated mucin-1 antigen (uMUC1)	EPPT peptide	Breast, colon, pancreas and lung cancer cell-lines
Dextran coated magnetite SPIONs	Folate receptor	Folic acid	human epithelial carcinoma cell lines
Ferumoxides	Colorectal tumor antigen	Monoclonal antibody A7	Colorectal carcinoma
SPIONS	Her-2/neu receptor	Herceptin	NIH3T36.7
SPIONS	Folate receptor	Methotrexate	Human cervical cancer cell-lines
PEG-SPIONS	Folate receptor	Folic acid	Human cervical cancer cell-lines
SPIONs	membrane bound matrix metalloproteases 2	Chorotoxin peptides	Rat-Glioma cell-lines

<b>SPIONs</b>	<b>Target</b>	<b>targeting ligands</b>	<b>Tumors</b>
SPIONs conjugated with photodynamic agents	surface localized tumor vasculature	F3 peptide	Rat glioma
HFn-IO	$\alpha_v\beta_3$ integrins	RGD4C	Melanoma cell-lines
SPIONs	LHRH receptor	Luteinizing hormone releasing hormone (LHRH)	Breast cancer
SPIONs	Clotted plasma	CREKA peptide	Breast cancer
USPIONs	$\alpha_v\beta_3$ integrins	Arg-Gly-Asp (RGD)	Human epidermoid carcinoma
PEG-SPIONs	Folate receptor	Folic acid	Human epithelial mouth carcinoma
Streptavidin Conjugated SPIONs	PSMA	Antibody to Prostate specific membrane antigen (PSMA)	Human prostate cancer cells
Magnetism-engineered SPIONs	Her-2/neu receptor	Herceptin	NIH3T36.7
PEG-SPIONs	membrane bound matrix metalloproteases 2	Chorotoxin	Rat glioma

Triple labeled siPLK1-StAv-SPIONs delivery platform has been characterized for its composition, physical, physiochemical properties influenced delivery of siPLK1. siPLK1-StAv-SPIONs physical characterization demonstrated typical cubic spinel inverse crystal magnetite units with the core diameter of SPIONs being 10 nm. The hydrodynamic diameter was in range of 110-150nm which signifies endocytosis as possible mechanism for the intracellular uptake<sup>172</sup>. siPLK1-StAv-SPIONs showed dense surface morphology as evaluated by AFM. The conjugation of PLK1 targeting complex, siPLK1-StAv-SPIONs, resulted in triple-labeled nanoparticles consisting of approximately 5 siPLK1 molecules per siPLK1-StAv-SPION. *In silico* docking of biotinylated siPLK1 with streptavidin with the concern of availability of siPLK1 to the surface of StAv-SPIONs, showed siPLK1 is always outside of the streptavidin and not getting entrapped in coating. Evaluation of physical and physiochemical properties of siPLK1-StAv-SPIONs provided us well characterized and highly reproducible functional probes for selective targeting of PLK1 in PDAC.

Pancreatic cancer cell-line, 6606PDA, derived from a murine endogenous PDAC mouse model (KPC mouse), were used for evaluation of *in-vitro* properties owing to their characteristic properties of mimicking human tumor cells. Our *in-vitro* study summarized efficient initiation of PLK1 silencing by mean of specific targeting by siPLK1 duplex. We sought to analyze the uptake of the siPLK1-StAv-SPIONs in tumor cells and we found the significant increase in intracellular iron concentration reflecting increased uptake of siPLK1-StAv-SPIONs by the cells. Our study was originally based on the ability of PLK1 suppression to hinder tumor proliferation by arresting the cells in G2/M phase of mitosis<sup>173-175</sup>. On siPLK1-StAv-SPIONs treatments, cytometric analysis revealed pronounced increase in the number of cells in the G2/M phase. To confirm the silencing efficacy of siPLK1-StAv-SPIONs, we found apparent suppression in proliferation of 6606PDA cells. siPLK1-StAv-SPIONs showed better tolerance and generated less reactive oxygen species. Our delivery strategy allowed us to achieve substantial silencing in tumors. This silencing effect and in turns its therapeutic intervention reduced tumor proliferation comparable or superior to previously published results<sup>7</sup>.

We subsequently assessed the uptake specificity and possible uptake mechanism of siPLK1-StAv-SPIONs. We found evident uptake of MPAP (+) EPPT1 (+) siPLK1-StAv-SPIONs in cancer cells. MUC1 blocking showed a concentration dependent decrease in the uptake of siPLK1-StAv-SPIONs, revealing the uptake of siPLK1-StAv-SPIONs to be dependent on EPPT1 and MPAP. The specificity for tumor cells uptake is mediated by MUC1 selective anchorage driven by EPPT1.

To assess the possible functional mechanism of uptake in cells, we hypothesized endocytosis as the possible mechanism for the uptake considering the size, particle charge

and physical characteristics which determined the chances of passive diffusion or active transport<sup>86,176-180</sup>. To further validate this notion, pretreatment with a clathrin dependent endocytosis inhibitor, Dynasore<sup>181</sup> abated siPLK1-StAv-SPIONs uptake. This data support the conception that uptake of siPLK1-StAv-SPIONs explicit to the tumor cells is driven by clathrin mediated endocytosis.

siPLK1-StAv-SPIONs showed partial colocalization with early endosomal marker, EEA1 over a period of 30 minutes confirming the endosomal uptake of siPLK1-StAv-SPIONs. We suggest that siPLK1-StAv-SPIONs are specifically endocytosized in tumor cells by clathrin dependent endocytosis mechanism and remain in the endosomes. In order to achieve successful gene silencing, siRNA must interact with RNA-induced silencing complex (RISC) to induce RNA silencing. If siRNA cannot escape from the endosomal compartment, there would be too less siRNA to the cytosol to interact with RNA-induced silencing complex (RISC). Perinuclear localization of siRNA enhances the potential to interact with RNA-induced silencing complex (RISC). However, most of these delivery approaches are not optimized to enable intracellular trafficking of the siRNAs into the cytoplasm where they must associate with the RNA-induced silencing complex (RISC) to direct the cleavage of mRNAs bearing complementary binding sites. In particular, the trafficking of siRNAs from endosomes into the cytoplasm represents a major rate-limiting step for many delivery approaches. These observations prompted us to further examine in transmission electron microscopy whether siPLK1-StAv-SPIONs are taken up by the cells. Endosomal colocalization of siPLK1-StAv-SPIONs at early time point and more frequent cytoplasmic localisation during later time point was directed and proved endosomal escape. Different mechanisms such as pore formation in the endosomal membrane, proton sponge effect of protonable groups and fusion into the lipid bilayer of endosomes have been proposed to facilitate the endosomal escape. Unsaturated amino groups of MPAP drive the proton sponge effect by sequestering proton pumps on endosomes and rupturing endosomes (**Figure 54**). The proton sponge effect is mediated by agents with a high buffering capacity and the flexibility to swell when protonated. Protonation induces an extensive inflow of ions and water into the endosomal environment which subsequently leads to rupture of the endosomal membrane and release of the entrapped components. Tertiary amine groups that contain a hydrophobic chain e.g. MPAP, have been shown to accumulate in endosomes which have an acidic pH and protonated resulting in leading to an increase in osmotic pressure in the endosomes that results in disruption of the endosomal membrane<sup>9,86,182-189</sup>.

Our study introduces MRI imaging of tumor for tracking siPLK1-StAv-SPIONs. These particles because of small crystal size possess a large ferrimagnetic moment that in turn is free to align with an applied magnetic field and possess predominant proton relaxation rates

of the surrounding water proton spins which is associated with the magnetic susceptibility of the particles leading to  $T_2$  relaxation. The aligned magnetization then creates microscopic field gradients that dephase nearby protons and enhance the  $T_2$  NMR relaxation rate giving rise to signal reduction on  $T_2$  weighted images, over and beyond the usual dipole-dipole relaxation mechanism that affect both  $T_2$  and  $T_1$  relaxation time<sup>190-192</sup>.

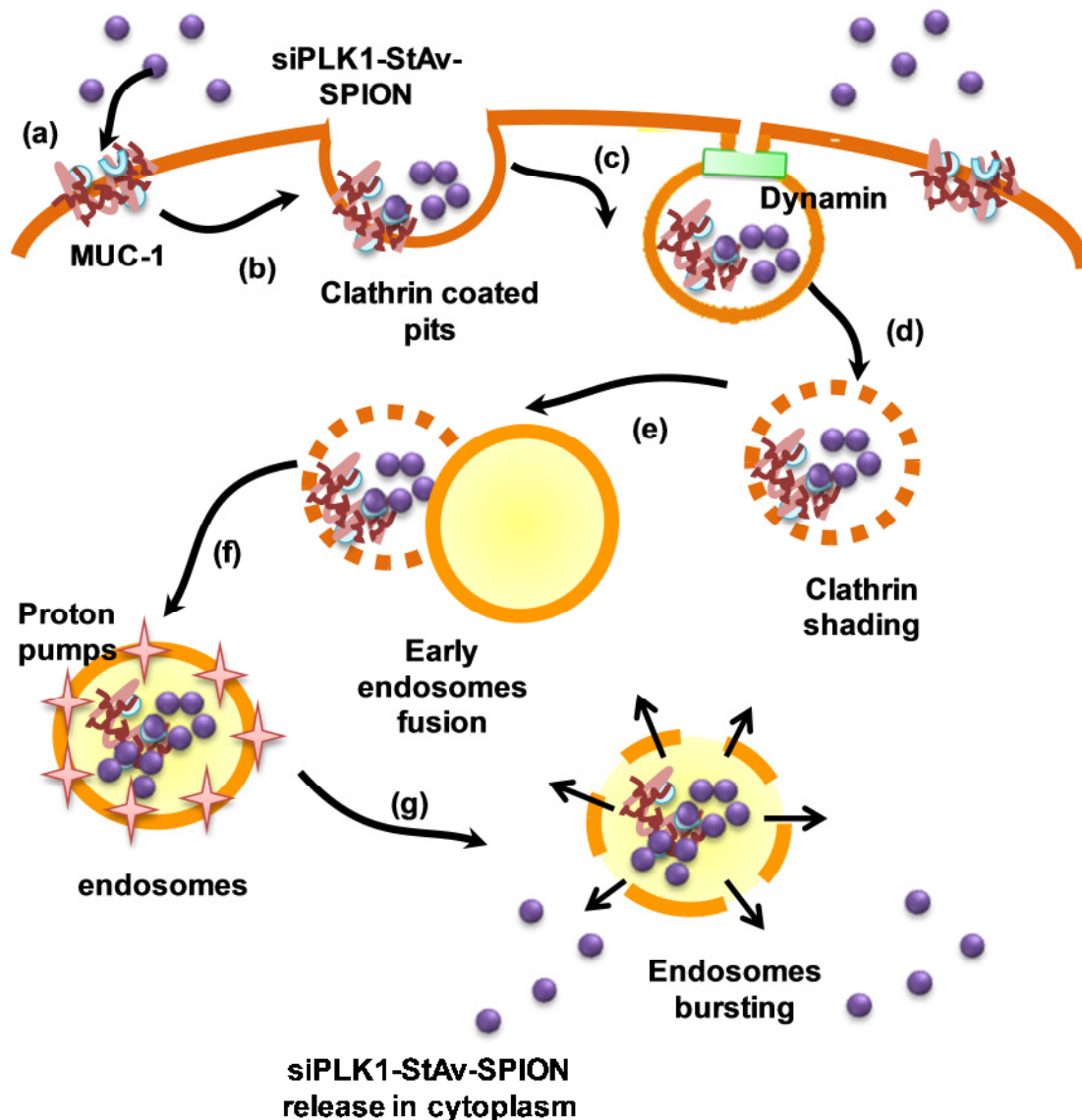


**Figure 54: Uptake and release mechanism of siPLK1-StAv-SPIONs.** (a) siPLK1-StAv-SPIONs bind selectively to MUC1 expressing cells through the aid of EPPT1 and MPAP. (b) The cells start forming clathrin coated pits along the siPLK1-StAv-SPIONs. (c) These pits undergo scission, which is mediated by Dynamin. (d) The formed vesicles get internalized, where clathrin is shaded. (e-f) Clathrin shaded vesicles fuse with early endosomes to form endosomes. (g) Inside endosomes unsaturated amino acid groups from MPAP sequester protons through proton pumps. This builds an osmotic pressure inside the endosomes resulting in the membrane rupture of endosomes and the release of siPLK1-StAv-SPIONs into the cytoplasm. Here the siRNA can work via the RISC complex.

As per our anticipation, siPLK1-StAv-SPIONs after 2 hours treatment showed significant diminution in  $T_2$  relaxivity as evident by a decrease in contrast in tumors. The effectiveness of

a contrast agent can be described by its relaxivity, which is the proportionality constant of the measured rate of relaxation, or  $R_1$  ( $1/T_1$ ) and  $R_2$  ( $1/T_2$ ), over a range of SPIONs concentrations. We further validated the accumulation of the siPLK1-StAv-SPIONs in tumor using quantitative analysis for iron overload calculated using  $R_2^*$  single peak fat corrected echo images<sup>155</sup>.  $R_2^*$  value over  $100s^{-1}$  were considered to be a surfeit of iron in the tissue. siPLK1-StAv-SPIONs treated animals showed a significant increment in  $R_2$  values compared to control. The added value in combining the siRNA delivery and imaging capabilities within a single nanoparticle module allows to monitor noninvasively and quantitatively the bioavailability of the therapeutic agent. Using our approach, we can directly correlate the delivery with the time course and abundance of a therapeutic molecule or potentially identify new transcriptional targets, associated with enhanced graft survival, from a better-informed perspective. Moreover, MRI serves the dual purpose of reporting on the relative accumulation of the siPLK1-StAv-SPIONs in tumor tissue and quantifying the change in tumor volume over the course of treatment, as an indicator of therapeutic response<sup>101,104,110,127,138</sup>. With these studies, we establish the feasibility of nanoparticle-based image-tagged siRNA delivery to PDAC.

Target silencing by siPLK1 may offer several advantages over functional inhibition by small-molecule inhibitors. By its nature, siRNAs is highly specific and allows for the selective inhibition of closely related proteins compared with the relative promiscuity of kinase inhibitors. Current PLK1 inhibitors, for example, also inhibit PLK2 and PLK3 kinase activity, raising some concern that concomitant inhibition of these family members may have opposing effects in controlling cell division<sup>193</sup>. The biological response to protein depletion by siPLK1 can also differ from its functional inhibition by small molecules, in loss of both kinase and polo-box functionality upon PLK1 gene silencing. The duration of drug effect with minimal side effects can be achieved with siPLK1 is another attractive advantage. Once RNAi is established within mammalian cells, gene silencing can persist for many days due to the relative stability of activated RISC in the presence of its complementary mRNA<sup>194</sup>. Therefore, the maintenance of drug activity for a siRNA therapeutic is uncoupled from the requirement to maintain an effective drug concentration in the blood.

To address the efficiency of siPLK1-StAv-SPIONs, we performed a randomized, placebo controlled study in mice bearing syngenic orthotopic tumor. Many *in vivo* models have combined human cells and immunodeficient mice. These models suffer from several shortcomings since normal tumor development and the role of the immune system cannot be evaluated due to the impaired immune system. Also, human cells may behave differently once xenografts transplanted into different species. Therefore, syngenic orthotopic tumor models in immunocompetent animals offer much more realistic conditions for studying

malignancies and the impact on the immune system<sup>110</sup>. We found the drastic decrease in the harvested tumor volume on siPLK1-StAv-SPIONs treatment these results prove the fact that siPLK1-StAv-SPIONs are not only available to the tumor but also signify the tumor siPLK1 silencing. Having ascertained the viability of delivery strategy in reducing tumor burden and increasing survival in these proof-of-principle experiments, we observed long term serum availability, better tolerance and tumor specific silencing of siPLK1. We believe that the attenuation of RNAi in the tumor most likely results from the effective killing of affected tumor cells and from the dilution of activated RISC through the proliferation of cells receiving sub-lethal doses of PLK1 siRNA<sup>193</sup>. We have demonstrated that systemic administration of siPLK1-StAv-SPIONs can trigger RNAi-mediated silencing of PLK1 within solid tumors, silencing target expression at a magnitude sufficient to induce the mitotic disruption and apoptosis of tumor cells and thus reducing the proliferation.

The orthotopic syngenic tumor model has been previously criticized for a less developed tumor vasculature and tumor microenvironment compared to an endogenous tumor model<sup>6</sup>. This impedes productive utility of syngenic orthotopic model in preclinical modeling: Unfortunately, neither cell based assays nor xenograft models are particularly successful in predicting drug responses in humans. A broad analysis of *in vitro* models and tumor xenografts found poor correlations with activity in phase II clinical trials and generally concluded that only compounds that are successful in a large number of different models are likely to be effective in the clinic<sup>195</sup>. Genetically engineered mouse models (GEMM) are a promising alternative to traditional preclinical assays and address many of the shortcomings of cell-based assays and xenografts. GEMs provide *in situ* tumor development in an immunocompetent animal setting. LSL-Kras<sup>G12D</sup>, LSL-Trp53<sup>R172H</sup>, Pdx-1-Cre (KPC) mice, spontaneously develop immunocompetent PDAC that resemble to histopathologic and molecular features of human PDAC, thought to be relevant for validating treatment efficacy in patients<sup>30,112,196</sup>. We replicated a prospective, randomized, double blind, placebo control pilot study in KPC mice to evaluate of efficacy of siPLK1-StAv-SPIONs on tumor progression. We observed complimentary findings to that of in the syngenic orthotopic tumor model in reducing tumor burden and silencing PLK1.

The combination of the favorable biodistribution of these nanoparticles to tumors and their imaging properties represents an exciting possibility for the simultaneous delivery and detection of siRNA based therapeutic agents *in vivo*. The feasibility of such studies is underscored by the recent demonstration of substantial silencing in nonhuman primates following systemic siRNA administration at clinically relevant doses<sup>104</sup>. One of the main advantages offered by siPLK1-StAv-SPIONs is the possibility to carry out validation studies of selective targets using specific siRNAs at different stages of tumor development.

Moreover, validated targets can be used in combination of traditional chemotherapeutic agents leading to the identification of therapeutic strategies.

Currently, the only treatment approved to treat PDAC tumors is gemcitabine. Yet, the average increased survival offered by gemcitabine is minimal (4-5 months)<sup>197</sup>. In the KPC model, gemcitabine cannot be delivered to the tumor cells. One of the major reasons for insufficient delivery is stromal barrier and nonspecific targeting. Limited depletion of stromal cells using a Hedgehog antagonist such as IPI-926 allowed robust gemcitabine delivery into the tumor and increased therapeutic efficacy<sup>30</sup>. Recently, a KPC model has been developed to target stromal tissue using a PEGylated hyaluronidase<sup>128,129</sup>. These studies identified elimination of the stromal hyaluronan diminishes hydrostatic pressure, allowing efflux of the administered chemotherapeutic agent's thus improving therapeutic outcome. These results suggest that a strategy to improve localisation of chemotherapeutic agent to the tumor cells may improve therapeutic outcome of the treatment by specific tumor cells targeting. We believe, siPLK1-StAv-SPIONs provide one of the opportunities to tumor specific efficient delivery. However, we need to emphasize that the precise mechanism mediating efficient gene silencing in vivo remain to be fully understood.

Overall, we believe that our study represents an important new step toward the application of siRNAs as cancer therapeutic agents by providing a new imaging strategy with which to assess their delivery and tumor specific silencing.

## 7. SUMMARY

Pancreatic ductal adenocarcinoma (PDAC) is one of the most aggressive malignancy and projected to be the third leading cause of cancer related death by 2030<sup>12,14</sup>. Despite extensive knowledge and insights into biological properties and genetic aberrations of pancreatic ductal adenocarcinoma cells, therapeutic options remain temporary and ineffective<sup>13,32,195</sup>. One plausible explanation for the futile response to therapy is an insufficient and nonspecific delivery of anticancer drugs to the tumor site<sup>30,128,129</sup>. Superparamagnetic iron oxide nanoparticles (SPION) coupled with siRNA targeted against the cell cycle specific serine-threonine-kinase, Polo-like kinase-1 (siPLK1-StAv-SPIONs) could serve a dual purpose for delivery of siPLK1 to tumor and noninvasive assessment of delivery *in vivo*. siPLK1-StAv-SPIONs were designed as theranostics to function via a membrane translocation peptide (MPAP-) as well as a tumor selective peptide (EPPT-1) to increase intracellular delivery and tumor specificity, respectively. *In vitro* and *in vivo* experiments using a syngenic orthotopic PDAC model as well as the endogenous LSL-Kras<sup>G12D</sup>, LSL-Trp53<sup>R172H</sup>, Pdx-1-Cre model revealed significant accumulation of siPLK1-StAv-SPIONs in PDAC resulting in efficient *PLK1* silencing. Tumor specific silencing of *PLK1* halts tumor growth, marked by decrease in tumor cell proliferation and increase in apoptosis. siPLK1-StAv-SPIONs are well tolerated with no observed systemic side effects. Our data suggests, siPLK1-StAv-SPIONs with dual specificity residues for tumor targeting and membrane translocation, represent an exciting opportunity for targeted therapy in PDAC.

## 8. ZUSAMMENFASSUNG

Das duktale Adenokarzinom des Pankreas (PDAC) zählt zu den aggressivsten Krebserkrankungen und wird bis 2030 als dritthäufigste krebsbedingte Todesursache angenommen<sup>12,14</sup>. Intensive Arbeiten zu biologischen Eigenschaften und genetischen Aberrationen der Krebszellen haben nicht zu einem effektiven therapeutische Ansatz geführt bzw. nur eine kurzzeitige Besserung<sup>13,32,195</sup>. Eine mögliche Erklärung für das fehlende Therapieansprechen könnte der unzureichende und unspezifische Transport von Zytostatika in den Tumor sein<sup>30,128,129</sup>. „Superparamagnetic iron oxide nanoparticles“ (SPION) gekoppelt mit siRNA, die sich gegen die zellzyklusspezifische serine-threonine-kinase, Polo-like kinase-1 (siPLK1-StAv-SPIONs), richten, könnten zwei Ziele verfolgen: den Transport und die gerichtete Aufnahme von siPLK1 zum Tumor sowie die Anreicherung der Eisenpartikel im Tumor im MRT. siPLK1-StAv-SPIONs fungieren damit als „theranostics“. Das Membrantranslokationspeptid(MPAP-) sowie das tumorselektive Peptid (EPPT1-), führen zu einer gezielten Aufnahme, erhöhen die intrazelluläre Verfügbarkeit und die Spezifität des Wirkstoffes. In *in vitro* und *in vivo* Experimenten in einem syngenem orthotopen Tumormodell sowie einem endogenen Pankreaskarzinommodell der Maus (LSL-KrasG12D,LSL-Trp53R172H,Pdx-1-Cre) konnte eine signifikante Anreicherung von siPLK1-StAv-SPIONs in Karzinom nachgewiesen werden. Dies führte zu einer signifikant verminderten Expression von PLK1. Die tumorspezifische Suppression der PLK1 Expression verhindert ein Wachstum des Tumors mit einer verminderten Proliferationsrate sowie einer signifikant gesteigerten Apoptoserate. Für siPLK1-StAv-SPIONs wurden keine systemischen Nebenwirkungen beobachtet. siPLK1-StAv-SPIONs wirken durch die Bindung an das Oberflächenprotein MUC1 des Pankreaskarzinoms und durch die MPAP vermittelte Endozytose als spezifisches und effektives Instrument zur zielgerichteten Therapie des Pankreaskarzinoms.

## 9. REFERENCES

1. Maitra, A. & Leach, S.D. Disputed paternity: the uncertain ancestry of pancreatic ductal neoplasia. *Cancer cell* 22, 701-703 (2012).
2. Zhang, Y., *et al.* The expression of PLK-1 in cervical carcinoma: a possible target for enhancing chemosensitivity. *Journal of Experimental & Clinical Cancer Research: CR* 28, 130 (2009).
3. Yamaguchi, T., *et al.* Phosphorylation by Cdk1 induces Plk1-mediated vimentin phosphorylation during mitosis. *The Journal of cell biology* 171, 431 (2005).
4. Rizki, A., Mott, J.D. & Bissell, M.J. Polo-like kinase 1 is involved in invasion through extracellular matrix. *Cancer Research* 67, 11106-11110 (2007).
5. Gray, P.J., *et al.* Identification of human polo-like kinase 1 as a potential therapeutic target in pancreatic cancer. *Molecular cancer therapeutics* 3, 641-646 (2004).
6. Zhang, Y., *et al.* Study human pancreatic cancer in mice: how close are they? *Biochim Biophys Acta* 1835, 110-118 (2013).
7. Raab, M., *et al.* Toxicity modelling of Plk1-targeted therapies in genetically engineered mice and cultured primary mammalian cells. *Nature communications* 2, 395 (2011).
8. Poste, G. & Kirsh, R. Site Specific (Targeted) Drug Delivery in Cancer Therapy. *Nature biotechnology* 1, 869-878 (1983).
9. Cho, K., Wang, X., Nie, S. & Shin, D.M. Therapeutic nanoparticles for drug delivery in cancer. *Clinical cancer research* 14, 1310-1316 (2008).
10. Kelkar, S.S. & Reineke, T.M. Theranostics: combining imaging and therapy. *Bioconjugate chemistry* 22, 1879-1903 (2011).
11. Thorek, D.L., Chen, A.K., Czupryna, J. & Tsourkas, A. Superparamagnetic iron oxide nanoparticle probes for molecular imaging. *Annals of biomedical engineering* 34, 23-38 (2006).
12. Vincent, A., Herman, J., Schulick, R., Hruban, R.H. & Goggins, M. Pancreatic cancer. *Lancet* 378, 607-620 (2011).
13. Sultana, A., *et al.* Meta-analyses of chemotherapy for locally advanced and metastatic pancreatic cancer. *J Clin Oncol* 25, 2607-2615 (2007).
14. Rahib, L., *et al.* Projecting Cancer Incidence and Deaths to 2030: The Unexpected Burden of Thyroid, Liver, and Pancreas Cancers in the United States. *Cancer research* 74, 2913-2921 (2014).
15. McConkey, D.J. Apoptosis Signaling Pathways in Pancreatic Cancer Pathogenesis. *Handbook of Pancreatic Cancer* 14(2009).
16. Whibley, C., Pharoah, P.D. & Hollstein, M. p53 polymorphisms: cancer implications. *Nature Rev. Cancer* 9, 95-107 (2009).
17. Jänicke, R.U., Sohn, D. & Schulze-Osthoff, K. The dark side of a tumor suppressor: anti-apoptotic p53. *Cell Death & Differentiation* 15, 959-976 (2008).
18. Jani, J.P., *et al.* PF-03814735, an Orally Bioavailable Small Molecule Aurora Kinase Inhibitor for Cancer Therapy. *Molecular cancer therapeutics* 9, 883 (2010).
19. Bartsch, D.K., Gress, T.M. & Langer, P. Familial pancreatic cancer--current knowledge. *Nat Rev Gastroenterol Hepatol* 9, 445-453 (2012).
20. Klein, A.P., *et al.* Linkage analysis of chromosome 4 in families with familial pancreatic cancer. *Cancer Biol Ther* 6, 320-323 (2007).
21. Yadav, D. & Whitcomb, D.C. The role of alcohol and smoking in pancreatitis. *Nat Rev Gastroenterol Hepatol* 7, 131-145 (2010).
22. Whitcomb, D.C. Mechanisms of disease: advances in understanding the mechanisms leading to chronic pancreatitis. *Nature Clinical Practice Gastroenterology & Hepatology* 1, 46-52 (2004).
23. Butler, A.E., *et al.* Pancreatic duct replication is increased with obesity and type 2 diabetes in humans. *Diabetologia* 53, 21-26 (2010).
24. Raimondi, S., Maisonneuve, P. & Lowenfels, A.B. Epidemiology of pancreatic cancer: an overview. *Nat Rev Gastroenterol Hepatol* 6, 699-708 (2009).
25. Hruban, R.H., Maitra, A. & Goggins, M. Update on pancreatic intraepithelial neoplasia. *International journal of clinical and experimental pathology* 1, 306 (2008).
26. Winter, J.M., Maitra, A. & Yeo, C.J. Genetics and pathology of pancreatic cancer. *HPB* 8, 324-336 (2006).
27. Maitra, A., Kern, S.E. & Hruban, R.H. Molecular pathogenesis of pancreatic cancer. *Best Practice & Research Clinical Gastroenterology* 20, 211-226 (2006).

28. Mimeault, M., Brand, R.E., Sasson, A.A. & Batra, S.K. Recent advances on the molecular mechanisms involved in pancreatic cancer progression and therapies. *Pancreas* 31, 301-316 (2005).
29. Jimeno, A. & Hidalgo, M. Molecular biomarkers: their increasing role in the diagnosis, characterization, and therapy guidance in pancreatic cancer. *Mol Cancer Ther* 5, 787-796 (2006).
30. Olive, K.P., *et al.* Inhibition of Hedgehog signaling enhances delivery of chemotherapy in a mouse model of pancreatic cancer. *Science* 324, 1457-1461 (2009).
31. Sarkar, F.H., Banerjee, S. & Li, Y. Pancreatic cancer: pathogenesis, prevention and treatment. *Toxicol Appl Pharmacol* 224, 326-336 (2007).
32. Bardeesy, N. & DePinho, R.A. Pancreatic cancer biology and genetics. *Nature Reviews Cancer* 2, 897-909 (2002).
33. Almoguera, C., *et al.* Most human carcinomas of the exocrine pancreas contain mutant c-K-ras genes. *Cell* 53, 549-554 (1988).
34. Calhoun, E.S., *et al.* BRAF and FBXW7 (CDC4, FBW7, AGO, SEL10) mutations in distinct subsets of pancreatic cancer: potential therapeutic targets. *Am J Pathol* 163, 1255-1260 (2003).
35. Vugt, M.A.v., Smits, V.A., Klompmaker, R. & Medema, R.H. Inhibition of polo-like kinase-1 by DNA damage occurs in an ATM- or ATR-dependent fashion. *J. Biol. Chem.* 276, 41656–41660 (2001).
36. Wong, H.H. & Lemoine, N.R. Pancreatic cancer: molecular pathogenesis and new therapeutic targets. *Nature Reviews Gastroenterology and Hepatology* 6, 412-422 (2009).
37. Mundt, K.E., Golsteyn, R.M., Lane, H.A. & Nigg, E.A. On the regulation and function of human polo-like kinase 1 (PLK1): Effects of overexpression on cell cycle progression. *Biochem. Biophys. Res. Commun.* 239, 377–385 (1997).
38. Radulovich, N., *et al.* Differential roles of cyclin D 1 and D 3 in pancreatic ductal adenocarcinoma. *Molecular Cancer* 9, 24 (2010).
39. Rape, M. Cell cycle: on-time delivery of Plk1 during cytokinesis. *Current Biology* 17, R506-R508 (2007).
40. Schoffski, P. Polo-Like Kinase (PLK) Inhibitors in Preclinical and Early Clinical Development in Oncology. *The Oncologist* (2009).
41. Malumbres, M. & Barbacid, M. Cell cycle kinases in cancer. *Current opinion in genetics & development* 17, 60-65 (2007).
42. Kastan, M.B. & Bartek, J. Cell-cycle checkpoints and cancer. *Nature* 432, 316-323 (2004).
43. Wang, Y., *et al.* Centrosome-associated regulators of the G 2/M checkpoint as targets for cancer therapy. *Molecular Cancer* 8, 8 (2009).
44. Tang, J., Erikson, R.L. & Liu, X. Checkpoint kinase 1 (Chk1) is required for mitotic progression through negative regulation of polo-like kinase 1 (Plk1). *Proc. Natl Acad. Sci* 103, 11964-11969 (2006).
45. Barr, F.A. & Gruneberg, U. Cytokinesis: placing and making the final cut. *Cell* 131, 847-860 (2007).
46. Barr, F.A., Sillje, H.H. & Nigg, E.A. Polo-like kinases and the orchestration of cell division. *Nature reviews Molecular cell biology* 5, 429-441 (2004).
47. Jeong, K.H., Jeong, J.Y., Lee, H.O., Choi, E. & Lee, H. Inhibition of Plk1 Induces Mitotic Infidelity and Embryonic Growth Defects in Developing Zebrafish Embryos. *Developmental Biology* (2010).
48. Strebhardt, K. Multifaceted polo-like kinases: drug targets and antitargets for cancer therapy. *Nature reviews Drug discovery* 9, 643-660 (2010).
49. Nigg, E.A. Polo-like kinases: positive regulators of cell division from start to finish. *Current opinion in cell biology* 10, 776-783 (1998).
50. Archambault, V. & Glover, D.M. Polo-like kinases: conservation and divergence in their functions and regulation. *Nature reviews Molecular cell biology* 10, 265-275 (2009).
51. Takai, N., Hamanaka, R., Yoshimatsu, J. & Miyakawa, I. Polo-like kinases (Plks) and cancer. *Oncogene* 24, 287-291 (2005).
52. Ando, K., *et al.* Polo-like kinase 1 (Plk1) inhibits p53 function by physical interaction and phosphorylation. *Journal of Biological Chemistry* 279, 25549 (2004).
53. McInnes, C. & Wyatt, M.D. PLK1 as an oncology target: current status and future potential. *Drug discovery today* 16, 619-625 (2011).
54. Lee, M., Daniels, M.J. & Venkitaraman, A.R. Phosphorylation of BRCA2 by the polo-like kinase Plk1 is regulated by DNA damage and mitotic progression. *Oncogene* 23, 865-872 (2004).

55. Lindqvist, A., Rodríguez-Bravo, V. & Medema, R.H. The decision to enter mitosis: feedback and redundancy in the mitotic entry network. *The Journal of cell biology* 185, 193 (2009).
56. Pellegrino, R., *et al.* Oncogenic and tumor suppressive roles of polo-like kinases in human hepatocellular carcinoma. *Hepatology* 51, 857-868 (2010).
57. Syljuasen, R.G., Jensen, S., Bartek, J. & Lukas, J. Adaptation to the ionizing radiation-induced G2 checkpoint occurs in human cells and depends on checkpoint kinase 1 and polo-like kinase 1 kinases. *Cancer research* 2, 10253-10257 (2006).
58. Meraldi, P., Honda, R. & Nigg, E.A. Aurora-A overexpression reveals tetraploidization as a major route to centrosome amplification in p53<sup>-/-</sup> cells. *EMBO J.* 21, 4830492 (2002).
59. Liu, X., Lei, M. & Erikson, R.L. Normal cells, but not cancer cells, survive severe Plk1 depletion. *Molecular and cellular biology* 26, 2093-2108 (2006).
60. Strebhardt, K. & Ullrich, A. Targeting polo-like kinase 1 for cancer therapy. *Nature Reviews Cancer* 6, 321-330 (2006).
61. Yim, H. Current clinical trials with polo-like kinase 1 inhibitors in solid tumors. *Anti-cancer drugs* 24, 999-1006 (2013).
62. Lens, S.M., Voest, E.E. & Medema, R.H. Shared and separate functions of polo-like kinases and aurora kinases in cancer. *Nature Reviews Cancer* 10, 825-841 (2010).
63. Olmos, D., Swanton, C. & de Bono, J. Targeting polo-like kinase: learning too little too late? *Journal of Clinical Oncology* 26, 5497-5499 (2008).
64. Mross, K., *et al.* A randomised phase II trial of the Polo-like kinase inhibitor BI 2536 in chemo-naive patients with unresectable exocrine adenocarcinoma of the pancreas: a study within the Central European Society Anticancer Drug Research (CESAR) collaborative network. *British journal of cancer* 107, 280-286 (2012).
65. Lin, C.C., *et al.* A phase I study of two dosing schedules of volasertib (BI 6727), an intravenous polo-like kinase inhibitor, in patients with advanced solid malignancies. *Br J Cancer* 110, 2434-2440 (2014).
66. Olmos, D., *et al.* Phase I study of GSK461364, a specific and competitive Polo-like kinase 1 inhibitor, in patients with advanced solid malignancies. *Clinical cancer research* 17, 3420-3430 (2011).
67. Garland, L.L., Taylor, C., Pilkington, D.L., Cohen, J.L. & Von Hoff, D.D. A phase I pharmacokinetic study of HMN-214, a novel oral stilbene derivative with polo-like kinase-1 interacting properties, in patients with advanced solid tumors. *Clinical cancer research* 12, 5182-5189 (2006).
68. Jimeno, A., *et al.* Phase I study of ON 01910. Na, a novel modulator of the Polo-like kinase 1 pathway, in adult patients with solid tumors. *Journal of Clinical Oncology* 26, 5504-5510 (2008).
69. Corti, A., *et al.* Targeted drug delivery and penetration into solid tumors. *Medicinal research reviews* 32, 1078-1091 (2011).
70. Tannock, I.F. Tumor physiology and drug resistance. *Cancer and Metastasis Reviews* 20, 123-132 (2001).
71. Moses, M.A., Brem, H. & Langer, R. Advancing the field of drug delivery: taking aim at cancer. *Cancer cell* 4, 337-341 (2003).
72. Spankuch, B., *et al.* Cancer inhibition in nude mice after systemic application of U6 promoter driven short hairpin RNAs against PLK1. *Journal of the National Cancer Institute* 96, 862-872 (2004).
73. Dassie, J.P., *et al.* Systemic administration of optimized aptamer-siRNA chimeras promotes regression of PSMA-expressing tumors. *Nature biotechnology* 27, 839-846 (2009).
74. McNamara, J.O., *et al.* Cell type-specific delivery of siRNAs with aptamer-siRNA chimeras. *Nature biotechnology* 24, 1005-1015 (2006).
75. Yang, X.Z., *et al.* Systemic delivery of siRNA with cationic lipid assisted PEG-PLA nanoparticles for cancer therapy. *J Control Release* 156, 203-211 (2011).
76. Davidson, B.L. & McCray, P.B. Current prospects for RNA interference-based therapies. *Nature Reviews Genetics* 12, 329-340 (2011).
77. Castanotto, D. & Rossi, J.J. The promises and pitfalls of RNA-interference-based therapeutics. *Nature* 457, 426-433 (2009).
78. Gondi, C.S. & Rao, J.S. Concepts in in vivo siRNA delivery for cancer therapy. *Journal of cellular physiology* 220, 285-291 (2009).
79. Wang, X., Yang, L., Chen, Z.G. & Shin, D.M. Application of nanotechnology in cancer therapy and imaging. *CA: a cancer journal for clinicians* 58, 97-110 (2008).
80. Wang, J., Lu, Z., Wientjes, M.G. & Au, J.L.-S. Delivery of siRNA therapeutics: barriers and carriers. *The AAPS journal* 12, 492-503 (2010).

81. De Paula, D., Bentley, M.V.r.L. & Mahato, R.I. Hydrophobization and bioconjugation for enhanced siRNA delivery and targeting. *RNA* 13, 431-456 (2007).
82. Lane, H.A. & Nigg, E.A. Antibody microinjection reveals an essential role for human polo-like kinase 1 (Plk1) in the functional maturation of mitotic centrosomes. *The Journal of cell biology* 135, 1701-1713 (1996).
83. Lee, D.Y. & Li, K.C. Molecular theranostics: a primer for the imaging professional. *AJR. American journal of roentgenology* 197, 318 (2011).
84. Xie, J., Lee, S. & Chen, X. Nanoparticle-based theranostic agents. *Advanced drug delivery reviews* 62, 1064-1079 (2010).
85. Ahmed, N., Fessi, H. & Elaissari, A. Theranostic applications of nanoparticles in cancer. *Drug Discovery Today* 17, 928-934 (2012).
86. Gupta, A.K. & Gupta, M. Cytotoxicity suppression and cellular uptake enhancement of surface modified magnetic nanoparticles. *Biomaterials* 26, 1565-1573 (2005).
87. Gupta, A.K. & Gupta, M. Synthesis and surface engineering of iron oxide nanoparticles for biomedical applications. *Biomaterials* 26, 3995-4021 (2005).
88. Xie, J. & Jon, S. Magnetic nanoparticle-based theranostics. *Theranostics* 2, 122 (2012).
89. Si, S., *et al.* Magnetic monodisperse Fe<sub>3</sub>O<sub>4</sub> nanoparticles. *Crystal growth & design* 5, 391-393 (2005).
90. Dresco, P.A., Zaitsev, V.S., Gambino, R.J. & Chu, B. Preparation and properties of magnetite and polymer magnetite nanoparticles. *Langmuir* 15, 1945-1951 (1999).
91. Hoffman-Amtenbrink, M., Von Rechenberg, B. & Hofmann, H. Superparamagnetic nanoparticles for biomedical applications. (2009).
92. Gass, J., Poddar, P., Almand, J., Srinath, S. & Srikanth, H. Superparamagnetic polymer nanocomposites with uniform Fe<sub>3</sub>O<sub>4</sub> nanoparticle dispersions. *Advanced Functional Materials* 16, 71-75 (2006).
93. Shao, H., Yoon, T.-J., Liong, M., Weissleder, R. & Lee, H. Magnetic nanoparticles for biomedical NMR-based diagnostics. *Beilstein journal of nanotechnology* 1, 142-154 (2010).
94. Allen, T.M. Ligand-targeted therapeutics in anticancer therapy. *Nature Reviews Cancer* 2, 750-763 (2002).
95. Hinoda, Y., *et al.* Increased expression of MUC1 in advanced pancreatic cancer. *J Gastroenterol* 38, 1162-1166 (2003).
96. Goldenberg, D.M. Targeted therapy of cancer with radiolabeled antibodies. *Journal of Nuclear Medicine* 43, 693-713 (2002).
97. Ghosh, S.K., Pantazopoulos, P., Medarova, Z. & Moore, A. Expression of underglycosylated MUC1 antigen in cancerous and adjacent normal breast tissues. *Clin Breast Cancer* 13, 109-118 (2013).
98. Ghosh, S.K., *et al.* Targeted imaging of breast tumor progression and therapeutic response in a human uMUC-1 expressing transgenic mouse model. *Int J Cancer* 132, 1860-1867 (2013).
99. Medarova, Z., Rashkovetsky, L., Pantazopoulos, P. & Moore, A. Multiparametric monitoring of tumor response to chemotherapy by noninvasive imaging. *Cancer Res* 69, 1182-1189 (2009).
100. Moore, A., Medarova, Z., Potthast, A. & Dai, G. In vivo targeting of underglycosylated MUC-1 tumor antigen using a multimodal imaging probe. *Cancer Res* 64, 1821-1827 (2004).
101. Kumar, M., Medarova, Z., Pantazopoulos, P., Dai, G. & Moore, A. Novel membrane permeable contrast agent for brain tumor detection by MRI. *Magnetic Resonance in Medicine* 63, 617-624 (2010).
102. Pham, W., Kircher, M.F., Weissleder, R. & Tung, C.H. Enhancing membrane permeability by fatty acylation of oligoarginine peptides. *ChemBiochem* 5, 1148-1151 (2004).
103. Ifediba, M.A., Medarova, Z., Ng, S.-W., Yang, J. & Moore, A. siRNA delivery to CNS cells using a membrane translocation peptide. *Bioconjugate chemistry* 21, 803-806 (2010).
104. Medarova, Z., Pham, W., Farrar, C., Petkova, V. & Moore, A. In vivo imaging of siRNA delivery and silencing in tumors. *Nat Med* 13, 372-377 (2007).
105. Medarova, Z., *et al.* In vivo imaging of autologous islet grafts in the liver and under the kidney capsule in non-human primates. *Transplantation* 87, 1659-1666 (2009).
106. Yigit, M.V., Moore, A. & Medarova, Z. Magnetic nanoparticles for cancer diagnosis and therapy. *Pharm Res* 29, 1180-1188 (2012).
107. Li, C.X., *et al.* Delivery of RNA interference. *Cell cycle- Landes Bioscience* 5, 2103 (2006).
108. Palmacci, S. & Josephson, L. Synthesis of polysaccharide covered superparamagnetic oxide colloids. (Google Patents, USA, 1993).
109. Cornelsen, M., Helm, C.A. & Block, S. Destabilization of Polyelectrolyte Multilayers Formed at Different Temperatures and Ion Concentrations. *Macromolecules* 43, 4300-4309 (2010).

110. Partecke, I.L., *et al.* In vivo imaging of pancreatic tumours and liver metastases using 7 Tesla MRI in a murine orthotopic pancreatic cancer model and a liver metastases model. *BMC Cancer* 11, 40 (2011).
111. Sugahara, K.N., *et al.* Tissue-penetrating delivery of compounds and nanoparticles into tumors. *Cancer Cell* 16, 510-520 (2009).
112. Hingorani, S.R., *et al.* Trp53R172H and KrasG12D cooperate to promote chromosomal instability and widely metastatic pancreatic ductal adenocarcinoma in mice. *Cancer Cell* 7, 469-483 (2005).
113. Neesse, A., *et al.* SPARC independent drug delivery and antitumour effects of nab-paclitaxel in genetically engineered mice. *Gut* 63, 974-983 (2014).
114. Riemer, J., Hoepken, H.H., Czerwinska, H., Robinson, S.R. & Dringen, R. Colorimetric ferrozine-based assay for the quantitation of iron in cultured cells. *Anal Biochem* 331, 370-375 (2004).
115. Darzynkiewicz, Z., Juan, G. & Bedner, E. Determining cell cycle stages by flow cytometry. *Curr Protoc Cell Biol* 8, 8.4 (2001).
116. Richardson, K.C., Jarett, L. & Finke, E.H. Embedding in epoxy resins for ultrathin sectioning in electron microscopy. *Stain Technol* 35, 313-323 (1960).
117. Zhang, Y., Huo, M., Zhou, J. & Xie, S. PKSolver: An add-in program for pharmacokinetic and pharmacodynamic data analysis in Microsoft Excel. *Comput Methods Programs Biomed* 99, 306-314 (2010).
118. Peer, D., *et al.* Nanocarriers as an emerging platform for cancer therapy. *Nature Nanotechnology* 2, 751-760 (2007).
119. Bao, G., Mitragotri, S. & Tong, S. Multifunctional nanoparticles for drug delivery and molecular imaging. *Annual review of biomedical engineering* 15, 253-282 (2013).
120. Kim, B.Y., Rutka, J.T. & Chan, W.C. Nanomedicine. *New England Journal of Medicine* 363, 2434-2443 (2010).
121. Peng, S. & Sun, S. Synthesis and characterization of monodisperse hollow Fe<sub>3</sub>O<sub>4</sub> nanoparticles. *Angewandte Chemie* 119, 4233-4236 (2007).
122. Peng, X.-H., Qian, X., Mao, H. & Wang, A.Y. Targeted magnetic iron oxide nanoparticles for tumor imaging and therapy. *International journal of nanomedicine* 3, 311 (2008).
123. Jain, P.K., El-Sayed, I.H. & El-Sayed, M.A. Au nanoparticles target cancer. *nano today* 2, 18-29 (2007).
124. Jain, R.K. & Stylianopoulos, T. Delivering nanomedicine to solid tumors. *Nature reviews clinical oncology* 7, 653-664 (2010).
125. Jain, T.K., Morales, M.A., Sahoo, S.K., Leslie-Pelecky, D.L. & Labhasetwar, V. Iron oxide nanoparticles for sustained delivery of anticancer agents. *Molecular pharmaceutics* 2, 194-205 (2005).
126. Sawyers, C.L. The cancer biomarker problem. *Nature* 452, 548-552 (2008).
127. Medarova, Z. & Moore, A. MRI as a tool to monitor islet transplantation. *Nature Reviews Endocrinology* 5, 444-452 (2009).
128. Provenzano, P.P., *et al.* Enzymatic targeting of the stroma ablates physical barriers to treatment of pancreatic ductal adenocarcinoma. *Cancer Cell* 21, 418-429 (2012).
129. Jacobetz, M.A., *et al.* Hyaluronan impairs vascular function and drug delivery in a mouse model of pancreatic cancer. *Gut* 62, 112-120 (2013).
130. Boucher, Y. & Jain, R.K. Microvascular pressure is the principal driving force for interstitial hypertension in solid tumors: implications for vascular collapse. *Cancer Res* 52, 5110-5114 (1992).
131. Medarova, Z., *et al.* Noninvasive magnetic resonance imaging of microvascular changes in type 1 diabetes. *Diabetes* 56, 2677-2682 (2007).
132. Zimmer, C., *et al.* Tumor cell endocytosis imaging facilitates delineation of the glioma-brain interface. *Exp Neurol* 143, 61-69 (1997).
133. Maeda, H., Wu, J., Sawa, T., Matsumura, Y. & Hori, K. Tumor vascular permeability and the EPR effect in macromolecular therapeutics: a review. *J Control Release* 65, 271-284 (2000).
134. Moore, A. & Medarova, Z. Imaging of siRNA delivery and silencing. *Methods Mol Biol* 487, 93-110 (2009).
135. Tiemann, K. & Rossi, J.J. RNAi-based therapeutics-current status, challenges and prospects. *EMBO Mol Med* 1, 142-151 (2009).
136. Zimmermann, T.S., *et al.* RNAi-mediated gene silencing in non-human primates. *Nature* 441, 111-114 (2006).
137. Copolovici, D.M., Langel, K., Eriste, E. & Langel, U.I. Cell-Penetrating Peptides: Design, Synthesis, and Applications. *ACS nano* 8, 1972-1994 (2014).

138. Medarova, Z., Pham, W., Kim, Y., Dai, G. & Moore, A. In vivo imaging of tumor response to therapy using a dual-modality imaging strategy. *Int J Cancer* 118, 2796-2802 (2006).
139. Bertrand, N., Wu, J., Xu, X., Kamaly, N. & Farokhzad, O.C. Cancer nanotechnology: The impact of passive and active targeting in the era of modern cancer biology. *Advanced drug delivery reviews* 66, 2-25 (2013).
140. Carter, P. Improving the efficacy of antibody-based cancer therapies. *Nature Reviews Cancer* 1, 118-129 (2001).
141. Portney, N.G. & Ozkan, M. Nano-oncology: drug delivery, imaging, and sensing. *Analytical and Bioanalytical Chemistry* 384, 620-630 (2006).
142. Manchester, M. & Singh, P. Virus-based nanoparticles (VNPs): platform technologies for diagnostic imaging. *Advanced drug delivery reviews* 58, 1505-1522 (2006).
143. Lewis, J.D., *et al.* Viral nanoparticles as tools for intravital vascular imaging. *Nature medicine* 12, 354-360 (2006).
144. Parveen, S. & Sahoo, S.K. Polymeric nanoparticles for cancer therapy. *Journal of drug targeting* 16, 108-123 (2008).
145. Barbas, A.S., Mi, J., Clary, B.M. & White, R.R. Aptamer applications for targeted cancer therapy. *Future Oncology* 6, 1117-1126 (2010).
146. Gu, F.X., *et al.* Targeted nanoparticles for cancer therapy. *nano today* 2, 14-21 (2007).
147. Morris, M.C., Depollier, J., Mery, J., Heitz, F. & Divita, G. A peptide carrier for the delivery of biologically active proteins into mammalian cells. *Nature biotechnology* 19, 1173-1176 (2001).
148. Park, J.H., *et al.* Polymeric nanomedicine for cancer therapy. *Progress in Polymer Science* 33, 113-137 (2008).
149. Bharali, D.J., Khalil, M., Gurbuz, M., Simone, T.M. & Mousa, S.A. Nanoparticles and cancer therapy: a concise review with emphasis on dendrimers. *International journal of nanomedicine* 4, 1 (2009).
150. Baker, J.R. Dendrimer-based nanoparticles for cancer therapy. *ASH Education Program Book* 2009, 708-719 (2009).
151. Wolinsky, J.B. & Grinstaff, M.W. Therapeutic and diagnostic applications of dendrimers for cancer treatment. *Adv Drug Deliv Rev* 60, 1037-1055 (2008).
152. Riehemann, K., *et al.* Nanomedicine: challenge and perspectives. *Angewandte Chemie International Edition* 48, 872-897 (2009).
153. Neuberger, T., Schaepf, B., Hofmann, H., Hofmann, M. & Von Rechenberg, B. Superparamagnetic nanoparticles for biomedical applications: possibilities and limitations of a new drug delivery system. *Journal of Magnetism and Magnetic Materials* 293, 483-496 (2005).
154. Kievit, F.M. & Zhang, M. Surface engineering of iron oxide nanoparticles for targeted cancer therapy. *Accounts of chemical research* 44, 853-862 (2011).
155. Sun, C., Lee, J.S. & Zhang, M. Magnetic nanoparticles in MR imaging and drug delivery. *Advanced drug delivery reviews* 60, 1252-1265 (2008).
156. Chertok, B., *et al.* Iron oxide nanoparticles as a drug delivery vehicle for MRI monitored magnetic targeting of brain tumors. *Biomaterials* 29, 487-496 (2008).
157. El-Sayed, I.H., Huang, X. & El-Sayed, M.A. Surface plasmon resonance scattering and absorption of anti-EGFR antibody conjugated gold nanoparticles in cancer diagnostics: applications in oral cancer. *Nano letters* 5, 829-834 (2005).
158. Huang, X., El-Sayed, I.H., Qian, W. & El-Sayed, M.A. Cancer cell imaging and photothermal therapy in the near-infrared region by using gold nanorods. *Journal of the American Chemical Society* 128, 2115-2120 (2006).
159. Lim, Z.-Z.J., Li, J.-E.J., Ng, C.-T., Yung, L.-Y.L. & Bay, B.-H. Gold nanoparticles in cancer therapy. *Acta Pharmacologica Sinica* 32, 983-990 (2011).
160. Argyo, C., Weiss, V., Braluchle, C. & Bein, T. Multifunctional mesoporous silica nanoparticles as a universal platform for drug delivery. *Chemistry of Materials* 26, 435-451 (2014).
161. Rosenholm, J.M., *et al.* Targeting of porous hybrid silica nanoparticles to cancer cells. *ACS nano* 3, 197-206 (2009).
162. Lu, J., *et al.* Mesoporous silica nanoparticles for cancer therapy: energy-dependent cellular uptake and delivery of paclitaxel to cancer cells. *Nanobiotechnology* 3, 89-95 (2007).
163. Gobin, A.M., *et al.* Near-infrared resonant nanoshells for combined optical imaging and photothermal cancer therapy. *Nano letters* 7, 1929-1934 (2007).
164. Liu, Z., *et al.* Drug delivery with carbon nanotubes for in vivo cancer treatment. *Cancer research* 68, 6652-6660 (2008).
165. Lal, S., Clare, S.E. & Halas, N.J. Nanoshell-enabled photothermal cancer therapy: impending clinical impact. *Accounts of chemical research* 41, 1842-1851 (2008).

166. Samia, A.C., Chen, X. & Burda, C. Semiconductor quantum dots for photodynamic therapy. *Journal of the American Chemical Society* 125, 15736-15737 (2003).
167. Bakalova, R., Ohba, H., Zhelev, Z., Ishikawa, M. & Baba, Y. Quantum dots as photosensitizers? *Nature biotechnology* 22, 1360-1361 (2004).
168. Gao, X., Cui, Y., Levenson, R.M., Chung, L.W. & Nie, S. In vivo cancer targeting and imaging with semiconductor quantum dots. *Nature biotechnology* 22, 969-976 (2004).
169. Mroz, P., *et al.* Photodynamic therapy with fullerenes. *Photochemical & Photobiological Sciences* 6, 1139-1149 (2007).
170. Zakharian, T.Y., *et al.* A fullerene-paclitaxel chemotherapeutic: synthesis, characterization, and study of biological activity in tissue culture. *Journal of the American Chemical Society* 127, 12508-12509 (2005).
171. Haley, B. & Frenkel, E. Nanoparticles for drug delivery in cancer treatment. in *Urologic Oncology: Seminars and original investigations*, Vol. 26 57-64 (Elsevier, 2008).
172. Noh, S.M., *et al.* Pegylated poly-l-arginine derivatives of chitosan for effective delivery of siRNA. *Journal of Controlled Release* 145, 159-164 (2010).
173. Raab, M., *et al.* Toxicity modelling of Plk1-targeted therapies in genetically engineered mice and cultured primary mammalian cells. *Nat Commun* 2, 395 (2011).
174. Schmit, T.L., Zhong, W., Setaluri, V., Spiegelman, V.S. & Ahmad, N. Targeted depletion of Polo-like kinase (Plk) 1 through lentiviral shRNA or a small-molecule inhibitor causes mitotic catastrophe and induction of apoptosis in human melanoma cells. *J Invest Dermatol* 129, 2843-2853 (2009).
175. Spankuch-Schmitt, B., Bereiter-Hahn, J., Kaufmann, M. & Strebhardt, K. Effect of RNA silencing of polo-like kinase-1 (PLK1) on apoptosis and spindle formation in human cancer cells. *J Natl Cancer Inst* 94, 1863-1877 (2002).
176. Schulze, E., *et al.* Cellular Uptake and Trafficking of a Prototypical Magnetic Iron-Oxide Label in-Vitro. *Investigative Radiology* 30, 604-610 (1995).
177. Raynal, I., *et al.* Macrophage endocytosis of superparamagnetic iron oxide nanoparticles - Mechanisms and comparison of Ferumoxides and Ferumoxtran-10. *Investigative Radiology* 39, 56-63 (2004).
178. McMahon, H.T. & Boucrot, E. Molecular mechanism and physiological functions of clathrin-mediated endocytosis. *Nat Rev Mol Cell Biol* 12, 517-533 (2011).
179. Grant, B.D. & Donaldson, J.G. Pathways and mechanisms of endocytic recycling. *Nat Rev Mol Cell Biol* 10, 597-608 (2009).
180. Conner, S.D. & Schmid, S.L. Regulated portals of entry into the cell. *Nature* 422, 37-44 (2003).
181. Kirchhausen, T., Macia, E. & Pelish, H.E. Use of dynasore, the small molecule inhibitor of dynamin, in the regulation of endocytosis. *Methods Enzymol* 438, 77-93 (2008).
182. van den Boorn, J.G., Schlee, M., Coch, C. & Hartmann, G. SiRNA delivery with exosome nanoparticles. *Nat Biotechnol* 29, 325-326 (2011).
183. Yezhelyev, M.V., Qi, L.F., O'Regan, R.M., Nie, S. & Gao, X.H. Proton-sponge coated quantum dots for siRNA delivery and intracellular imaging. *Journal of the American Chemical Society* 130, 9006-9012 (2008).
184. Yang, S. & May, S. Release of cationic polymer-DNA complexes from the endosome: A theoretical investigation of the proton sponge hypothesis. *Journal of Chemical Physics* 129(2008).
185. Behr, J.-P. The Proton Sponge: a Trick to Enter Cells the Viruses Did Not Exploit. *Chimia* 51, 34-36 (1997).
186. Mu, Q., Broughton, D.L. & Yan, B. Endosomal leakage and nuclear translocation of multiwalled carbon nanotubes: developing a model for cell uptake. *Nano Lett* 9, 4370-4375 (2009).
187. Veiseh, O., *et al.* Cell transcytosing poly-arginine coated magnetic nanovector for safe and effective siRNA delivery. *Biomaterials* 32, 5717-5725 (2011).
188. Dominska, M. & Dykxhoorn, D.M. Breaking down the barriers: siRNA delivery and endosome escape. *J Cell Sci* 123, 1183-1189 (2010).
189. Varkouhi, A.K., Scholte, M., Storm, G. & Haisma, H.J. Endosomal escape pathways for delivery of biologicals. *J Control Release* 151, 220-228 (2011).
190. Bulte, J.W., *et al.* Neurotransplantation of magnetically labeled oligodendrocyte progenitors: magnetic resonance tracking of cell migration and myelination. *Proc Natl Acad Sci U S A* 96, 15256-15261 (1999).
191. Zhou, J. & Rossi, J.J. Aptamer-targeted cell-specific RNA interference. *Silence* 1, 4 (2010).

192. Wang, P., *et al.* Combined small interfering RNA therapy and in vivo magnetic resonance imaging in islet transplantation. *Diabetes* 60, 565-571 (2011).
193. Judge, A.D., *et al.* Confirming the RNAi-mediated mechanism of action of siRNA-based cancer therapeutics in mice. *J Clin Invest* 119, 661-673 (2009).
194. Bartlett, D.W. & Davis, M.E. Insights into the kinetics of siRNA-mediated gene silencing from live-cell and live-animal bioluminescent imaging. *Nucleic Acids Res* 34, 322-333 (2006).
195. Olive, K.P. & Tuveson, D.A. The use of targeted mouse models for preclinical testing of novel cancer therapeutics. *Clin Cancer Res* 12, 5277-5287 (2006).
196. Van Dyke, T. Finding the tumor copycat: approximating a human cancer. *Nat Med* 16, 976-977 (2010).
197. Guerra, C. & Barbacid, M. Genetically engineered mouse models of pancreatic adenocarcinoma. *Mol Oncol* 7, 232-247 (2013).
198. Fleet, M. The structure of magnetite: two annealed natural magnetites,  $\text{Fe}_{3.005}\text{O}_4$  and  $\text{Fe}_{2.96}\text{Mg}_{0.04}\text{O}_4$ . *Acta Crystallographica Section C: Crystal Structure Communications* 40, 1491-1493 (1984).

## 10. APPENDICES

## APPENDIX I

## Magnetite X-Ray diffraction data

**Structure:** 4, t-spinel inverse, f-oxospinelides, sf-spinel, s-magnetite

Cubic \* Fd3m Z = 8

**Reference structure:** ME Fleet (1984) Acta Cryst., C 40, 1491-1493 <sup>198</sup>

**Lattice parameters:**

a = 8.3969                      alpha = 90.0

a = 8.3969                      beta = 90.0

a = 8.3969                      gamma = 90.0

**Unit cell volume:** 592.07<sup>0</sup>A<sup>3</sup>

**Molar volume:** 44.58

**X-ray density:** 5.19g/cm<sup>3</sup>

**X-ray wavelength:** 1.78892<sup>0</sup>A

**JCPDS card for Magnetite:** 19-0629

**Table 14: JCPDS card for Magnetite**

N/N	H	K	L	d(hkl)	I/I <sub>0</sub> *100, %
1	1	1	3	2.53176	100
2	4	4	0	1.48438	43.5
3	2	2	0	2.96875	27
4	1	1	5	1.61598	20.5
5	4	0	0	2.09923	20
6	3	3	5	1.28052	10.5
7	2	2	4	1.71401	9.4
8	3	3	3	1.61598	8.2
9	2	2	2	2.42398	7.8
10	2	2	6	1.26588	4.4
11	1	1	1	4.84795	4.2
12	6	2	0	1.32767	3.9

**APPENDIX II****Stoichiometric calculation for siRNA/SPIONs**

Source of SPIONs: Fe<sub>3</sub>O<sub>4</sub> (Magnetite)

Crystal system: Isometric Hexaoctahedral

**Calculation for siRNA/SPIONs**

Unit cells volume of Magnetite: 592.07<sup>0</sup>A<sup>3</sup>

Unit cells volume of Magnetite: 0.59nm<sup>3</sup>

Average diameter of nanoparticles: 10nm

Average volume of nanoparticles: **392.50nm<sup>3</sup>**

Number of magnetite crystals per nanoparticle: **662.92**

Average Iron concentration: 0.02M

*(Calculated using Iron quantification assay)*

Average number of Iron atoms: 9.09 \* 10<sup>20</sup>/ml

*(Avagadro's calculation)*

Average number of Iron molecules in magnetite: **3.03 \* 10<sup>20</sup>/ml**

Number of units per Magnetite: 8

1 Crystal of Magnetite contains (8\*3): 24 iron atoms

24 molecules consist of 1 magnetite:

Thus, X molecules consists \_\_\_magnetite: 1.26\* 10<sup>19</sup>

Number of SPIONs per ml: 1.90\* 10<sup>16</sup>/ml

*(Calculated using Iron quantification assay)*

Average number of siRNA per ml: 9.06\* 10<sup>16</sup>/ml

*(Calculated using Ribogreen RNA quantification assay, followed by Avagadro's calculations)*

**Average number of siRNA/SPION: 4.75**

**APPENDIX III****Stoichiometric calculation for streptavidin binding sites**1. Theoretical calculations for streptavidin (StAv) binding

Molecular weight of StAv:	53000Da
Stock of StAv added to SPIONs:	2mg
Protein content in StAv:	0.84mg/mg
Actual StAv added to SPIONs:	1.68mg
Amount of protein detected/ml of SPIONs:	0.12mg/ml
Actual amount of StAv/ml of StAv/ml of SPIONs:	0.10mg/ml
<b>Average StAv concentration:</b>	<b><math>1.93 \times 10^{-6} \text{ M}</math></b>
Average number of StAv molecules:	$1.18 \times 10^{18}/\text{ml}$
<i>(Avagadro's calculation)</i>	
Number of SPIONs per ml:	$1.90 \times 10^{16}/\text{ml}$
<i>(Calculated using Iron quantification assay)</i>	
Number of StAv/SPIONs:	60
Number of Biotin binding site per subunits:	1
Number of Biotin binding sites per StAv tetramer:	4
<b>Theoretical average binding sites/SPIONs:</b>	<b>240</b>

2. Calculations for available Biotin binding sites/SPIONs

In order to elucidate actual biotin binding sites available for free Biotin streptavidin interaction, we developed the flourogenic assay using TRITC-Streptavidin and Biotin solution. We characterized the ratio for amount of TRITC-Streptavidin and Biotin needed using concentration titration. We used the standardized amount of TRITC-streptavidin and Biotin and measured the fluorescent intensity at (Ex: 557, Em: 590) 590nm (**E<sub>1</sub>**). Furthermore, we added known amount of StAv-SPIONs and we incubated it with known concentration of Biotin solution for 15 minutes at room temperature. We added then known concentration of TRITC-streptavidin and measured the fluorescent intensity at (Ex: 557, Em: 590) 590nm (**E<sub>2</sub>**). The difference between E<sub>1</sub> and E<sub>2</sub> (**E<sub>1</sub>- E<sub>2</sub>**) leads us to the actual amount of available biotin binding sites per SPIONs. (**Figure 55**)

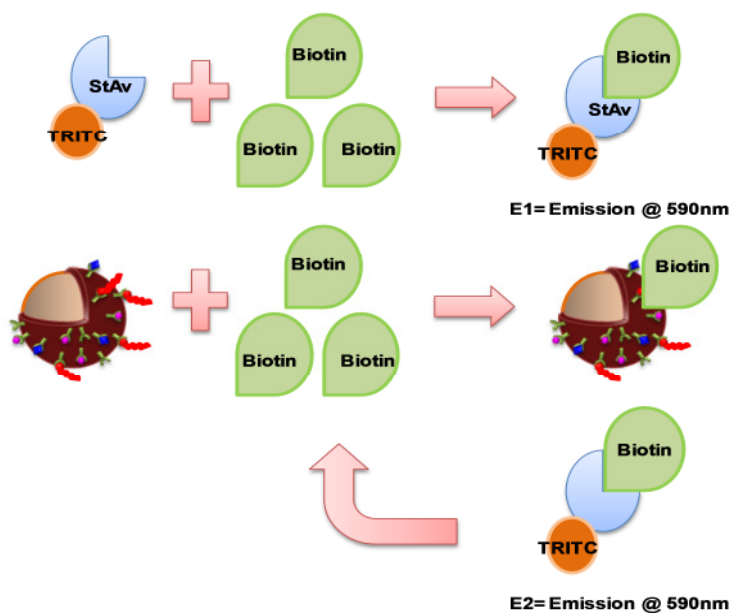


**Figure 55: Schematic diagram illustrating biotin binding sites evaluation using TRITC-Streptavidin substrate**

Average concentration of Biotin entrapped:  $1.46 \times 10^{-6} \text{M}$

Average number of biotin molecules/ml:  $1.10 \times 10^{+16}$

*(Avagadro's calculation)*

**Number of biotin binding sites available per SPIONs: 45**

## APPENDIX IV

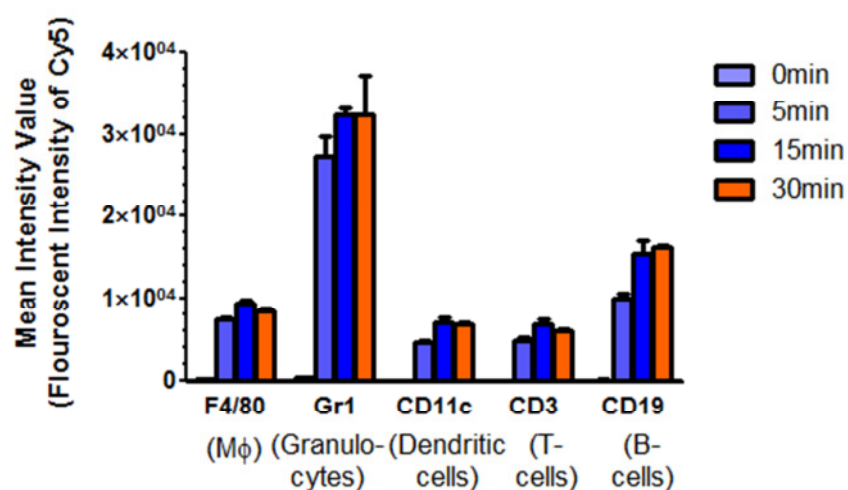


**Figure 56: siPLK1-StAv-SPIONs uptake by splenocytes 30 min after treatment.** FACS analysis of different subtypes of immune cells showed uptake of siPLK1-StAv-SPIONs quantified using fluorescent intensity of Cy5. Granulocytes showed maximum uptake of siPLK1-StAv-SPIONs as early as 5 min.

## 11. ACKNOWLEDGEMENT

There are many who have helped and inspired me during my doctoral study, I would like to convey my gratitude to all those people.

My deepest gratitude is to my mentors & guides; **Prof. Dr Julia Mayerle** and **Prof. Dr Markus M. Lerch** for providing me opportunity to do my PhD under his esteemed supervision at Universitätsmedizin Greifswald. They patiently provided the vision, encouragement and advice necessary for me to proceed through the doctoral program. Thanks a lot for giving me this opportunity to work here at KIM-A, Universitätsmedizin Greifswald; instilling the confidence in me and your help with the transition to a new professional perspective. I would also like to thank **Dr Frank-Ulrich Weiss** for his constant encouragement of my research work sharing their knowledge and co-operation to complete this thesis and constructive suggestions throughout my stay in Greifswald.

I would like to thank Prof. Kühn and Dr. Delcea for their kind help and support. I thank all my lab colleagues, Steffen, Matze, Theresa, Cindy, Sudu, Annette, Thomas, Sandrina, Georg, Enno, Patryk, Ali, Jonas, Armin, Raghav, Daniel, Julia A., Silvia, Stefan, Preshit and Myk for the wonderful time we had together for everything; be it lab or personal life. Your constant support and guidance helped me a lot and will always be remembered. Chain of gratitude would be incomplete if I forget to thank Kaddi, Diana, Doris, Susi and Norina for providing skillful technical assistance to carry out the research work successfully. I am also indebted to my other friends Pravin, Gaurav, Rashmita, Donna & others; thanks for your love & support. I would also like to thank Shrikant, Sachin, Rahul, Tushar, Yogesh and Kanchan for always being there with me. Thank you all for giving me the life long memories, engraved in my heart.

There are no words to express my feeling, love and affectionate gratitude to my family for their faith, love, inspiration, selfless sacrifices and constant encouragement throughout my life. I am grateful to everybody who has been part of my life and helped in some way or other, but if I failed to mention their names, thank you all.

It is my duty to express my tearful acknowledgement to the animals, which have been sacrificed for the betterment of human being.

## **SCHRIFTLICHE ERKLÄRUNG**

Hiermit erkläre ich, dass ich die vorliegende Dissertation selbständig verfasst und keine anderen als die angegebenen Hilfsmittel benutzt habe.

Die Dissertation ist bisher keiner anderen Fakultät, keiner anderen wissenschaftlichen Einrichtung vorgelegt worden.

Ich erkläre, dass ich bisher kein Promotionsverfahren erfolglos beendet habe und dass eine Aberkennung eines bereits erworbenen Doktorgrades nicht vorliegt.

Greifswald, 12/06/2016

(Ort, Datum)

(Ujwal Mukund Mahajan)